Master thesis

About the mechanical properties of bicycle tyres

by

Niels Baltus

in partial fulfillment of the requirements for the degree of

Master of Science
in Mechanical Engineering

at the Delft University of Technology.

Supervisor: Dr. ir. Arend L. Schwab

Abstract

A lot of research has been done on the behaviour of pneumatic tyres and this has led to various tyre models and a lot of measurement data. However, in the specific field of bicycle tyres, not so much measurement data is available. However, in 2013 Andrew Dressel received the Degree of Doctor of Philosophy in Engineering at the University of Wisconsin-Milwaukee by presenting his research: Measuring and modeling the mechanical properties of bicycle tires. In this research he did a lot of measurements with multiple bicycle tyre brands and models under different conditions. The results from these measurements are interesting to use for modelling purposes.

The goal of this research is to find out if it is possible to estimate the bicycle tyre behaviour in terms of vertical stiffness, cornering stiffness and camber stiffness based on known parameters like the inflation pressure, tyre width, rim width, vertical load and the rubber compound using a tyre model.

An important part of this thesis are tyre models. The measurement data will be analysed using various tyre models. The first used tyre model is the brush model. This model uses a single material parameter and it turns out that this is too less to be able to extract clear relations between the tyre behaviour and the known parameters like inflation pressure, tyre width and rim width.

The second tyre model that is used is the enhanced string model. This model is an extension of the brush model. This model has three material parameters for the vertical direction and also three material parameters for the lateral direction. Investigating this model shows that there is reasonable suspicion to assume that one of the model parameters represents the inflation pressure. In order to find the material parameters for every tyre, inflation pressure and normal load combination a parameter optimisation is required. The results from this parameter optimisation show that the suspected model parameter is actually not related to the inflation pressure. When the obtained model parameters from the optimisation are put back into the tyre model interesting results are acquired, because the model output agrees fairly well with the measurement data. This is unexpected because the model parameters were differing a lot depending on how they were obtained, e.g. obtaining the parameters from cornering stiffness or from camber stiffness.

The answer to the research question is no. In order to extract relations between the model parameters and the tyres behaviour depending on their measurable properties, a lot more complete measurements are needed. The whole idea was to be able to estimate tyre behaviour without the need of extensive testing. This still might be possible, but in order to to that a lot more measurements are needed first. These measurements should create a baseline of model parameters which can be used to estimate the model parameters of unmeasured tyres.

Contents

1

Introduction

A tyre transfers the vehicle's load from the axle through the wheel to the surface over which it travels and provides traction. Most tyres, such as car, aircraft and bicycle tyres are pneumatically inflated rubber structures. It is this composition that makes tyres do what they are meant to do; provide traction in longitudinal and lateral direction and absorb shocks in vertical direction. However, it is also this composition that makes the behaviour of tyres highly non-linear. This non-linear behaviour makes it hard to model a tyre. A lot of research has been done on the behaviour of pneumatic tyres and this has led to various tyre models. These tyre models can be divided into two groups: phenomenological models and physical models [1]. The phenomenological models are based on experimental data and the physical models are theory based. Naturally, combinations of both models also exist.

Nowadays, the phenomenological model developed by Prof. Dr. Ir. Pacejka, the Magic Formula, for forces generated in tyre contact patches is widely used, since this model can approximate the tyre forces quite accurately. The disadvantage is that they are not based on physical properties of the tyre and a lot of measurements are needed to find the values of the large amount of parameters that describe the tyre behaviour.

A physical model, FTire [2], is a finite element method computer simulation. This model also approximates the tyre forces accurately. Here the disadvantage is that it cannot run accurate simulations in real-time. A lot of processing power is needed to calculate the tyre forces.

1.1. Motivation for this research

1.1.1. Behavioural expectancy of a bicycle tyre

Bicycle tyres are expected to behave more simply than car or truck tyres. Car and truck tyres have steel belts and a thick carcass, which causes more non-linear effects in their behaviour and makes the modelling more complex. A bicycle tyre is slender when the contact patch width is compared to the wheel radius and the contact patch length. A bicycle tyre is also circular in cross section, which suggests a simpler geometry [3]. Most bicycle tyres for urban purposes also have a thin casing with almost no bending stiffness (non-inflated). This behavioural expectancy suggests easier tyre modelling, where less model parameters are needed to describe the tyre behaviour.

1.1.2. Bicycle tyre measurements

In 2013 Andrew Dressel received the Degree of Doctor of Philosophy in Engineering at the University of Wisconsin-Milwaukee by presenting his research: Measuring and modeling the mechanical properties of bicycle tires [4]. In this research he did a lot of measurements with multiple bicycle tyre brands and models. The results from these measurements are interesting to use for modelling purposes. In addition to this research a group of bachelor students examined the vertical stiffness under different conditions [5] of the same bicycle tyres as used by Dressel. This increases the usefulness for modelling purposes, because a more complete data set is available.

1.2. Research objectives and contributions

The combination of the many bicycle tyre measurements done by Dressel and the plausible expectation that bicycle tyres behave more simply than car or truck tyres, brings us to the objectives of this research.

1.2.1. Research question

Is it possible to estimate bicycle tyre behaviour in terms of vertical stiffness, cornering stiffness and camber stiffness based on known parameters like the inflation pressure, tyre width, rim width, vertical load and the rubber compound using a tyre model?

In short: *Is it possible to estimate bicycle tyre behaviour based on known parameters using a tyre model?*

In order to answer this question the following three main things are needed:

- The relation between the known parameter and the behavioural property.
- A tyre model.
- The values of the tyre model parameters as a function of the known tyre parameters.

The first thing has already been found by Dressel and the group of bachelor students. The second component is being decided on in this research. As has been slightly discussed before, there are several tyre models which differ in approach and complexity. In this research the focus lies on physical tyre models with a low amount of parameters describing the tyre behaviour. Various physical tyre models will be elaborated and a choice will be made. The next step is to find the model parameters as a function of the known tyre parameters. After this is done, the results will be analysed and the research question will be answered.

1.3. Structure

Several tyre models will be discussed in Chapter 2. In the end of Chapter 2 a choice is made to be able to find the tyre model parameters as a function of the known tyre parameters. Chapter 3 is dedicated to investigating the enhanced string model, which is done for better understanding of that model and to have a feeling for interpreting the results. In Chapter 4 the methods are explained: How to come from the derived model equations and measurement data to the results. The results are shown in Chapter 5. In Chapter 6 the results will be discussed and finally in Chapter 7 conclusions are drawn and recommendations for future work will be given.

2

Tyre Models

2.1. Tyre brush model

In this section the theory of the tyre brush model will be explained. This theory is described in chapter 3 of Tire and Vehicle Dynamics by Pacejka [1]. It is an extension to the original 'brush' model of Fromm and Julien from 1952.

Theory of the tyre brush model

The tyre brush model is a relatively simple theoretical tyre model. In the brush model the tyre is represented by a row of elastic bristles that touches the road plane. The bristles can be seen as the tread elements and are able to deflect in a direction parallel to the road surface. The flexibility of the bristles represents the elasticity of the combination of carcass, belt and actual tread elements of the real tyre. The first element of a rolling tyre that enters the contact zone is assumed to stand perpendicular to the road surface. For a freely rolling tyre in upright position (no camber angle), so no turning (no side-slip angle), accelerating or braking (no tyre slip), all elements are perpendicular to the road surface and in this case they are not generating a force. Rolling resistance will be ignored for the sake of simplicity. In the case that the wheel velocity vector V has an angle with respect to the wheel plane, side-slip occurs. Fore-and-aft slip occurs when the rotational wheel velocity multiplied with the effective rolling radius is not equal to the forward component of the wheel velocity. The combined slip situation is shown in Figure 2.1. The deflection of the elements induce forces and depending on the position of the resultant force, a moment occurs as well. In Figure 2.2 pure side-slip situations are shown. As can be seen there is a maximum amount of possible deflection depending on the position in the contact region of the element. This is determined by the vertical force distribution. The maximum force that can be generated by the tyre depends on three parameters: the friction coefficient μ, the vertical force distribution q_z and the stiffness of the element c_{py}. The vertical force distribution is assumed to be parabola shaped. With this the maximum deflection is also parabola shaped. As shown in Figure 2.2 there are two possible states for the contact region: adhesion and sliding. The point where the straight line intersects the parabola is the point from where the sliding starts. By increasing the slip angle, the generated side force increases. The position from the resultant force behind the contact centre is called the pneumatic trail t. The aligning torque is generated by the non-symmetric shape of the deflection distribution and can be calculated by multiplying the lateral force with the pneumatic trail. The characteristics of the lateral force and aligning torque at increasing side-slip angle are shown on the right side of Figure 2.2.

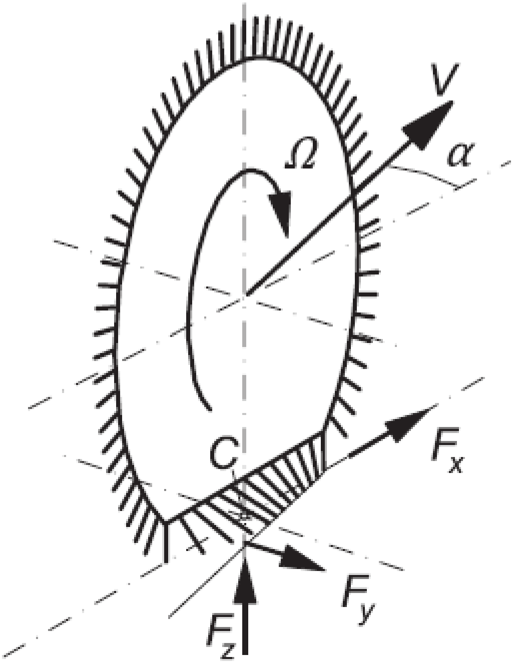

Figure 2.1: A visual representation of both slip situations in the brush tyre model [1].

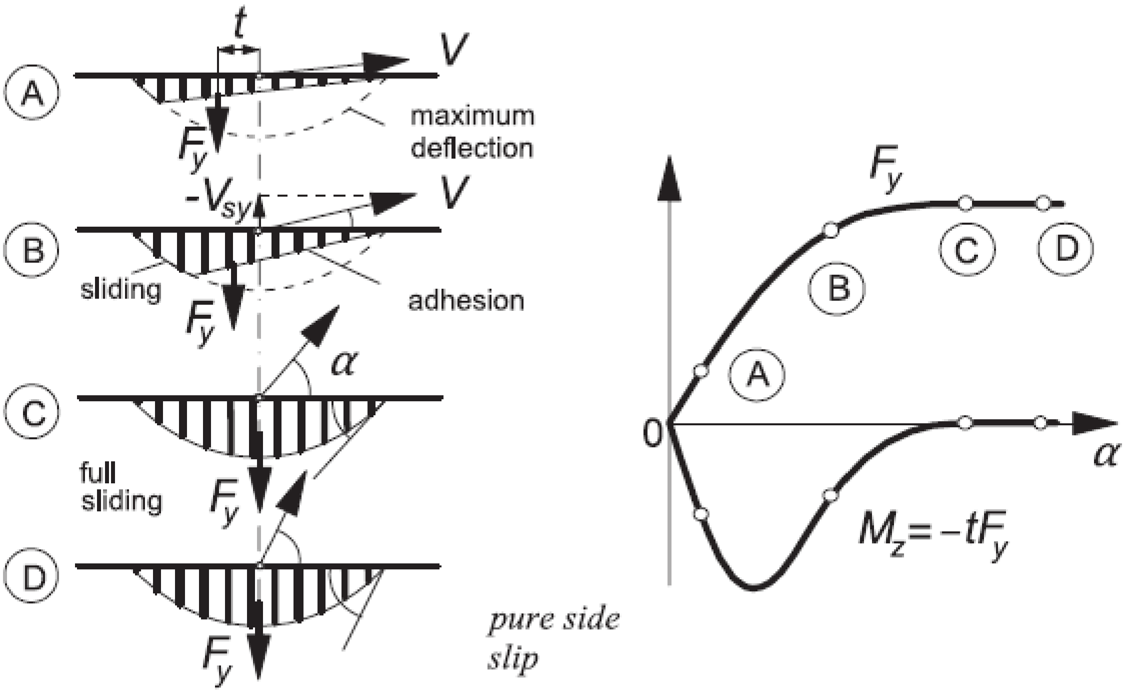

Figure 2.2: Left: Pure side-slip, from small to large slip angle. Right: Resulting side force and aligning torque characteristics [2].

Since Dressel did measurements for pure side-slip and camber, only the lateral part of the tyre brush model will be further elaborated. First the pure side-slip will be discussed and secondly the camber.

---

[1] Image is taken from [1].

[2] Image is taken from [1].

2.1.1. Pure side slip

A more detailed visualisation of the tyre brush model moving at a constant slip angle is depicted in Figure 2.3. The contact line in the adhesion range is straight and parallel to the velocity vector V and in the sliding range it is curved, since the available frictional force becomes lower than the force which would be required for the tips of the tread elements to follow the straight line further. The lateral deformation in the adhesion range equals

$$v = (a - x)\tan\alpha \tag{2.1}$$

where a is half the contact length. For $\alpha \to 0$ or $\mu \to \infty$, the sliding region vanishes and Equation 2.1 is valid for the entire contact region. The following integrals and expressions for the cornering force F_y and the self-aligning torque M_z hold:

$$F_y = c_{py}\int_{-a}^{a} v dx = 2c_{py}a^2\alpha \tag{2.2}$$

$$M_z = c_{py}\int_{-a}^{a} v x dx = -\frac{2}{3}c_{py}a^3\alpha \tag{2.3}$$

where c_{py} is the stiffness of the tread elements per unit length of the assumedly rectangular contact area.

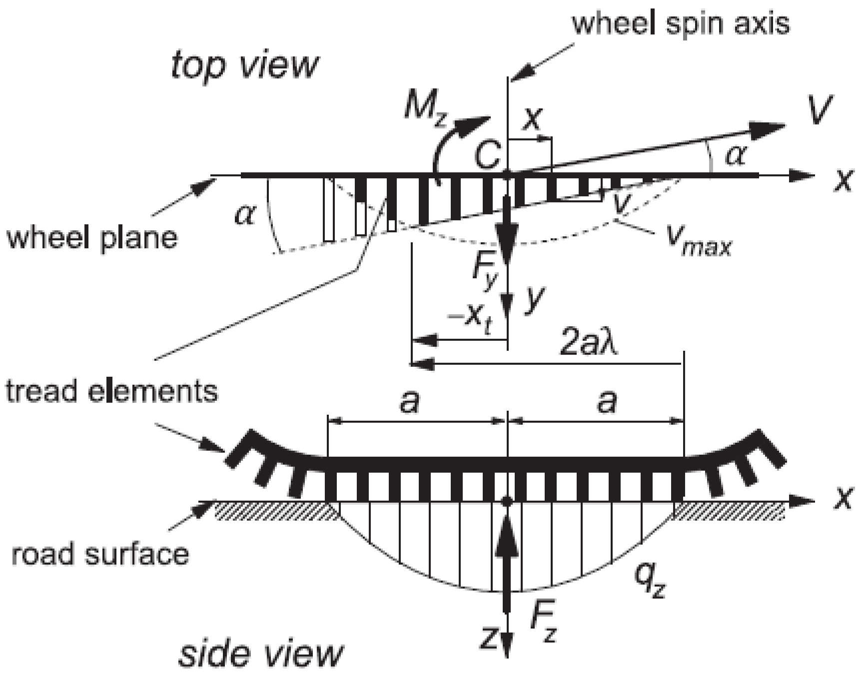

Figure 2.3: Top and side view of the tyre brush model moving at pure slip angle [3].

From equations 2.2 and 2.3 the cornering stiffness and self-aligning torque stiffness can be deduced respectively.

$$C_{F_\alpha} = \left(\frac{\partial F_y}{\partial \alpha}\right)_{\alpha=0} = 2c_{py}a^2 \tag{2.4}$$

$$C_{M_\alpha} = -\left(\frac{\partial M_z}{\partial \alpha}\right)_{\alpha=0} = \frac{2}{3}c_{py}a^3 \tag{2.5}$$

---

[3] Image is taken from [1].

The cornering stiffness C_{F_α}, self-aligning torque stiffness C_{M_α}, and contact patch length $2a$ are all measured by Dressel. With these measured parameters, material parameter c_{py} can be calculated with equations 2.4 and 2.5 rewritten as:

$$c_{py} = \frac{C_{F_\alpha}}{2a^2} \tag{2.6}$$

and

$$c_{py} = \frac{3C_{M_\alpha}}{2a^3} \tag{2.7}$$

2.1.2. Camber and turning

Along with longitudinal slip (slip ratio) and lateral slip (slip angle) there is a third slip quantity which is called spin. The total spin consists of two components: camber and turn slip. This third slip quantity is described by Pacejka in [6]. In Figure 2.4 a visualisation of spin is depicted, with γ indicating the camber angle, the yaw angle ψ, path radius R and the wheel rotational velocity Ω.

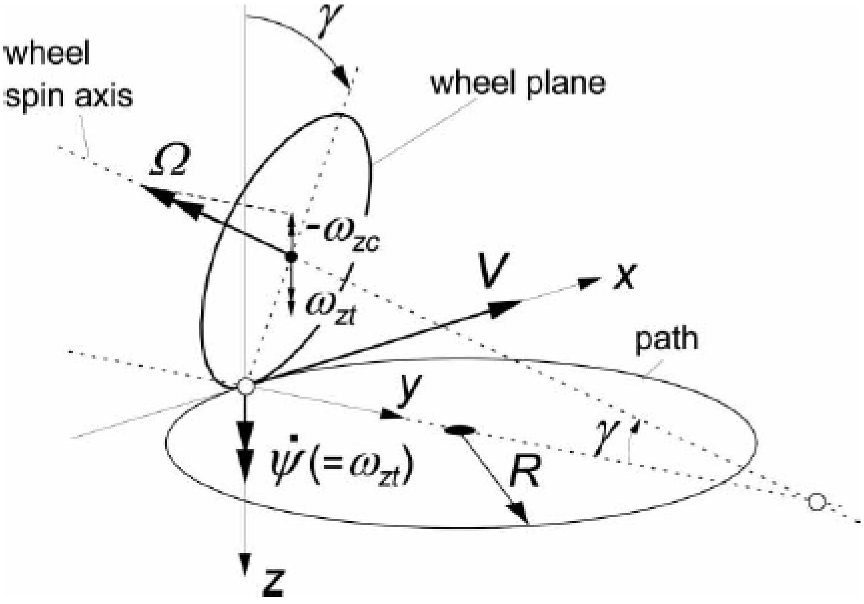

Figure 2.4: Pure turn slip and camber [4].

The normal component of the rotational velocity ω_z over the forward velocity V is called the spin slip φ. For a freely rolling wheel (no braking, driving or side slip), the following equation is valid:

$$\varphi = -\frac{1}{V}\omega_z = -\frac{1}{V}(\dot{\psi} - \Omega\sin\gamma) = -\frac{1}{R} + \frac{1}{r_e}\sin\gamma \tag{2.8}$$

The total spin in fact is just the difference of two curvatures: one of the path of the contact centre and the other of the vertical projection of the peripheral line of the undeformed tilted tyre. In the article by Pacejka [6] a camber reduction factor ϵ_y has been introduced, because of the relatively small camber stiffness of car and truck tyres compared to motorcycle tyres. For this research the camber reduction factor will be neglected. In the measurements done by Dressel, the wheel is travelling in a straight line with a forced camber angle. This means that the wheel is not rotating around its z-axis, such that $\dot{\psi}$ is equal to zero. The spin slip becomes:

$$\varphi = \frac{1}{V}\Omega\sin\gamma = \frac{1}{r_e}\sin\gamma \tag{2.9}$$

---

[4] Image is taken from [6].

The lateral force and the self-aligning torque respectively are:

$$F_y = C_{F_\alpha}\alpha + C_{F_\varphi}\varphi \tag{2.10}$$

$$M_z = -C_{M_\alpha}\alpha + C_{M_\varphi}\varphi \tag{2.11}$$

For the measurement of camber stiffness, Dressel kept the slip angle at zero. Such that Equation 2.10 can be reduced to:

$$F_y = C_{F_\varphi}\varphi \tag{2.12}$$

Since Dressel did the measurements by altering the camber angle (for small camber angles), this equation should be written as:

$$F_y = C_{F_\varphi}\frac{1}{r_e}\sin\gamma = C_{F_\varphi}\frac{1}{r_e}\gamma \tag{2.13}$$

In the article by Pacejka [6] reciprocity is observed in the moment response to side-slip and the force response to turn slip. For the tyre brush model it turns out that

$$C_{F_\varphi} = C_{M_\alpha} \tag{2.14}$$

With this information the material stiffness c_{py} can be obtained from the turn slip stiffness. Combining equations 2.5 and 2.12, the following relation for the spin stiffness and material parameter c_{py} is found:

$$C_{F_\varphi} = \left(\frac{\partial F_y}{\partial \varphi}\right)_{\varphi=0} = \left(\frac{\partial F_y}{\partial \gamma}\right)_{\gamma=0} r_e = \frac{2}{3}\frac{1}{r_e}c_{py}a^3 \tag{2.15}$$

The value measured by Dressel is the spin stiffness (for pure camber) and the material parameter c_{py} can be obtained in the following way:

$$c_{py} = \frac{3C_{F_\varphi}r_e}{2a^3} \tag{2.16}$$

2.1.3. Pneumatic trail

As mentioned before, the position from the resultant force behind the contact centre is called the pneumatic trail t. The resultant lateral force times the pneumatic trail is the self aligning torque. Since Dressel measured both the lateral force and the self-aligning torque and calculated the stiffnesses from both, the pneumatic trail can be calculated by:

$$t = -\frac{C_{M_\alpha}}{C_{F_\alpha}} \tag{2.17}$$

In Tire and Vehicle Dynamics [1] Pacejka shows that at vanishing slip angle, the expression for pneumatic trail reduces to:

$$t = t_0 = -\left(\frac{M_z}{F_y}\right)_{\alpha\to 0} = \frac{1}{3}a \tag{2.18}$$

This is one-sixth of the contact patch length.

2.2. Rotta model

This section will elaborate on the Rotta model. The Rotta model is based on assumptions that work really well with bicycle tyres. The main assumption that is made in the Rotta model is the shape of the tyre, which is a circle when there is no vertical force applied to the wheel. This is a simpler geometry for which it is easier come up with equations that use this geometry for tyre force calculations.

Theory of the Rotta model

Rotta's model dates from 1949 [7] and is written in German. A translation from the Cornell Aeronautical Laboratory is available [8]. Rotta developed a tyre element model, which is an infinitesimal slice of the tyre and rim. Papadopoulos and Dressel extended the model for a whole tyre instead of just a single section. For a narrow tyre and long contact patch, it is assumed that the slowly varying deformation can be analysed as a series of non-coupled 2D elements [3]. This will be discussed later on, first the basics of the Rotta model will be explained.

Cross-section geometry

In the Rotta model, the rim is expressed as a rigid line segment and the tyre as an inextensible string joining the rim edges. The inside contains air pressure p_0 relative to the external atmosphere. In Figure 2.5 a cross-section as defined by Rotta is shown. B is the tyre width, B_s is the rim width and H is the uncompressed tyre height. The initial angle γ_0 relative to the horizontal of the rim can be found from $\sin(\gamma_0) = B_s/B$.

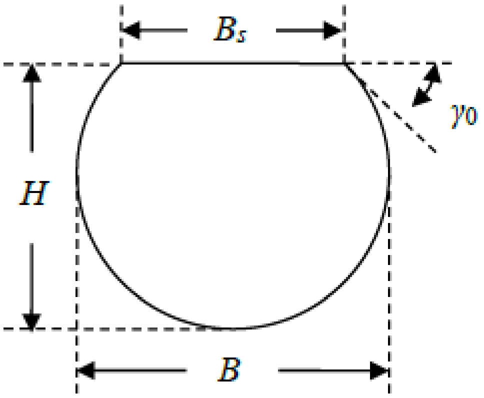

Figure 2.5: Unloaded tyre cross-section as defined by Rotta [5].

Papadopoulos chooses to use the parameters as shown in Figure 2.6. w_0 is half the rim width, L is the casing half length and ϕ_0 represents the initial angle substended by half the tyre ($\phi_0 = \pi - \gamma_0$).

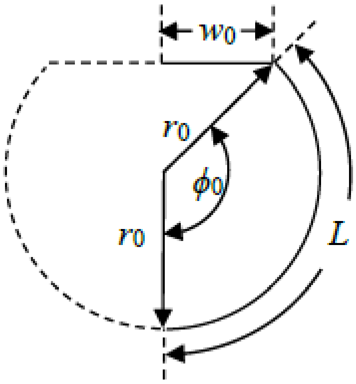

Figure 2.6: Unloaded tyre cross-section as defined by Papadopoulos [6].

---

[5] Image is taken from [3].

Combining $L = r_0\phi_0$ and $w_0 = r_0 \sin\phi_0$ eliminates the initial radius r_0 and gives an implicit equation for ϕ_0 (has to be solved numerically):

$$\frac{\sin\phi_0}{\phi_0} = \frac{w_0}{L} \tag{2.19}$$

By applying a vertical force on the rim without any tyre slip, the casing will be pressed flat to the ground over a contact width $2d$, see Figure 2.7. It departs the ground while being tangent to the ground at the edge of both sides of the contact patch and then follows a circular arc up to the edge of the rim. It is assumed that the length of the casing does not change, such that the sum of the circular sidewall arcs and the part flat on the ground is a fixed number ($2L$).

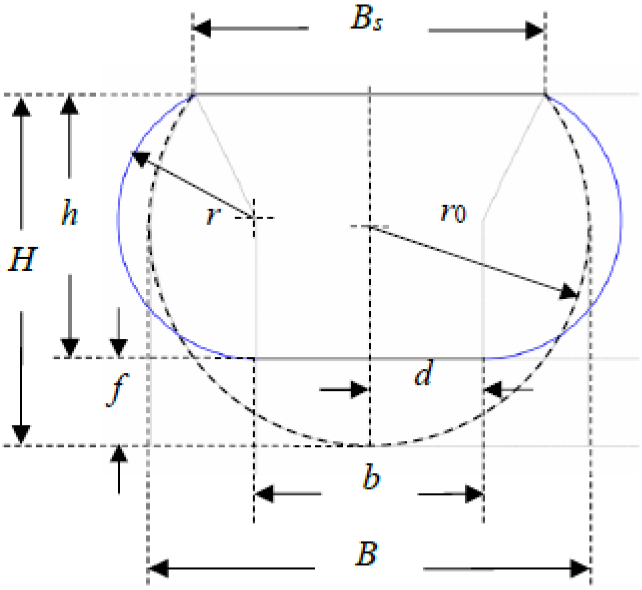

Figure 2.7: Tyre cross-section of a vertical loaded rim as defined by Papadopoulos [7].

Consider the midpoint of the tyre casing to touch the ground at a coordinate system origin. Then for any position of the rim, there is a simple geometry problem to be solved for each sidewall: Determine the distance d from the origin to the edge of the contact region, and arc parameters radius r and subtended angle ϕ, such that: The contacting length d plus the arc length $r\phi$ is equal to the fixed casing half-length L:

$$d + r\phi = L \tag{2.20}$$

The y-coordinate of the final casing point $d + r\sin\phi$ matches the y-coordinate of the rim edge:

$$d + r\sin\phi = Y_{rim} \tag{2.21}$$

The z-coordinate of the final casing point $r(1-\cos\phi)$ matches the z-coordinate of the rim edge:

$$r(1-\cos\phi) = Z_{rim} \tag{2.22}$$

These three requirements suffice to determine d, r, ϕ uniquely from L, Y_{rim}, Z_{rim}. Although a closed form solution has not been found, the following reduction is useful: Eliminate r from Equation 2.19 and 2.20, then solve for d:

$$d = \frac{Y_{rim}\phi - L\sin\phi}{\phi - \sin\phi} \tag{2.23}$$

With this value of d, Equation 2.19 can be used to write

$$r = \frac{L - Y_{rim}}{\phi - \sin\phi} \tag{2.24}$$

---

[6] Image is taken from [3].

[7] Image is taken from [3].

This can be substituted in Equation 2.21 and gives an implicit equation for ϕ:

$$\frac{L - Y_{rim}}{Z_{rim}} = \frac{\phi - \sin\phi}{1 - \cos\phi} \tag{2.25}$$

This is for any rim edge coordinates relative to the ground point corresponding to the casing midpoint. It should be possible to determine ϕ and subsequently compute the other geometric quantities.

When the rim is moved towards the ground the deformation is symmetric. Both sidewalls will have the same length, such that they have identical values of d, r, and ϕ. When the compressed rim is rotated or laterally translated, the right and left solutions are different. From this difference the ground reaction forces on the rim can be determined.

2.2.1. Tyre forces

For an element of the tyre the forces and moments (per unit length) applied to the displaced and rotated rim segment need to be found. This is most easily done by determining the forces of the tyre on the ground, then the reverse of these are the ground reactions acting on the wheel.

The vertical force (per unit circumferential distance) on the tyre is equal to the tyre pressure times the total width of contact: $F_z = p_0(d_L + d_R)$. The line of action is at the centre of the contact region, with x-coordinate $(d_R - d_L)/2$.

The horizontal force (per unit circumferential distance) on the tyre can be derived from the difference in sidewall tension. The sidewall tension is calculated as $T = p_0 r$. So the lateral force on the tyre is $p_0(r_L - r_R)$.

2.3. Enhanced string model

The theory of the enhanced string model will be discussed in this section.

Theory of the enhanced string model

The enhanced string model is an extension of the brush model. As with the brush model, the contact patch is assumed to be narrow, such that the contact patch can be represented by a line. This assumption turns the two-dimensional problem into a one-dimensional problem. The bristles of the brush remain and a two-parameter Pasternak foundation is added. The bristles represent the stiffness of the tread, whereas the restoring force of the foundation represents the stiffness generated by the inflation pressure, the sidewalls and the pre-stress of the tyre belt. In the paper by Meijaard [9] it is described that the restoring force is given by a combination of a part that is proportional to the deflection, as in Winkler elastic foundation, and a part that is proportional to the second derivative, the change in curvature, which is caused by the shearing of the foundation. This model is used in the vertical and the lateral direction. For the longitudinal direction, the model is simplified, but that does not matter for this research, since the available measurements are only done for the vertical and lateral directions. First the normal force distribution will be elaborated and then the lateral force distribution.

2.3.1. Normal force distribution

The equations for the normal force distribution are elaborated in this section. An undeformed belt radius R_b of the tyre is assumed. If the camber angle is zero, this is just the outer radius in the plane of symmetry minus the tread thickness, which is equal to the length l_t of the bristles. However, if there is a camber angle, the centre of curvature is on the axis of the wheel. The stiffness generated by the inflation pressure, the sidewalls and the pre-stress of the tyre belt and the stiffness of the tread elements are directional. Therefor a local right-handed orthonormal coordinate system $oxyz$ is introduced in the contact patch. The origin is in the centre of the contact patch, the z-axis is pointing in the downward direction, the x-axis is pointing in the forward direction, parallel to the wheel plane, and the y-axis is pointing to the right. The normal stiffness of the bristles is k_{tz} (N m^{-2}) per unit of length, the normal stiffness of the foundation is k_{Wz} (N m^{-2}) per unit of length and the shear stiffness of the foundation is k_{Pz} (N). The subscript z denotes the vertical direction, t is the subscript for the tread, W stands for the Winkler part of the foundation and P for the Pasternak part. Furthermore, there is ϵ_n, which is the deflection of the tyre. This is defined as the sinking of the wheel centre in comparison with the position that the tread just touches the road. The half of the contact length is denoted by a. It is assumed that the normal force distribution is symmetric. The displacements w_t of the tread elements can be approximated by a parabolic distribution, since the stiffness is considered constant and the displacements small. Positive in upward direction, the displacement is

$$\begin{aligned} w_t &= \epsilon_n - \frac{x^2}{2R_b} && (-a < x < a) \\ w_t &> \epsilon_n - \frac{x^2}{2R_b} && (x < -a \text{ or } x > a), \end{aligned} \tag{2.26}$$

where x is the distance along the contact line, which is zero in the centre and positive in the forward direction. The force on the tread elements outside of the contact patch is zero. The part of the potential energy per unit of length resulting from normal displacements is given by

$$U_z = \frac{1}{2}k_{Pz}(w_b')^2 + \frac{1}{2}k_{Wz}w_b^2 + \frac{1}{2}k_{tz}(w_b - w_t)^2, \tag{2.27}$$

where w_b is the normal deflection of the tyre belt, which is positive in the upward direction, and the prime denotes a derivative with respect to x. Meijaard [9] takes variations in the potential energy with respect to the belt displacement and obtains the following differential equation

$$\begin{aligned} -k_{Pz}w_b'' + (k_{Wz} + k_{tz})w_b = k_{tz}w_t \qquad & (-a < x < a), \\ -k_{Pz}w_b'' + k_{Wz}w_b = 0 \qquad & (x < -a \text{ or } x > a). \end{aligned} \tag{2.28}$$

The bounded solutions outside the contact region are given by

$$\begin{aligned} w_b(x) = w_b(a)e^{-\kappa_{zo}(x-a)}, \quad & w_b'(x) = -\kappa_{zo}w_b(a)e^{-\kappa_{zo}(x-a)} \qquad (x > a), \\ w_b(x) = w_b(-a)e^{-\kappa_{zo}(x+a)}, \quad & w_b'(x) = -\kappa_{zo}w_b(-a)e^{-\kappa_{zo}(x+a)} \quad (x < -a). \end{aligned} \tag{2.29}$$

In this equation $\kappa_{zo} = (k_{Wz}/k_{Pz})^{1/2}$. The solutions in Equation 2.29 give the following boundary conditions

$$\kappa_{zo} w_b(a) + w_b'(a) = 0, \quad \kappa_{zo} w_b(-a) - w_b'(-a) = 0. \tag{2.30}$$

The symmetric solution within the contact region can be written as

$$w_b(x) = C_z \cosh(\kappa_{zi} x) + \left(1 - \frac{\kappa_{zo}^2}{\kappa_{zi}^2}\right)\left(\epsilon_n - \frac{x^2}{2R_b} - \frac{1}{\kappa_{zi}^2 R_b}\right), \tag{2.31}$$

where $\kappa_{zi} = [(k_{Wz} + k_{tz})/k_{Pz}]^{1/2}$ and the constant C_z follows from the boundary condition at $x = a$ in Equation 2.30. The value of a can be found as the positive solution to the equation

$$\begin{gathered} w_b(a) = w_t(a) = \epsilon_n - \frac{a^2}{2R_b}, \text{ or} \\ C_z \cosh(\kappa_{zi} a) - \frac{\kappa_{zo}^2}{\kappa_{zi}^2}\left(\epsilon_n - \frac{a^2}{2R_b}\right) - \left(1 - \frac{\kappa_{zo}^2}{\kappa_{zi}^2}\right)\frac{1}{\kappa_{zi}^2 R_b} = 0 \end{gathered} \tag{2.32}$$

This equation can be solved by an iterative procedure. A good starting value for half the contact length appears to be

$$a = (2R_b \epsilon_n)^{1/2} \tag{2.33}$$

The available measurements from Dressel [4] already contain the contact length data. This is a good way to check if the approximation from Meijaard is in agreement with the measurement data. The pressure distribution per unit length is given by $p_z = k_{tz}(w_t - w_b)$, where a compressive pressure is positive:

$$p_z = k_{tz}\left[- C_z \cosh(\kappa_{zi} x) + \left(1 - \frac{\kappa_{zo}^2}{\kappa_{zi}^2}\right)\frac{1}{\kappa_{zi}^2 R_b} + \frac{\kappa_{zo}^2}{\kappa_{zi}^2}\left(\epsilon_n - \frac{x^2}{2R_b}\right)\right] \qquad (-a < x < a). \tag{2.34}$$

The normal compressive force can be found by integrating the normal pressure over the contact line:

$$F_z = \int_{-a}^{a} p_z dx = 2k_{tz} a\left[- C_z \frac{\sinh(\kappa_{zi} a)}{\kappa_{zi} a} + \left(1 - \frac{\kappa_{zo}^2}{\kappa_{zi}^2}\right)\frac{1}{\kappa_{zi}^2 R_b} + \frac{\kappa_{zo}^2}{\kappa_{zi}^2}\left(\epsilon_n - \frac{a^2}{6R_b}\right)\right]. \tag{2.35}$$

In order to find the values of the parameters of this model for the tested tyres by Dressel and the guys from the Bachelor Thesis, Equation 2.35 has to be rewritten. In this case the measurement data is the vertical stiffness, which is defined as:

$$C_{F_z} = \left(\frac{\partial F_z}{\partial \epsilon_n}\right)_{\epsilon_n = 0}. \tag{2.36}$$

Taking the partial derivative of Equation 2.35 to the vertical deflection gives the following equation:

$$\left(\frac{\partial F_z}{\partial \epsilon_n}\right)_{\epsilon_n = 0} = 2k_{tz} a\left(- \frac{\partial C_z}{\partial \epsilon_n}\frac{\sinh(\kappa_{zi} a)}{\kappa_{zi} a} + \frac{\kappa_{zo}^2}{\kappa_{zi}^2}\right). \tag{2.37}$$

In this equation the derivative of C_z with respect to ϵ_n is equal to:

$$\frac{\partial C_z}{\partial \epsilon_n} = \frac{\kappa_{zo}\left(\frac{\kappa_{zo}^2}{\kappa_{zi}^2} - 1\right)}{\kappa_{zo} \cosh(\kappa_{zi} a) + \kappa_{zi} sinh(\kappa_{zi} a)}. \tag{2.38}$$

Combining this with Equation 2.37 gives us the following equation:

$$\left(\frac{\partial F_z}{\partial \epsilon_n}\right)_{\epsilon_n = 0} = 2k_{tz}\left(- \frac{\sinh(\kappa_{zi} a)}{\kappa_{zo} \cosh(\kappa_{zi} a) + \kappa_{zi} \sinh(\kappa_{zi} a)} \frac{\kappa_{zo}}{\kappa_{zi}}\left(\frac{\kappa_{zo}^2}{\kappa_{zi}^2} - 1\right) + a\frac{\kappa_{zo}^2}{\kappa_{zi}^2}\right). \tag{2.39}$$

This can be reduced to:

$$\left(\frac{\partial F_z}{\partial \epsilon_n}\right)_{\epsilon_n = 0} = 2k_{tz}\left(- \frac{1}{\frac{\kappa_{zo}}{\tanh(\kappa_{zi} a)} + \kappa_{zi}} \frac{\kappa_{zo}}{\kappa_{zi}}\left(\frac{\kappa_{zo}^2}{\kappa_{zi}^2} - 1\right) + a\frac{\kappa_{zo}^2}{\kappa_{zi}^2}\right). \tag{2.40}$$

As mentioned before, $\kappa_{zo} = (k_{Wz}/k_{Pz})^{1/2}$ and $\kappa_{zi} = [(k_{Wz} + k_{tz})/k_{Pz}]^{1/2}$. Filling these into Equation 2.40 gives a really messy equation so that won't be done.

2.3.2. Stationary lateral force distribution

Now an equation is available for finding the vertical stiffness of the tread and the foundation, the same will be done for the lateral stiffness. The velocity distribution along the contact line is given by

$$V_{by}(x) = V_y + \Omega_z x - \Omega_x R_b. \tag{2.41}$$

Since it is a stationary motion, $\Omega_x = 0$. The lateral slip velocity is defined as the lateral velocity of the centre of the contact line:

$$\dot{\epsilon}_y \equiv V_{by}(0) = V_y - \Omega_x R_b \tag{2.42}$$

The dimensionless lateral slip is defined in the following way:

$$s_y = \frac{\dot{\epsilon}_y}{V_x} = \frac{V_y}{V_x} - \frac{\Omega_x R_b}{V_x} \tag{2.43}$$

In the brush model from previous chapter the lateral slip was denoted by α, but for this model s_y is used. As explained in the previous chapter the third slip quantity, along with the longitudinal slip and the lateral slip, is the spin. The normal spin is defined as:

$$s_n = \frac{-\Omega_z R_b}{V_x} \tag{2.44}$$

Again, another notation for the spin slip is used compared to previous chapter (s_n instead of φ).

The lateral displacement of the belt and bristles are v_b and v_t respectively. In the stationary case, an extra script s will be added. The contact region is divided into two parts, just as with the brush model from previous chapter. These are the adhesion region and the sliding region. The point where adhesion region transitions into the sliding region is denoted by $\bar{x}$. This is only valid when the normal spin is small or if the normal spin and the lateral slip have opposite signs, as is the case for motorcycles and bicycles in stationary cornering. The lateral displacement of the bristles in the adhesion region, for the stationary case, is given by

$$v_t(x) = v_{t,s}(x) = v'_{b,s}(a) - (a-x)s_y + (a^2 - x^2)\frac{s_n}{2R_b} \tag{2.45}$$

Similar to the equations for vertical displacement, the differential equations for the lateral belt displacement become

$$\begin{aligned} -k_{Py}v_b'' + (k_{Wy} + k_{ty})v_b &= k_{ty}v_t && (\bar{x} < x < a), \\ -k_{Py}v_b'' + k_{Wy}v_b &= \pm\mu_k p_z && (0 < x < \bar{x}), \\ -k_{Py}v_b'' + k_{Wy}v_b &= 0 && (x < -a \text{ or } x > a) \end{aligned} \tag{2.46}$$

If $s_y > 0$ the upper sign has to be chosen and the lower sign in the other case. The displacement of the bristles is prescribed for the adhesion region and the force is prescribed for the sliding region. The solutions in the outside regions have the same form as the equations in Equation 2.29, where w gets replaced by v and κ_{zo} by $\kappa_{yo} = (k_{Wy}/k_{Py})^{1/2}$. This gives the following boundary conditions:

$$\kappa_{yo}v_b(a) + v_b'(a) = 0, \quad \kappa_{yo}v_b(-a) - v_b'(-a) = 0. \tag{2.47}$$

The stationary solution in the adhesion region becomes

$$\begin{aligned} v_{b,s}(x) &= C_{y1}\cosh(\kappa_{yi}x) + C_{y2}\sinh(\kappa_{yi}x) \\ &+ \left(1 - \frac{\kappa_{yo}^2}{\kappa_{yi}^2}\right)\left(v_{b,s}(a) - (a-x)s_y + (a^2 - x^2)\frac{s_n}{2R_b} - \frac{s_n}{\kappa_{yi}^2 R_b}\right) \qquad (\bar{x} < x < a), \end{aligned} \tag{2.48}$$

in which $\kappa_{yi} = [(k_{Wy} + k_{ty})/k_{Py}]^{1/2}$ and C_{y1} and C_{y2} are constants that will be determined from the boundary conditions. The value $v_{b,s}(a)$ can be expressed in terms of the constants as

$$v_{b,s}(a) = \frac{\kappa_{yi}^2}{\kappa_{yo}^2}\left[C_{y1}\cosh(\kappa_{yi}a) + C_{y2}\sinh(\kappa_{yi}a) - \left(1 - \frac{\kappa_{yo}^2}{\kappa_{yi}^2}\right)\frac{s_n}{\kappa_{yi}^2 R_b}\right]. \tag{2.49}$$

When this value gets substituted in Equation 2.48, the following equation is obtained:

$$\begin{aligned} v_{b,s}(x) = C_{y1}&\left[\cosh(\kappa_{yi}x) + \left(\frac{\kappa_{yi}^2}{\kappa_{yo}^2} - 1\right)\cosh(\kappa_{yi}a)\right] \\ &+ C_{y2}\left[\sinh(\kappa_{yi}x) + \left(\frac{\kappa_{yi}^2}{\kappa_{yo}^2} - 1\right)\sinh(\kappa_{yi}a)\right] \\ &+ \left(1 - \frac{\kappa_{yo}^2}{\kappa_{yi}^2}\right)\left(-(a-x)s_y + (a^2 - x^2)\frac{s_n}{2R_b} - \frac{s_n}{\kappa_{yo}^2 R_b}\right) \qquad (\bar{x} < x < a). \end{aligned} \tag{2.50}$$

The solution for the sliding region is

$$\begin{aligned} v_{b,s} = C_{y3}\cosh(\kappa_{yo}x) + C_{y4}\sinh(\kappa_{yo}x) \pm \mu_k \frac{k_{tz}}{k_{Wy}}&\left[C_z \frac{\kappa_{yo}^2}{\kappa_{zi}^2 - \kappa_{yo}^2}\cosh(\kappa_{zi}x)\right. \\ \left. + \left(1 - \frac{\kappa_{zo}^2}{\kappa_{zi}^2}\right)\frac{1}{\kappa_{zi}^2 R_b} + \frac{\kappa_{zo}^2}{\kappa_{zi}^2}\left(\epsilon_n - \frac{x^2}{2R_b} - \frac{1}{\kappa_{yo}^2 R_b}\right)\right] &\qquad (-a < x < \bar{x}). \end{aligned} \tag{2.51}$$

It can be assumed that $\kappa_{zi} > \kappa_{yo}$. The four constants C_{y1}, C_{y2}, C_{y3} and C_{y4} are determined by the boundary condition from Equation 2.46 and the conditions that the displacement and the slope of the belt are continuous at $x = \bar{x}$. After solving the equations for the four constants, the stationary lateral force distribution can be written as

$$\begin{aligned} p_{y,s}(x) &= \pm\mu_k p_z(x) \\ &= \pm\mu_k k_{tz}\left[-C_z\cosh(\kappa_{zi}x) + \left(1 - \frac{\kappa_{zo}^2}{\kappa_{zi}^2}\right)\frac{1}{\kappa_{zi}^2 R_b}\right. \\ &\quad \left. + \frac{\kappa_{zo}^2}{\kappa_{zi}^2}\left(\epsilon_n - \frac{x^2}{2R_b}\right)\right] \qquad (-a < x < \bar{x}), \\ p_{y,s}(x) &= k_{ty}(v_b - v_t) \\ &= k_{ty}C_{y1}(\cosh(\kappa_{yi}x) - \cosh(\kappa_{yi}a)) + k_{ty}C_{y2}(\sinh(\kappa_{yi}x) - \sinh(\kappa_{yi}a)) \\ &\quad + k_{ty}\frac{\kappa_{yo}^2}{\kappa_{yi}^2}\left((a-x)s_y - (a^2 - x^2)\frac{s_n}{2R_b}\right) \qquad (\bar{x} < x < a). \end{aligned} \tag{2.52}$$

The condition for the transition point $\bar{x}$ is

$$p_{y,s}(\bar{x}^+) = \mu_s p_z(\bar{x}). \tag{2.53}$$

The stationary lateral force can now be calculated by the following integral:

$$F_{y,s} = \int_{-a}^{a} p_{y,s}(x)dx = \int_{-a}^{\bar{x}} p_{y,s}(x)dx + \int_{\bar{x}}^{a} p_{y,s}(x)dx. \tag{2.54}$$

The aligning moment can be found by:

$$M_{z,s} = -\int_{-a}^{a} x p_{y,s}(x)dx = -\int_{-a}^{\bar{x}} x p_{y,s}(x)dx - \int_{\bar{x}}^{a} x p_{y,s}(x)dx. \tag{2.55}$$

As might be recalled from the previous section, to find the values of the parameters of this model for the tested tyres by Dressel, these last two equations have to be rewritten. The cornering stiffness is defined as:

$$C_{F_\alpha} = \left(\frac{\partial F_{y,s}}{\partial s_y}\right)_{s_y=0} \tag{2.56}$$

Secondly, the self-aligning moment stiffness is:

$$C_{M_\alpha} = -\left(\frac{\partial M_{z,s}}{\partial s_y}\right)_{s_y=0} \tag{2.57}$$

And lastly, the spin stiffness is defined as:

$$C_{F_\varphi} = \left(\frac{\partial F_{y,s}}{\partial s_n}\right)_{s_n=0} \tag{2.58}$$

So in order to find the relation between the cornering stiffness and the model parameters, the partial derivative of the following formula to the slip angle will be taken:

$$\begin{aligned} F_{y,s} = & \int_{-a}^{\bar{x}} \pm\mu_k k_{tz}\left[-C_z\cosh(\kappa_{zi}x) + \left(1-\frac{\kappa_{zo}^2}{\kappa_{zi}^2}\right)\frac{1}{\kappa_{zi}^2 R_b} + \frac{\kappa_{zo}^2}{\kappa_{zi}^2}\left(\epsilon_n - \frac{x^2}{2R_b}\right)\right]dx \\ & + \int_{\bar{x}}^{a}\Bigg[k_{ty}C_{y1}(\cosh(\kappa_{yi}x)-\cosh(\kappa_{yi}a)) + k_{ty}C_{y2}(\sinh(\kappa_{yi}x)-\sinh(\kappa_{yi}a)) \\ & + k_{ty}\frac{\kappa_{yo}^2}{\kappa_{yi}^2}\left((a-x)s_y - (a^2-x^2)\frac{s_n}{2R_b}\right)\Bigg]dx \end{aligned} \tag{2.59}$$

The first integral doesn't contain terms with the slip angle s_y, such that the following integral is obtained:

$$\begin{aligned} \left(\frac{\partial F_{y,s}}{\partial s_y}\right)_{s_y=0} = & \int_{\bar{x}}^{a}\Bigg[k_{ty}\frac{\partial C_{y1}}{\partial s_y}(\cosh(\kappa_{yi}x)-\cosh(\kappa_{yi}a)) \\ & + k_{ty}\frac{\partial C_{y2}}{\partial s_y}(\sinh(\kappa_{yi}x)-\sinh(\kappa_{yi}a)) + k_{ty}\frac{\kappa_{yo}^2}{\kappa_{yi}^2}(a-x)\Bigg]dx \end{aligned} \tag{2.60}$$

Unlike the expression for $\partial C_z/\partial\epsilon_n$, the expression for $\partial C_{y1}/\partial s_y$ and $\partial C_{y2}/\partial s_y$ are very lengthy expressions. Therefor the complete equation for the cornering stiffness is even longer and it won't be shown here. The equation is obtained using the symbolic toolbox in Matlab, since it is impossible to obtain it by hand without making mistakes. This equation can be used to link the measurement data from Dressel to the model parameters $\kappa_{yo} = (k_{Wy}/k_{Py})^{1/2}$ and $\kappa_{yi} = [(k_{Wy}+k_{ty})/k_{Py}]^{1/2}$.

A similar expression can be found for the self-aligning moment and the normal spin. The expression for the self-aligning moment is:

$$\begin{aligned} M_{z,s} = & \int_{-a}^{\bar{x}} \pm\mu_k k_{tz}x\left[-C_z\cosh(\kappa_{zi}x) + \left(1-\frac{\kappa_{zo}^2}{\kappa_{zi}^2}\right)\frac{1}{\kappa_{zi}^2 R_b} + \frac{\kappa_{zo}^2}{\kappa_{zi}^2}\left(\epsilon_n - \frac{x^2}{2R_b}\right)\right]dx \\ & + \int_{\bar{x}}^{a} x\Bigg[k_{ty}C_{y1}(\cosh(\kappa_{yi}x)-\cosh(\kappa_{yi}a)) + k_{ty}C_{y2}(\sinh(\kappa_{yi}x)-\sinh(\kappa_{yi}a)) \\ & + k_{ty}\frac{\kappa_{yo}^2}{\kappa_{yi}^2}\left((a-x)s_y - (a^2-x^2)\frac{s_n}{2R_b}\right)\Bigg]dx \end{aligned} \tag{2.61}$$

Here again the first integral does not contain the slip term. The self-aligning moment stiffness becomes:

$$\begin{aligned} \left(\frac{\partial M_{z,s}}{\partial s_y}\right)_{s_y=0} = & \int_{\bar{x}}^{a} x\Bigg[k_{ty}\frac{\partial C_{y1}}{\partial s_y}(\cosh(\kappa_{yi}x)-\cosh(\kappa_{yi}a)) \\ & + k_{ty}\frac{\partial C_{y2}}{\partial s_y}(\sinh(\kappa_{yi}x)-\sinh(\kappa_{yi}a)) + k_{ty}\frac{\kappa_{yo}^2}{\kappa_{yi}^2}(a-x)\Bigg]dx \end{aligned} \tag{2.62}$$

Also this equation contains the lengthy expressions for $\partial C_{y1}/\partial s_y$ and $\partial C_{y2}/\partial s_y$. The complete expression for the self-aligning torque stiffness is even longer than the expression for the cornering stiffness, so it also won't be shown here. This equation is also found with the Matlab symbolic toolbox.

Lastly the expression for the spin stiffness will be derived. As can be seen in Equation 2.59, the first integral does not contain a term with the normal spin s_n, such that the following equation is obtained:

$$\begin{aligned} \left(\frac{\partial F_{y,s}}{\partial s_n}\right)_{s_n=0} = & \int_{\bar{x}}^{a}\Bigg[k_{ty}\frac{\partial C_{y1}}{\partial s_n}(\cosh(\kappa_{yi}x)-\cosh(\kappa_{yi}a)) \\ & + k_{ty}\frac{\partial C_{y2}}{\partial s_n}(\sinh(\kappa_{yi}x)-\sinh(\kappa_{yi}a)) - k_{ty}\frac{\kappa_{yo}^2}{\kappa_{yi}^2}\left(\frac{(a^2-x^2)}{2R_b}\right)\Bigg]dx \end{aligned} \tag{2.63}$$

The complete equation will be derived with the symbolic toolbox in Matlab to prevent mistakes and save time. The complete equation is again too long to show here.

2.4. Non-smooth delayed contact model

In this section the non-smooth delayed contact model will be discussed. The non-smooth delayed contact model is based on the stretched-string model. Beregi studied the vibrations of a towed wheel excited by the lateral deformation of the tyre [10]. The time delay in the tyre-ground contact as well as the partial side slip are considered making it possible to capture the dynamic deformation of the contact patch centre-line with relatively low parameters and computation time. This tyre model can identify the hysteresis effect in the stability of the rectilinear motion by numerical simulations, which is not possible with the simpler quasi steady-state tyre models.

Theory of the non-smooth delayed contact model

The most commonly used tyre models are assuming quasi steady-state deformation in the contact patch. This makes it possible to introduce tyre force and aligning moment characteristics, which works well for larger speeds [1] [11]. However, for low or medium velocities these models tend to be less accurate, because the memory-effect associated to the time-delay becomes more relevant in the contact patch [12] [13]. A solution to capture this behaviour is to use additional degrees of freedom besides addressed to certain dynamic features of the tyre together with the tyre force characteristics [14]. This solution is implemented in several models, but due to the higher number of parameters these might be found less convenient for a qualitative analysis of tyre dynamics. Another solution is to use continuum-based tyre models which are capable to describe the travelling waves in the rolling tyre-ground contact. The problem is that these models lead to partial differential equations, which can be computationally costly to solve.

Beregi selected the stretched-string tyre model for his study, which can be a good compromise in this respect since for pure rolling the deformation is described by a single partial differential equation whereas it takes into account the tyre deformation outside the contact patch too, which, like mentioned before, has a relevant effect in the low velocity range. A travelling wave solution can be composed analytically for the nonlinear partial differential equation by introducing time delay distributed along the contact length. However, the travelling wave solution cannot capture the sliding effect caused by friction in the contact region. Thus, while it can be effectively used for linear stability analysis, to investigate the nonlinear dynamics it has to be enhanced by taking the side slip into account too.

Taking the memory effect and the contact friction into account simultaneously in the tyre-road contact can result in a complex structure of sticking and sliding regions, as for the stretched-string model in particular, the deformation in the sliding parts is described by differential equations [15]. Beregi mentions that in contact mechanics several studies revealed a similar structure of sticking and sliding regions in the frictional contact of elastic continua [16]. In his study Beregi introduces a case-selective algorithm to determine the boundaries and the deformation in the different regions that can occur while the tyre makes lateral vibrations. Then the non-smooth delayed tyre model is implemented in the numerical simulation of a towed wheel. By obtaining the stable periodic solutions in the system he demonstrates the hysteresis effect observed in practice regarding the stability of the rectilinear motion.

2.4.1. Equations of a shimmying wheel

In their study they implement their tyre model into the in-plane model of a towed wheel attached to a rigid caster of length l, which is towed by a constant velocity V along the x-direction. The system has mass m and mass moment of inertia J_A with respect to the joint A. The deflection angle $\psi(t)$ can be used as a generalised coordinate to describe the position of the system in the (X,Y) coordinate-plane. To the king pin J a torsional damper with a damping coefficient of d_t is attached. All this is shown in Figure 2.8.

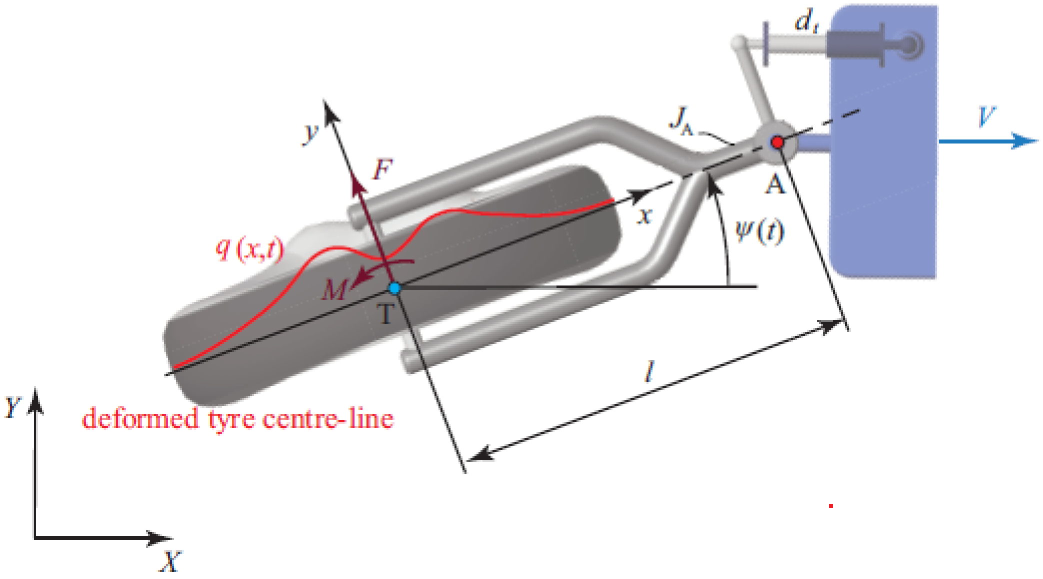

Figure 2.8: The in-plane model of a towed wheel with a rigid caster [8].

The equation of motion of the yaw vibrations of the wheel are as follows:

$$J_A\ddot{\psi}(t) + d_t\dot{\psi}(t) = M - Fl \tag{2.64}$$

where F and M are lateral contact force and aligning torque respectively. They are generated by the tyre deformation. The dots refer to time-derivatives.

2.4.2. Non-smooth delayed model of the tyre-ground contact

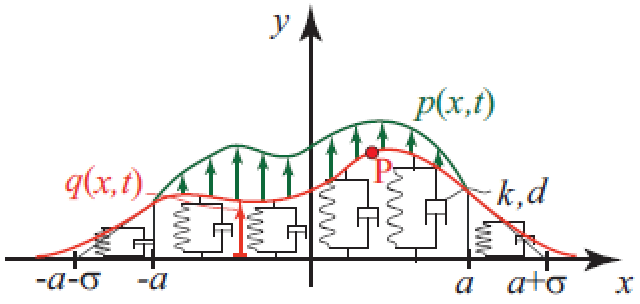

Figure 2.9: The stretched-string tyre model [9].

The tyre forces are calculated with the stretched-string tyre model, this is similar to the model from previous chapter. The difference is that instead of having only linearly distributed spring elements, this model also has linearly distributed damper elements. It is assumed that tyre damping is large enough not to allow deformation waves travelling around the wheel to have significant interference with the deformation at the leading edge $x = a$. The tyre model is shown in Figure 2.9. In the contact patch a distributed force system of $p(x,t)$ is applied to the string resulting in the deformation of the tyre, whereas outside the contact patch the tyre is assumed to be unloaded in lateral direction. The lateral deformation of the string can be described by the following partial differential equation:

$$k\sigma^2 q''(x,t) - d\dot{q}(x,t) - kq(x,t) = p(x,t) \tag{2.65}$$

---

[8] Image is taken from [10].

[9] Image is taken from [10].

where q(x,t) is the lateral deformation of the string and σ is the tyre relaxation length. Primes refer to derivatives with respect to coordinate x. The tyre forces are calculated according to the classical stretched-string model by integral formulae

$$F = k\int_{-\infty}^{\infty} q(x,t)dx + d\int_{\infty}^{\infty} \frac{d}{dt}q(x,t)dx \tag{2.66}$$

and

$$M = k\int_{-\infty}^{\infty} xq(x,t)dx + d\int_{\infty}^{\infty} x\frac{d}{dt}q(x,t)dx. \tag{2.67}$$

Contact patch deformation in case of pure rolling

When the tyre is purely rolling and there is no side-slip, the tyre is assumed to stick to the ground and the tyre centre-line to have zero relative velocity in the contact patch. The is formulated in the following kinematic constraint:

$$\frac{d}{dt}R_p = 0 \tag{2.68}$$

where R_p is the position vector of an arbitrary point P of the contact patch centre-line in the ground-fixed frame of reference. A nonlinear partial differential equation can be derived which describes the lateral deformation in the contact patch based on this vector

$$\dot{q}(x,t) = V\sin(\psi(t)) + (l-x)\dot{\psi}(t) - q'(x,t)\big(q(x,t)\dot{\psi}(t) - V\cos(\psi(t))\big). \tag{2.69}$$

For this equation a travelling wave solution can be composed, which yields to a formula with a time delay of $\tau(x)$ distributed along the contact region

$$q(x(\tau),t) = V\tau\sin(\psi(t)) - (a-l)\sin(\psi(t)-\psi(t-\tau)) + q(a,t-\tau)\cos(\psi(t)-\psi(t-\tau)) \tag{2.70}$$

while the longitudinal distribution of the time delay $\tau(x)$ can also be expressed. Thus, for the coordinate x the following is obtained

$$x(\tau) = -V\tau\cos(\psi(t))l + (a-l)\cos(\psi(t)-\psi(t-\tau)) + q(a,t-\tau)\sin(\psi(t)-\psi(t-\tau)). \tag{2.71}$$

It is reasonable to assume that no discontinuity in the deformed shape arises at the leading edge $(x=a)$ where the tyre particles first touch the ground, since the tyre is rolling. This is formulated in the following boundary condition

$$q'(a,t) = -\frac{q(a,t)}{\sigma}. \tag{2.72}$$

Applying the boundary condition, the ordinary differential equation for the lateral deformation at the leading edge is

$$\dot{q}(a,t) = V\sin(\psi(t)) - (a-l)\dot{\psi}(t) + \frac{q(a,t)}{\sigma}\big(q(a,t)\dot{\psi}(t) - V\cos(\psi(t))\big). \tag{2.73}$$

Partial side-slip in the contact patch

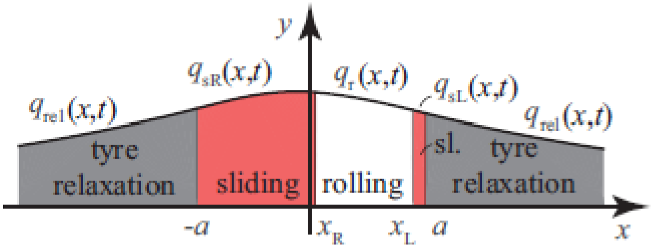

Figure 2.10: The different rolling, sliding and tyre relaxation regions assumed [10].

---

[10] Image is taken from [10].

If the effect of dry friction in the tyre-ground contact is considered, the condition of rolling only limitedly holds as side-slip will occur in those parts of the contact region where the intensity of the distributed force system corresponding to rolling is larger than the limits determined by friction. If the normal-force distribution in the contact region is assumed parabolic, these limits are also defined by parabolas [1]

$$p_{r+}(x) = \frac{3F_z\mu_r}{4a^3}(a^2 - x^2), \tag{2.74}$$

$$p_{r-}(x) = -\frac{3F_z\mu_r}{4a^3}(a^2 - x^2), \tag{2.75}$$

$$p_{s+}(x) = \frac{3F_z\mu_s}{4a^3}(a^2 - x^2), \tag{2.76}$$

$$p_{s-}(x) = -\frac{3F_z\mu_s}{4a^3}(a^2 - x^2), \tag{2.77}$$

where the subscript r and s indicate rolling and sliding respectively. From above it follows that for the rolling part of the contact patch $p(x) \in [p_{r-}(x), p_{r+}(x)]$ should hold.

The limits for the sliding give the distributed force system for the sliding parts of the contact patch in question. Therefore, these can be substituted into Equation 2.65 in order to calculate the deformation in these zones. This partial differential equation is badly-conditioned in terms of the required time-step for numerical simulation, which slows down the computation. Therefore, in the sliding regions the steady-state solutions are used: $q(x,t) = q_s(x,t)$, $\dot{q}(x,t) \equiv 0$ from Equation 2.65 which can be calculated from

$$q_s''(x,t) - \frac{q_s(x,t)}{\sigma^2} = \frac{M}{k\sigma^2}(x^2 - a^2). \tag{2.78}$$

For this differential equation the analytical solution can be provided as

$$q_s(x,t) = C_1 e^{\frac{x}{\sigma}} + C_2 e^{-\frac{x}{\sigma}} + \frac{M}{k}(a^2 - x^2 - 2\sigma^2) \tag{2.79}$$

where the constants C_1 and C_2 can be calculated from the corresponding boundary conditions, which will be discussed later on.

Deformation outside the contact patch

The deformation outside the contact patch $q_{rel}(x,t)$ can be calculated in a similar way as for the sliding parts. A quasi-stationary deformation is assumed as $q(x,t) = q_{rel}(x,t)$, $\dot{q}(x,t) \equiv 0$. It is assumed that there is no lateral load in this region, so Equation 2.65 yields to a homogeneous differential equation:

$$q''_{rel}(x,t) - \frac{q_{rel}(x,t)}{\sigma^2} = 0. \tag{2.80}$$

With the boundary conditions $q_{rel}(a,t) = q_{sL}(a,t)$, $lim_{x\to\infty} q_{rel}(x,t) = 0$ and $q_{rel}(-a,t) = q_{sR}(-a,t)$, $lim_{x\to-\infty} q_{rel}(x,t) = 0$ the deformation outside the contact patch ca be expressed as

$$q_{rel}(x,t) = q_{sR}(-a,t)e^{\frac{a+x}{\sigma}} \text{ for } x \in (\infty, -a], \tag{2.81}$$

and

$$q_{rel}(x,t) = q_{sL}(a,t)e^{\frac{a-x}{\sigma}} \text{ for } x \in [a, \infty). \tag{2.82}$$

Boundary conditions at the sliding regions

Because of simplicity only the cases of sliding regions at the leading edge or the trailing edge are taking into account. The whole contact patch slides when the siding regions merge. According to Beregi it can be shown that this is sufficient for the analysis of wheel-shimmy. Figure 2.10 shows the three different regions in the contact patch: a sliding region at the leading edge ($x \in [x_L, a]$), a rolling region in the middle ($x \in [x_R, x_L]$) and a sliding region at the rear edge ($x \in [-a, x_R]$). In the rolling part the deformation is described by the travelling-wave solution and in the sliding parts Equation 2.78 applies.

Evidently the transition between the regions should be smooth, so no discontinuities should occur. Therefor the following boundary conditions should be true:

$$\begin{aligned} q_r(x_L,t) =& q_{sL}(x_L,t) \\ q_{sR}(x_R,t) =& q_r(x_R,t) \end{aligned} \tag{2.83}$$

The first derivatives with respect to coordinate x of Equation 2.65 should be continues as well. This is included in the following boundary conditions:

$$\begin{aligned} q_r'(x_L,t) =& q_{sL}'(x_L,t) \\ q_{sR}'(x_R,t) =& q_r'(x_R,t) \end{aligned} \tag{2.84}$$

The same is also true for the transitions at the edges of the contact patch which translate to the following boundary conditions:

$$\begin{aligned} q_r'(a,t) &= -\frac{q_{sL}(a,t)}{\sigma} \\ q_{sR}'(-a,t) &= -\frac{q_r(-a,t)}{\sigma} \end{aligned} \tag{2.85}$$

All these boundary conditions lead to an over-constrained problem for the sliding regions since three boundary conditions are formulated for both the sliding parts at the leading and trailing edge, whereas existence and uniqueness of the solution of Equation 2.78 is assured by attaching two boundary conditions. Therefor, the solution will be found by varying the boundaries of the sliding regions x_L and x_R, using the boundary conditions from 2.83 and 2.85 in Equation 2.78 and the conditions from 2.84 are used to find the boundaries between the rolling ans sliding regions.

2.5. Selecting a tyre model

Now that several tyre models have been elaborated, a choice will be made. The model parameters from the chosen model will be linked to the measurements done by Dressel and the bachelor group.

2.5.1. Validity of the tyre brush model for bicycle tyres

The tyre brush model has only one material parameter, so more complex tyre structures are harder to model with purely the tyre brush model without extensions. It is expected that the behaviour of a ”simpler” bicycle tyre can be modelled by the tyre brush model with its single material parameter.

This single parameter model also might have a drawback, since the goal is to estimate tyre behaviour in terms of vertical stiffness, cornering stiffness and camber stiffness based on known parameters like inflation pressure, tyre width, rim width and kind of rubber. A single parameter, means that all these known properties are included in this parameter. The ideal situation would be a model parameter for every known tyre parameter.

The formulas derived in section 2.1 show that material parameter c_{py} from the tyre brush model can be calculated from the measurements done by Dressel. So it is possible to find the relation between the tyre behavioural properties and model parameters.

2.5.2. Validity of the Rotta model for bicycle tyres

This model is based on the more simple properties of bicycle tyres. So this model should be valid for bicycle tyres. Also, Papadopoulos shows the comparison between a measured load-compression curve, an analytically and numerical integrated contact patch and it is encouragingly similar. However, Dressel did use the Rotta model in his research to compare his measurements with a tyre model, so using the Rotta model would be repetitive.

The interesting part of this model is that it can show the influence of parameters like rim width, tyre width and height on the vertical and lateral force. This might be useful, since the goal of the thesis is to find out if it is possible to estimate the tyre behaviour in terms of vertical stiffness, cornering stiffness and camber stiffness based on known parameters like the inflation pressure, tyre width, rim width and the kind of rubber. Maybe the results from Dressel can be combined with the results of another model.

2.5.3. Validity of the enhanced string model for bicycle tyres

The formulas derived in section 2.3 show that the material parameters from the model can be calculated from the measurements done by Dressel. Even though the equations are quite extensive, it is possible to find the relation between the tyre behavioural properties and model parameters.

The potential advantage of this model over the tyre brush model is that it has a bit more parameters, so it might be possible to relate the different model parameters to the tyre parameters.

2.5.4. Validity of the non-smooth delayed contact model for bicycle tyres

This model is fairly similar to the enhanced string model. A difference compared to the enhanced string model is that the damping is also taken into account. The vertical pressure distribution is simpler again, just as with the tyre brush model. This might be a disadvantage, because the vertical pressure distribution determines the contact length and the contact length in it's turn is important for the cornering, self-aligning torque and camber stiffness.

Relaxation length

The most important difference of this model is that it also takes into account the relaxation length of the tyre. This is deformation of the string outside of the contact patch, which also generates a force. The relaxation length is an important parameter for wheel-shimmy effect at medium to low speeds[17]. Dressel did some small experiments to validate the relaxation length, but there are no exact values reported for each tyre, pressure and load combination. There are several methods or rule of thumb to calculate/estimate the relaxation length [18] [19]. This might be useful for future calculations.

2.5.5. Tyre model to be used

The tyre models that will be used are the brush tyre model and the enhanced string model. The brush tyre model will be used because it is fairly simple, so not too much work to find the relation between the model parameter and the measurements. The results might interesting and not using it might be regrettable. After that the enhanced string model will used. This will be done because each of the different model parameters might have a one on one relation to a known tyre parameters. The non-smooth delayed contact model won't be used, only in the case that the enhanced string model is working well and further refinement is needed.

3

Investigating the enhanced string model

Before the collected data will be analysed using this model, an investigation of the model's way of working will be done. This is necessary to get a better understanding of the model. A feeling has to be developed for the model parameter range and how they influence the model output, which is useful for determining if the results are meaningful. This is not needed for the tyre brush model since that model only contains a single parameter and its influence on the cornering stiffness is obvious. The enhanced string model has more parameters and also more complex equations. Moreover, some assumptions have to be made in order to obtain results with this model. The assumptions that are made will be explained and supported with arguments in this chapter.

3.1. Normal force distribution

The enhanced string model requires a few inputs in order to calculate the pressure distribution, vertical force and the contact length. These inputs are: vertical deflection ϵ_n, material parameters k_{Pz}, k_{Wz} and k_{tz} and the undeformed belt radius R_b. The undeformed belt radius is the same for every tested tyre by Dressel, so this input will be kept constant at 0.34 m in the following investigation of parameter influence. Another parameter that needs to be mentioned before investigating the enhanced string model is k_{tz}. This parameter represents the normal stiffness of the bristles. Since the bristles are attached to the foundation, it is assumed that these bristles represent the rubber tread that is in touch with the ground. This means that changing the stiffness shouldn't influence the total vertical stiffness too much, hence leaves the pressure distribution more or less unaffected. For example, think about knobby tyres, where only the knobs are in touch with the ground. If these knobs would have an infinitely high stiffness or no stiffness at all, this wouldn't change anything to the stiffness of the foundation. Now, looking at the formulas of the enhanced string model, this cannot be true. So the influence of k_{tz} will also be investigated, but for the investigation of the influence of other parameters the k_{tz} will be kept constant at $8 \cdot 10^6$ N m^{-2}. This is the same value as used in the paper by Meijaard.

First the influence of the vertical deflection ϵ_n of the tyre on the outputs will be discussed. The relevant input and output values are shown in Table 3.1, where the changing input is in bold font. In Figure 3.1 it can be seen that as the tyre will be deflected more, the force and the contact patch length increase. This is logical, since it just corresponds to a higher normal load. So the influence of the vertical deflection is exactly as expected.

The following two graphs are more interesting, because it tells more about how the two parameters affect the pressure distribution. As explained by Meijaard [9], k_{Pz} is the shear stiffness of the foundation and k_{Wz} is the normal stiffness of the foundation. The influence of k_{Pz} on the pressure distribution is shown in Figure 3.2. As k_{Pz} increases the contact patch decreases and the shape of the pressure distribution changes. The normal force also increases, which is expected since more force is required to obtain the same vertical deflection. An interesting observation is done for when k_{Pz} exceeds a certain value, because it seems that the shape of the pressure distribution cannot change anymore.

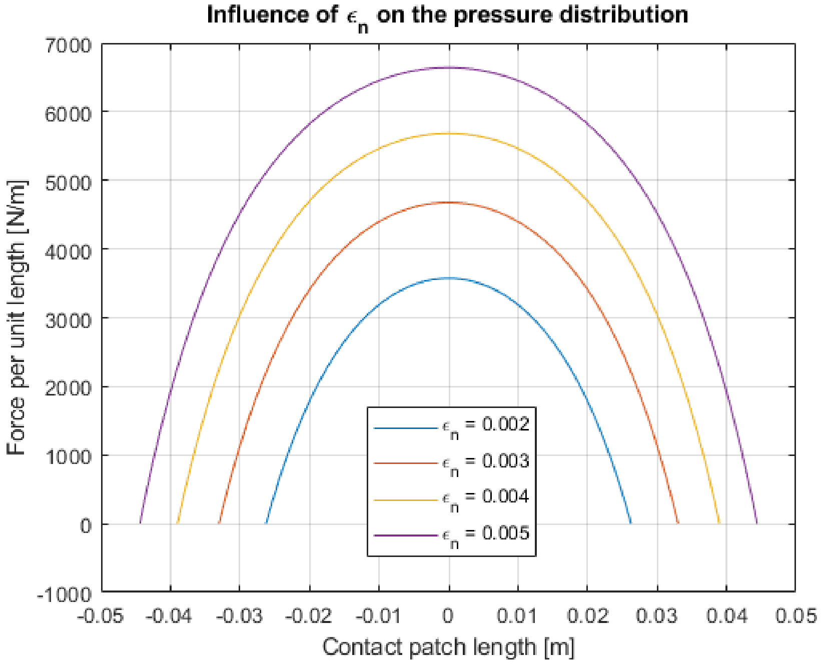

Figure 3.1: Influence of ϵ_n on the pressure distribution.

This means that the contact patch length increases after this certain value of k_{Pz}. It is suspected that such high values of k_{Pz} are not realistic and that it should be more in the region of 100-1000 N. These forces seem to be more reasonable for pre-tension in the tyres.

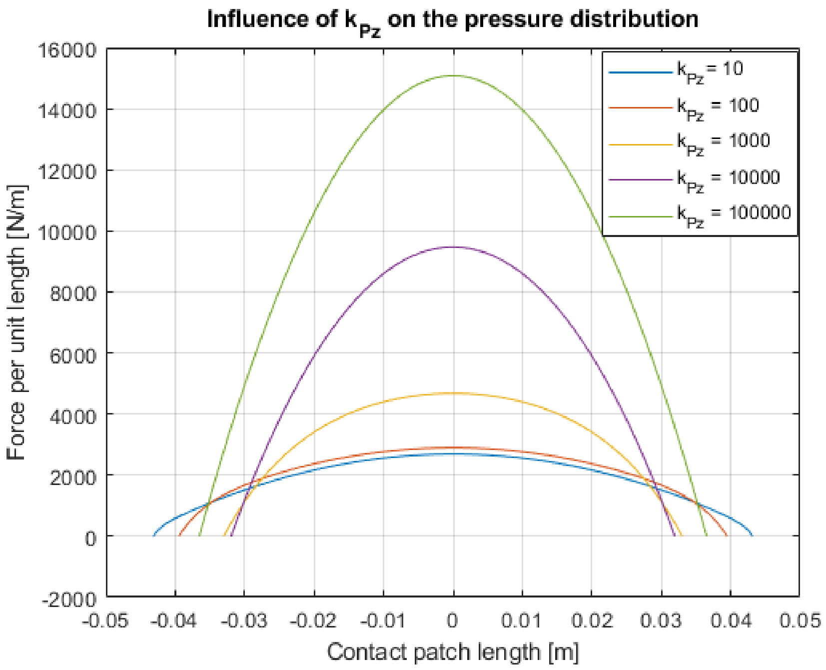

Figure 3.2: Influence of k_{Pz} on the pressure distribution.

The effect of increasing k_{Wz} on the pressure distribution is depicted in Figure 3.3. An increased normal stiffness requires more normal force to obtain the same deflection. Also the contact patch length increases.

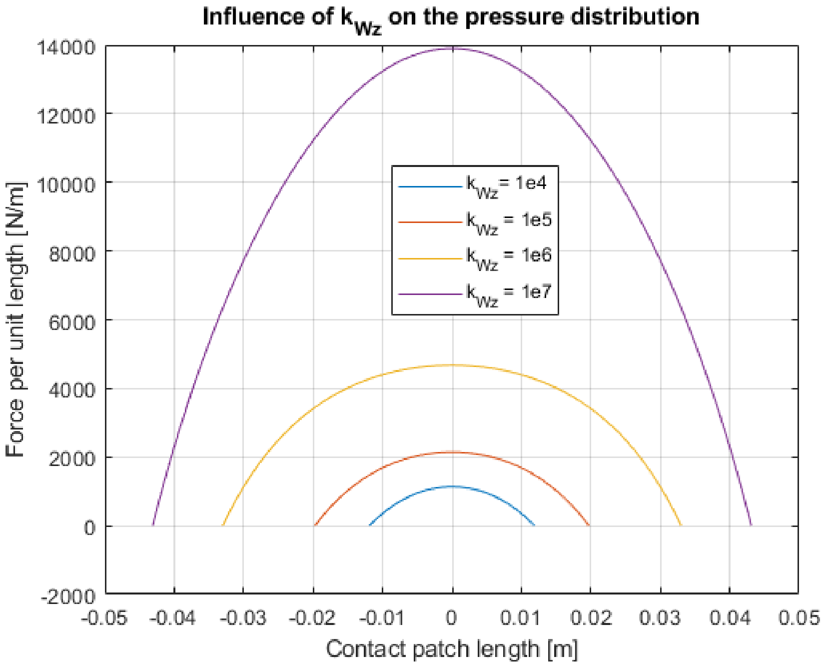

Figure 3.3: Influence of k_{Wz} on the pressure distribution.

Inputs				Outputs	
$\epsilon_n(m)$	$k_{Pz}(N)$	$k_{Wz}(Nm^{-2})$	$k_{tz}(Nm^{-2})$	$F_z(kg)$	$2a(m)$
0.002	1000	1e6	8e6	13.56	0.052
0.003	1000	1e6	8e6	22.76	0.066
0.004	1000	1e6	8e6	33.11	0.078
0.005	1000	1e6	8e6	44.49	0.089
0.003	**10**	1e6	8e6	16.47	0.086
0.003	**100**	1e6	8e6	17.28	0.079
0.003	**1000**	1e6	8e6	22.76	0.066
0.003	**10000**	1e6	8e6	41.65	0.064
0.003	**100000**	1e6	8e6	75.01	0.073
0.003	1000	**1e4**	8e6	1.87	0.024
0.003	1000	**1e5**	8e6	6.00	0.040
0.003	1000	**1e6**	8e6	22.76	0.066
0.003	1000	**1e7**	8e6	84.02	0.086

Table 3.1: Inputs and outputs used for creating the several figures.

From Figures 3.2 and 3.3 and Table 3.1 a reasonable value range for material parameters k_{Pz} and k_{Wz} can be extracted for matching it to the measurements done by the Bachelor group and Dressel. However, a big side note has to be placed with that, because it turns out that k_{tz} is influencing the pressure distribution a lot. This is depicted in Figure 3.4. For k_{Pz} = 100 N and k_{Pz} = 1000 N, as k_{Wz} increases, the normal load differs more for the different values of k_{tz}. The opposite is true for k_{Pz} = 10000 N. Where is was expected that the normal stiffness of the bristles didn't influence the pressure distribution too much. Also, the shapes of all the pressure distribution with k_{tz} from around $8 \cdot 10^7$ N m^{-2} and higher do not look realistic. In 'The Pneumatic Tire' [20] on page 262 and 264, measured pressure distributions are depicted and they do not have an (almost) vertical line at the beginning and end of the contact patch. So it will be assumed that the $8 \cdot 10^6$ N m^{-2} for k_{tz} used by Meijaard is a reasonable value that also can be used for this research.

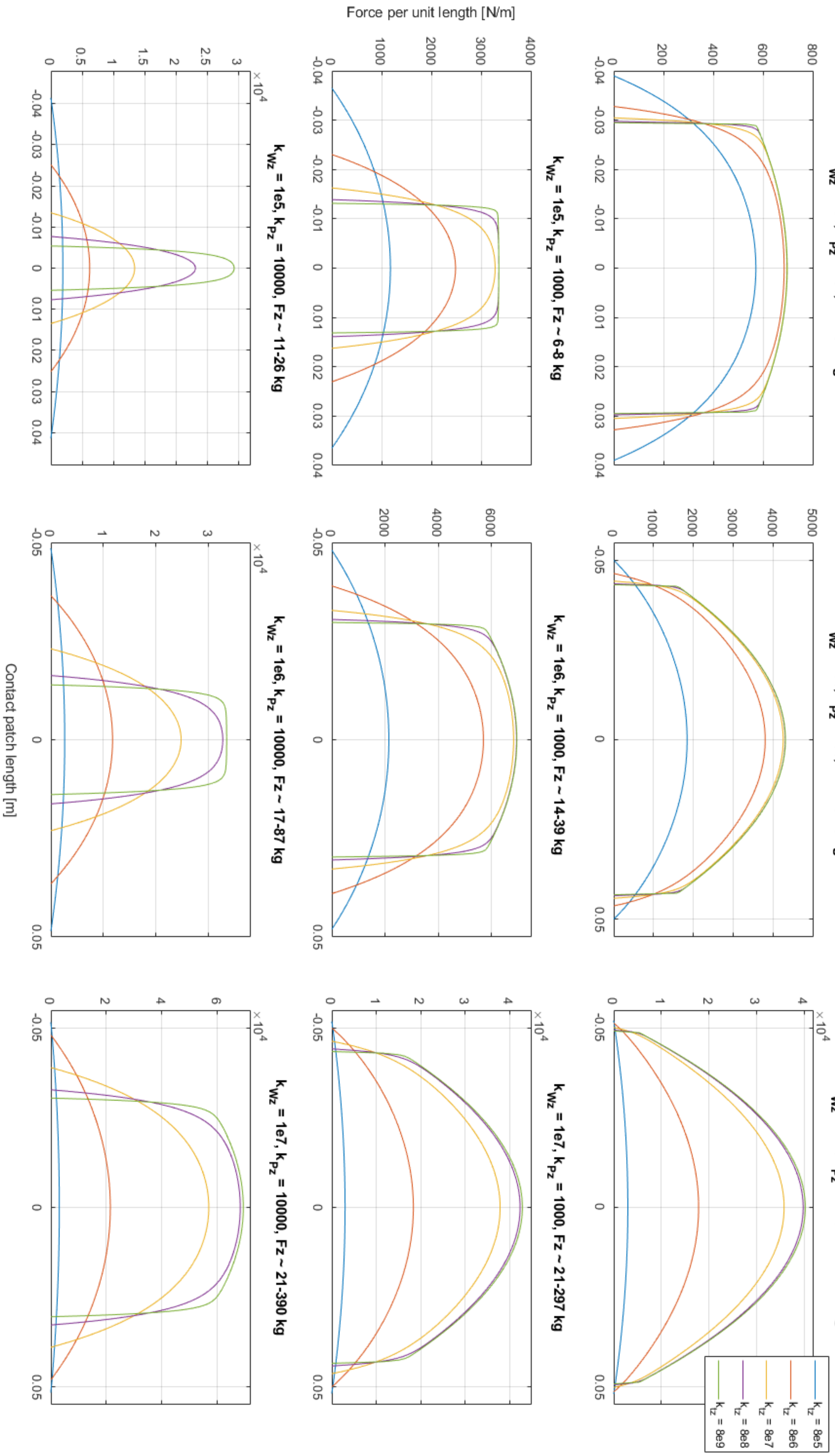

Figure 3.4: Influence of k_{tz} on the pressure distribution. The k_{Pz} is increased for every row and the k_{Wz} is increased for every column. Also the normal load is displayed between the lowest line and the highest line.

3.1.1. A closer look at the equation for the pressure distribution

Some behaviour seen in previous graphs might be hard to explain when you think about the physics. For example, the k_{Pz} that exceeds a certain value such that the contact length will increase. To investigate these behaviours, a few other figures are created. Recall that the equation for the pressure distribution is:

$$p_z = k_{tz}\left[-C_z\cosh(\kappa_{zi}x) + \left(1-\frac{\kappa_{zo}^2}{\kappa_{zi}^2}\right)\frac{1}{\kappa_{zi}^2 R_b} + \frac{\kappa_{zo}^2}{\kappa_{zi}^2}\left(\epsilon_n - \frac{x^2}{2R_b}\right)\right] \qquad (-a < x < a). \tag{3.1}$$

Equation 3.1 for the pressure distribution contains 3 different terms.

$$\begin{aligned} \text{term 1} &= k_{tz}\Big(-C_z\cosh(\kappa_{zi}x)\Big) \\ \text{term 2} &= k_{tz}\left(1-\frac{\kappa_{zo}^2}{\kappa_{zi}^2}\right)\frac{1}{\kappa_{zi}^2 R_b} \\ \text{term 3} &= k_{tz}\frac{\kappa_{zo}^2}{\kappa_{zi}^2}\left(\epsilon_n - \frac{x^2}{2R_b}\right) \end{aligned} \tag{3.2}$$

In these equations $\kappa_{zo} = (k_{Wz}/k_{Pz})^{1/2}$ and $\kappa_{zi} = [(k_{Wz}+k_{tz})/k_{Pz}]^{1/2}$. The influence of these 3 terms for an increasing k_{Pz} can be seen in Figures 3.5, 3.6, 3.7 and 3.8. As can be seen the influence of the third term for a low k_{Pz} is relatively big and decreases as this parameter increases in value. Also, the shape of the first term changes as the k_{Pz} increases.

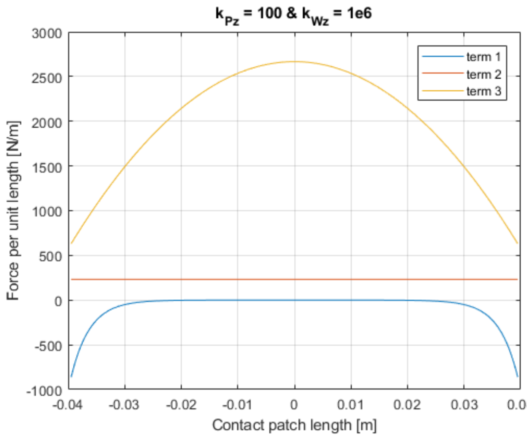

Figure 3.5: k_{Pz} = 100 N

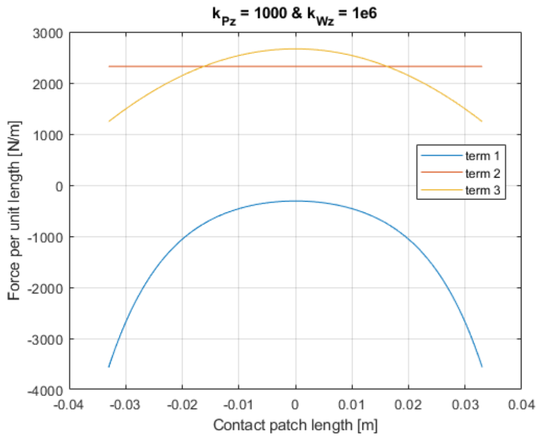

Figure 3.6: k_{Pz} = 1000 N

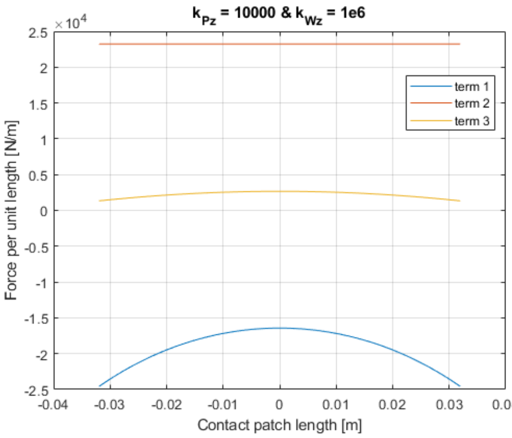

Figure 3.7: k_{Pz} = 10000 N

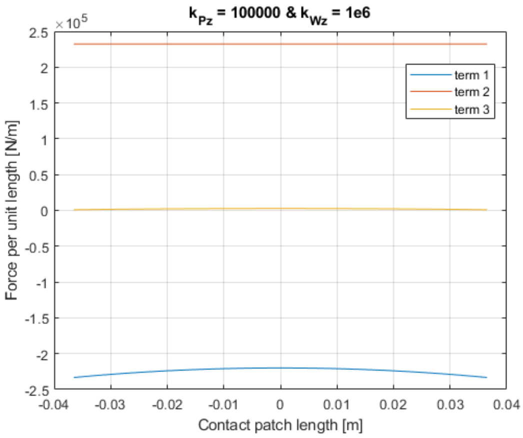

Figure 3.8: k_{Pz} = 100000 N

Now for a relatively low k_{Wz} the influence of the third term is small and starts to dominate when k_{Wz} grows larger, which can be seen in Figures 3.9, 3.10 and 3.11. This is the exact opposite of the influence of k_{Pz}. In both cases the first term gets affected but not by a large amount. Increasing the k_{Wz} has the same influence on the first term as decreasing the k_{Pz}, which can be seen from Equation 3.2.

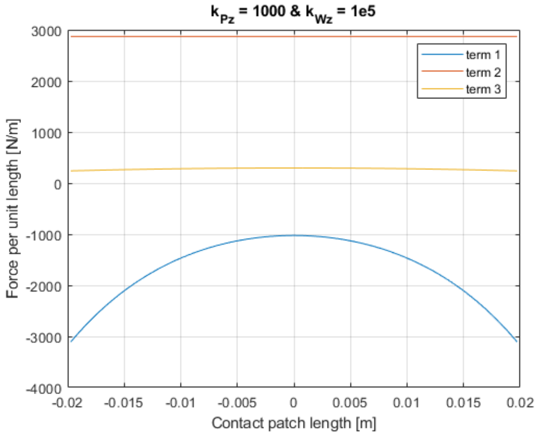

Figure 3.9: k_{Wz} = 1e5 N m^{-2}

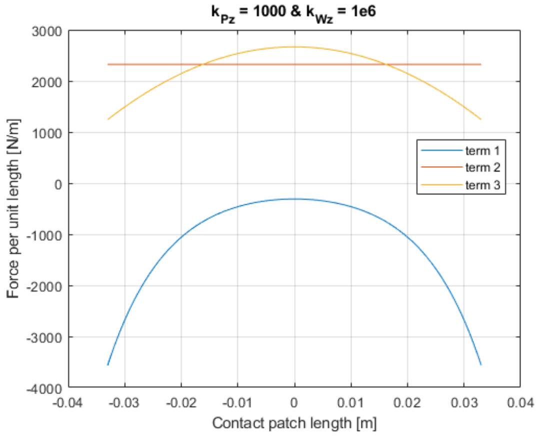

Figure 3.10: k_{Wz} = 1e6 N m^{-2}

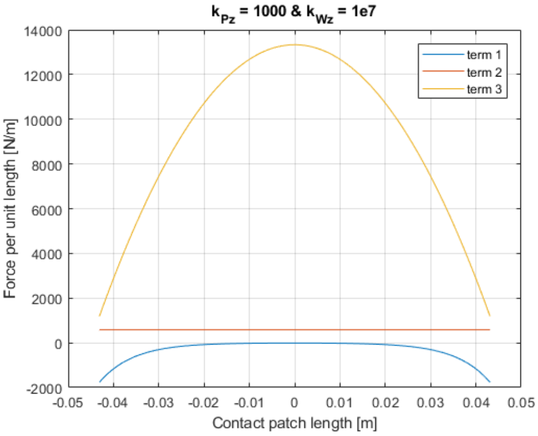

Figure 3.11: k_{Wz} = 1e7 N m^{-2}

Lastly the influence of k_{tz} on the different terms in the pressure distribution is shown in Figures 3.12, 3.13, 3.14, 3.15 and 3.16. The first term is the most important for the overall shape of the pressure distribution. As discussed before, the (almost) vertical lines at the beginning and end of the contact patch for higher values of k_{tz} are not realistic. So these vertical lines are determined by the first term of the pressure distribution equation. The second and third term are relatively unaffected by altering the k_{tz}.

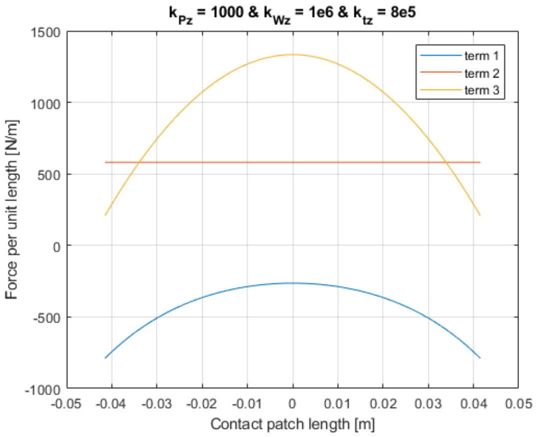

Figure 3.12: k_{tz} = 8e5 N m^{-2}

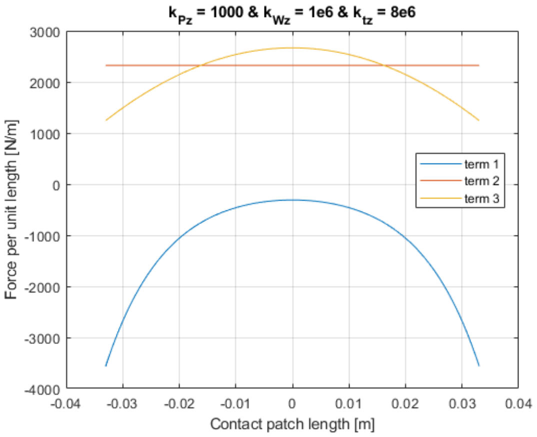

Figure 3.13: k_{tz} = 8e6 N m^{-2}

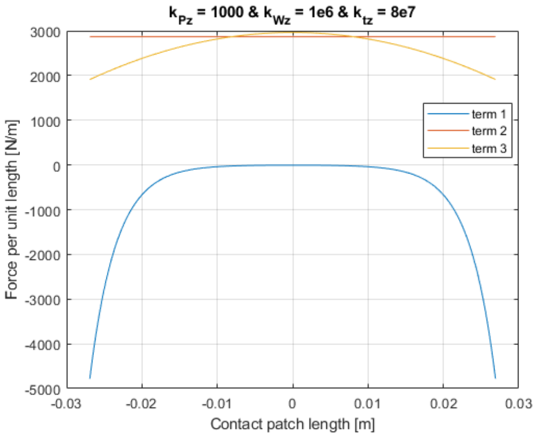

Figure 3.14: k_{tz} = 8e7 N m^{-2}

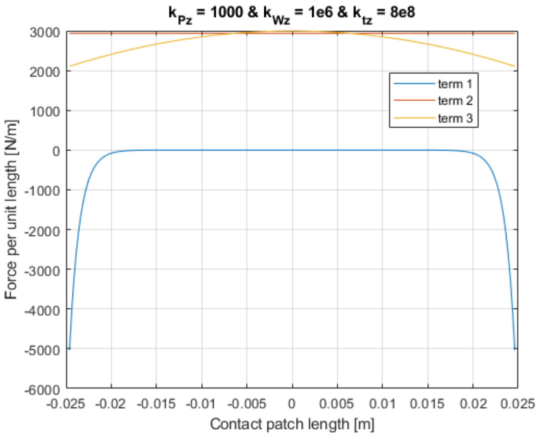

Figure 3.15: k_{tz} = 8e8 N m^{-2}

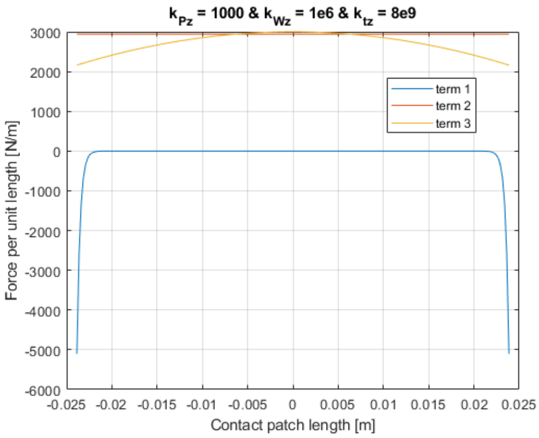

Figure 3.16: k_{tz} = 8e9 N m^{-2}

3.2. Normal load and vertical deflection

The Bachelor group did measurements to determine the vertical stiffness. They concluded that with increasing normal load, the vertical stiffness increases and that this increase in vertical stiffness diminishes [5]. It is interesting to know if the enhanced string model also shows this behaviour. Figures 3.17 and 3.18 contain the normal force as a function the vertical deflection and how k_{Pz} and k_{Wz} influence this respectively.

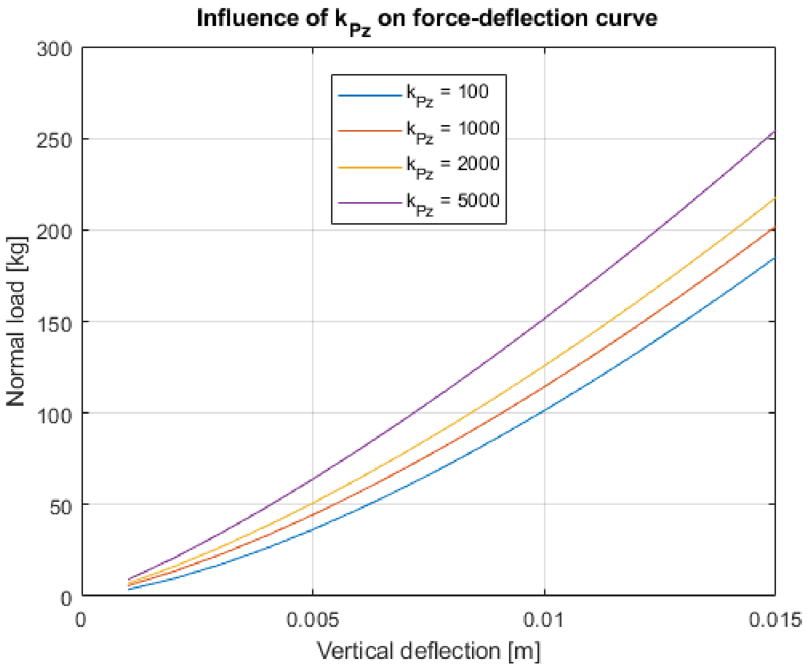

Figure 3.17: Influence of k_{Pz} on the normal load as a function of vertical deflection. k_{Wz} is kept constant at 1e6 N m^{-2}.

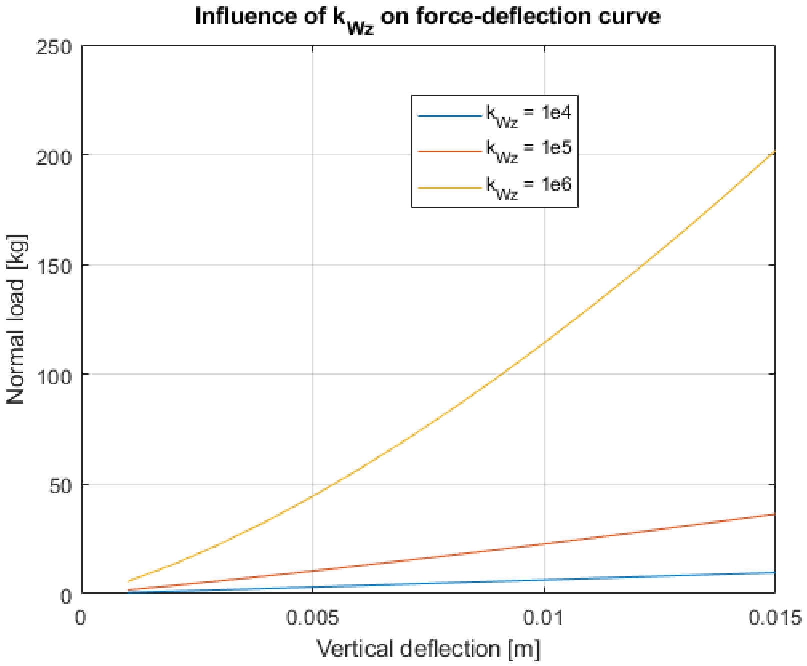

Figure 3.18: Influence of k_{Wz} on the normal load as a function of vertical deflection. k_{Pz} is kept constant at 1000 N.

The influence of k_{Pz} and k_{Wz} on the normal load was already observed in previously shown figures and Table 3.1. This confirms it and gives us a good indication of the parameter values for the tested bicycle tyres. Another observation is that the slope from all the lines is slightly increasing, which indicates that the vertical stiffness is increasing for increasing normal loads. This effect was also observed by the Bachelor group. In Figure 3.19 this effect is depicted more clearly. The different lines are there to show the influence of k_{Pz} and k_{Wz} on this curve.

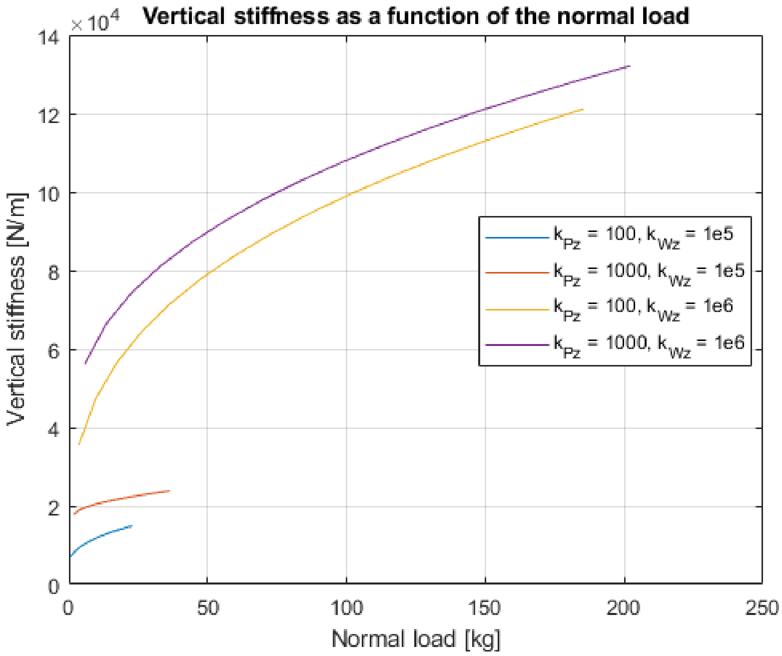

Figure 3.19: Vertical stiffness as a function of the normal load and the influence of k_{Pz} and k_{Wz} on this curve.

Now looking at the graphs that are presented by the Bachelor group, it can be concluded these look quite similar to the graph in Figure 3.19. As an example the vertical stiffness from the Cheng Shin Classic Zeppelin is depicted in Figure 3.20.

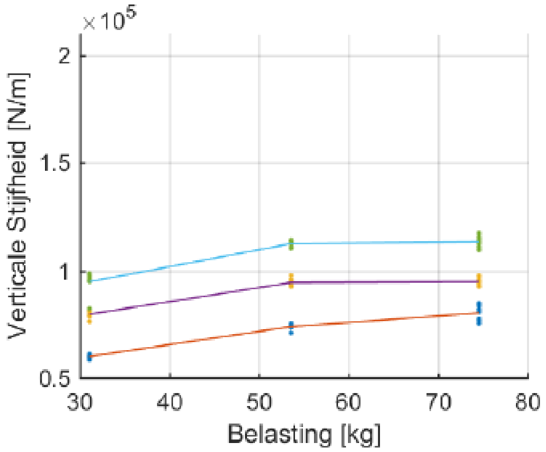

Figure 3.20: Vertical stiffness as a function of the normal load for the Cheng Shin Classic Zeppelin as presented by the Bachelor group. The different lines are for the different inflation pressures.

The varying k_{Pz} in Figure 3.19 looks fairly similar to the different inflation pressures of Figure 3.20. This creates the suspicion that k_{Pz} is closely related to the inflation pressure. Figure 3.2 amplifies this suspicion, since the contact patch length decreases when the k_{Pz} increases. The contact patch length from bicycle tyres also decreases when the inflation pressure is increased. Furthermore, from the measurements done by the Bachelor group Figures 3.21, 3.22 and 3.23 are created. These three graphs show great similarity to Figure 3.17.

From all the graphs shown in this section, it can be said that with reasonable suspicion k_{Pz} is more influenced by the inflation pressure and k_{Wz} is more affected by the carcass stiffness of the tyre. This is an interesting result, since the goal of this thesis is to estimate the tyre behaviour in terms of vertical stiffness, cornering stiffness and camber stiffness based on known parameters like the inflation pressure, tyre width, rim width and the kind of rubber. This means that with these model parameters, the inflation pressure can be (almost completely) decoupled from the other properties, which is useful in estimating tyre behaviour. It will be interesting to see if the model parameter values taken from the measurements will also have the behaviour as is shown here.

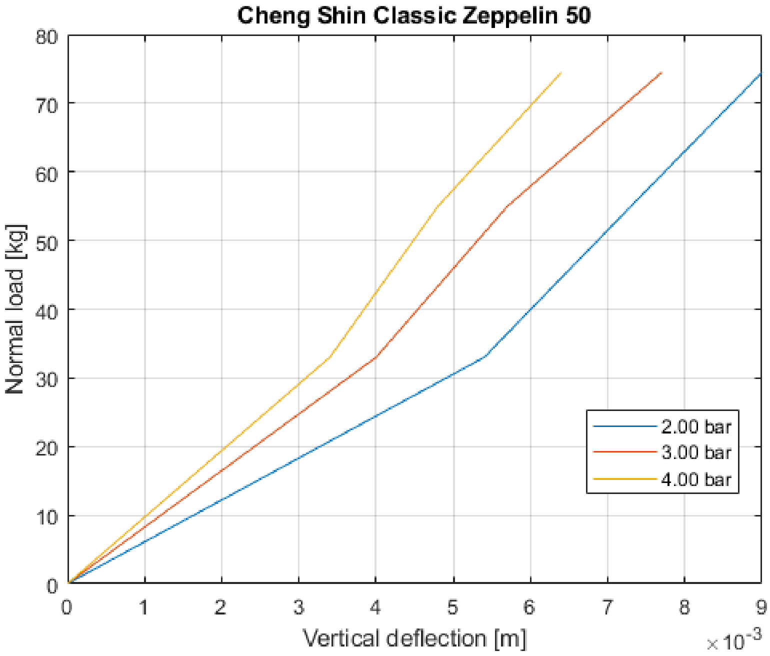

Figure 3.21: Influence of the inflation pressure on the normal load as a function of the vertical deflection for the Cheng Shin Classic Zeppelin.

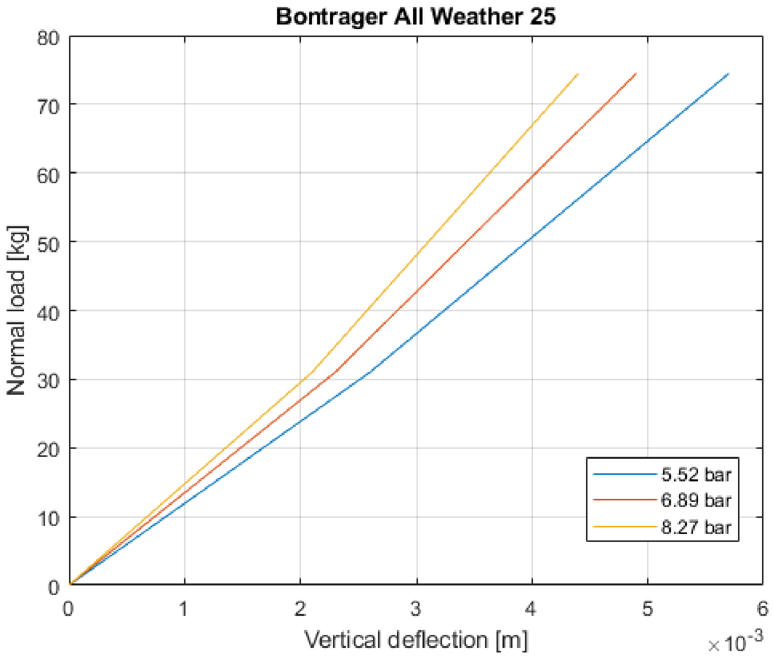

Figure 3.22: Influence of the inflation pressure on the normal load as a function of the vertical deflection for the Bontrager All Weather.

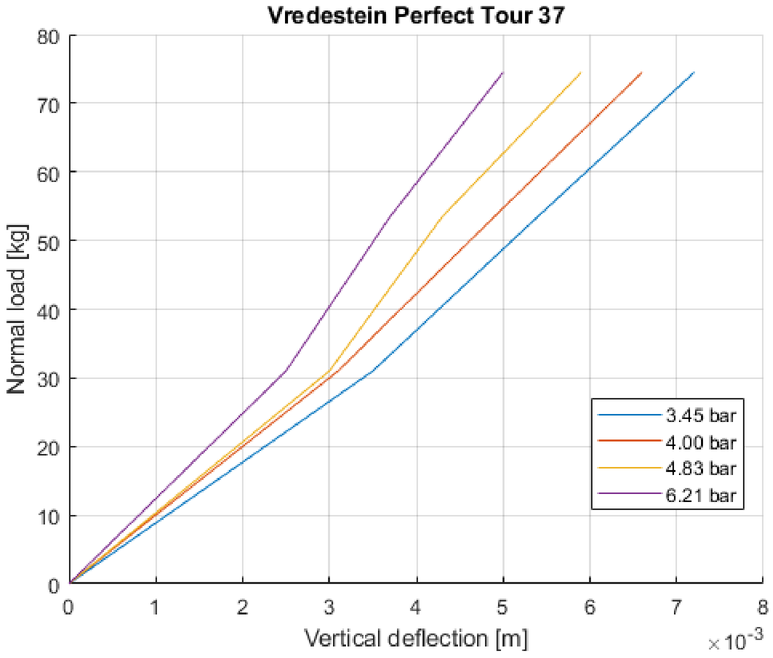

Figure 3.23: Influence of the inflation pressure on the normal load as a function of the vertical deflection for the Vredestein Perfect Tour.

3.3. Lateral force distribution

The lateral force distribution is determined by the lateral slip and the normal spin. First the situation for pure lateral slip will be discussed, then the situation for pure normal spin and the combined situation will be discussed.

The lateral pressure distribution is dependent on the vertical pressure distribution and a few new inputs. The inputs new inputs are: material parameters k_{Py}, k_{Wy} and k_{ty} and friction coefficients

μ_s and μ_k. The material parameters are the same as explained in previous section about the vertical pressure distribution, but now have the subscript y representing the stiffness in lateral direction. The fiction coefficients have subscript s and k standing for static and dynamic respectively. The static friction coefficient is used for the first part in the contact patch which is the adhesion part. The dynamic friction coefficient is for the second part of the contact patch which is sliding. This will become more clear with some figures later on.

The k_{ty} material parameter will be kept constant at $4 \cdot 10^6$ N m^{-2}. This is the same value as used in the paper by Meijaard. This is done with the same reasoning as used in the previous section. The effect of changing this parameter will be shown, but for the influence of other parameters this parameter will be kept at the same value as used by Meijaard.

The friction coefficients from Dressel's research are unknown, however, he used non-skid tape for the cornering and camber stiffness measurements. According to Dressel this means that the cornering and camber stiffness decrease less quickly. The effect that Dressel describes here will also be investigated.

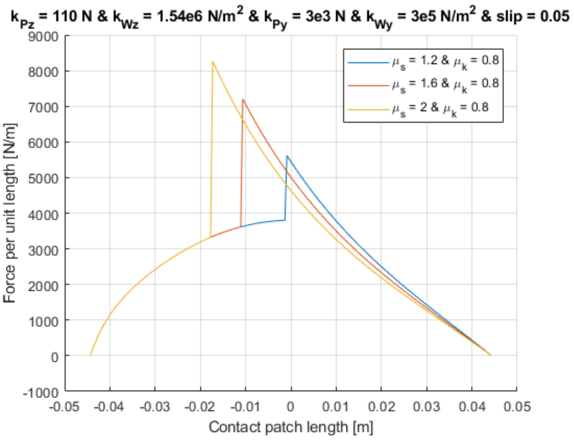

Figure 3.24: Influence of the static friction coefficient on the lateral pressure distribution.

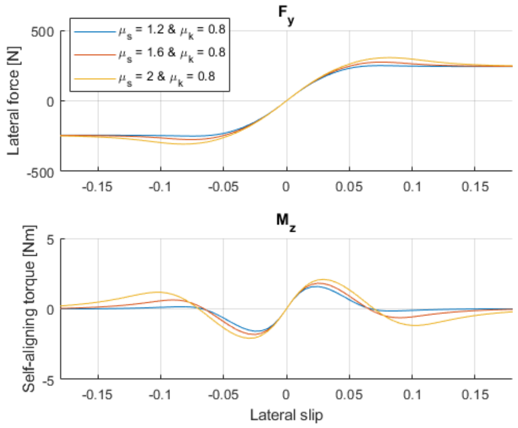

Figure 3.25: Influence of the static friction coefficient on the lateral force and self-aligning moment.

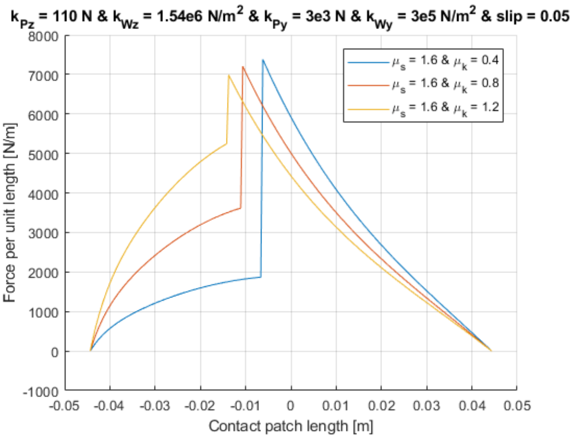

Figure 3.26: Influence of the dynamic friction coefficient on the lateral pressure distribution.

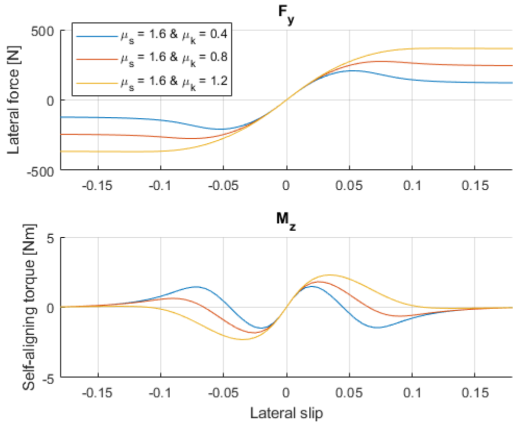

Figure 3.27: Influence of the dynamic friction coefficient on the lateral force and self-aligning moment.

First the influence of the friction coefficients will be investigated. In Figures 3.24 and 3.25 the influence of the static friction coefficient on the lateral pressure distribution, the lateral force-slip curve and self-aligning torque-slip curve is shown. In Figures 3.26 and 3.27 the influence of the dynamic friction coefficient is depicted. In the lateral pressure distribution graphs the difference between the static and dynamic friction coefficient can be seen. The static friction coefficient is used for the front part of the contact patch and the dynamic friction coefficient influences the rear part of the contact patch. From the lateral pressure distribution it can be derived that for a higher static friction coefficient the contact patch has a longer adhesion zone. The opposite is true for a lower dynamic friction coefficient, because the adhesion zone becomes shorter and also the sliding zone induces less force on the surface.

According to Dressel the cornering and camber stiffness decrease more quickly when the friction between the tyre and surface is less. Both the lateral force-slip curves support this statement. The effect of the dynamic friction coefficient is bigger, but it is true for both friction coefficients, since the slope of the lateral force curve starts to decrease at lower slip values for lower friction coefficients. The important thing to take away from it, is that the cornering and self-aligning torque stiffness are (almost) unaffected by the friction coefficients. The values of the cornering and camber stiffness are shown in Table 3.1. In here it can be seen that the cornering stiffness is increasing a bit when one of the friction coefficients is increased, this is because the peak lateral force is higher such that the slope remains constant over a larger range of slip. The camber stiffness is unaffected by the friction coefficients.

Note that these lateral pressure distributions are shown for a slip value of 0.05. This corresponds to an angle of 2.25 degrees between the velocity vector of the wheel and the wheel plane. For every slip angle a lateral pressure distribution can be created. To give an indication how the slip influences the pressure distribution Figure 3.28 is created. As can be seen in the figure, the adhesion region becomes shorter for higher slip values. It even disappeared for a slip value of 0.25. This means that the tyre is completely sliding and the biker will fall.

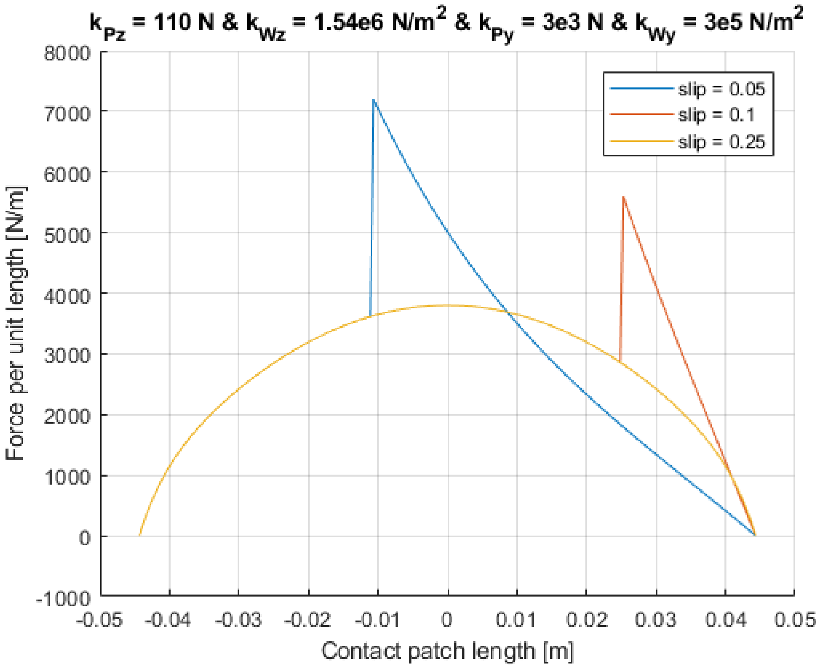

Figure 3.28: Influence of the slip on the lateral pressure distribution.

The pressure distribution graph can also be created for different normal spin values and a combination of normal spin and lateral slip. The normal spin is influenced by the camber angle of the wheel. The different pressure distributions are shown in Figure 3.29. This is to give an indication of how the pressure distribution is influenced by the normal spin and lateral slip.

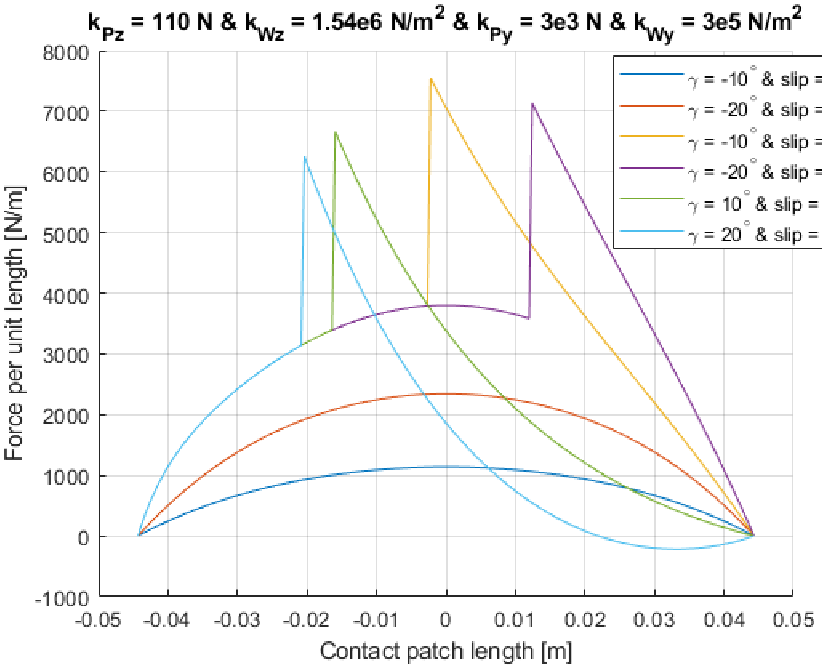

Figure 3.29: Influence of the normal spin and lateral slip on the pressure distribution.

The influence of k_{ty} on the lateral pressure distribution is depicted in Figure 3.30. Next to it in Figure 3.31 the influence on the lateral force and the self-aligning moment is shown. For a higher k_{ty} the adhesion part of the contact patch decreases, the cornering and self-aligning torque stiffness increase, but the maximum force/torque is reached at a lower slip angle. From Table 3.1 it can also be seen that the camber stiffness increases for higher values of k_{ty}.

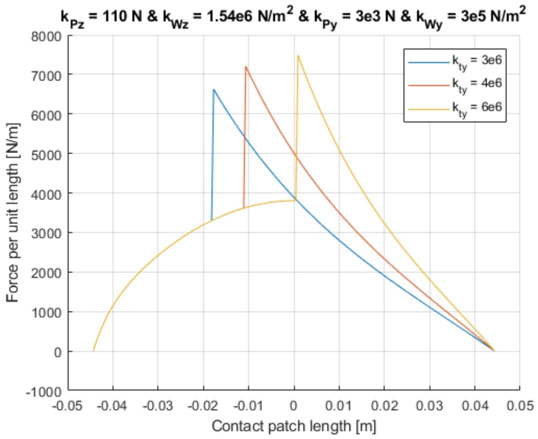

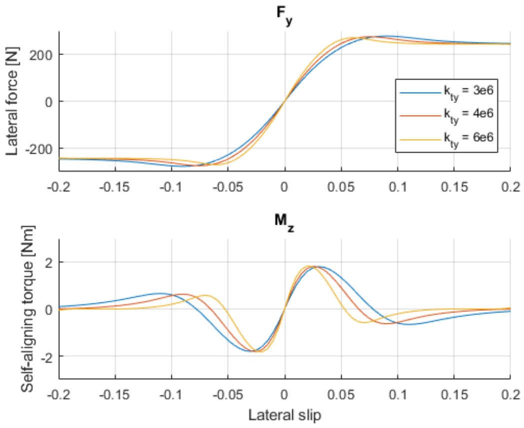

Figure 3.30: Influence of k_{ty} on the lateral pressure distribution.

Figure 3.31: Influence of k_{ty} on the lateral force and self-aligning moment.

The influence of k_{Py} on the lateral force, self-aligning torque and the pressure distribution is similar to the influence of k_{ty}. This can be seen in Figures 3.32 and 3.33. Also the camber stiffness increases for higher values of k_{Py}.

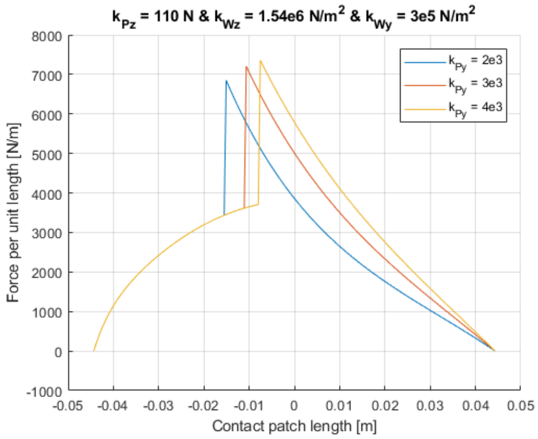

Figure 3.32: Influence of k_{Py} on the lateral pressure distribution.

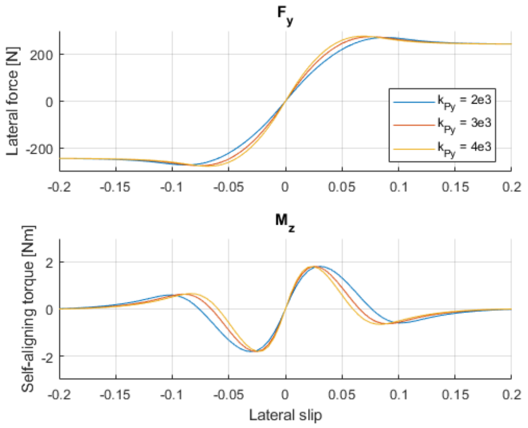

Figure 3.33: Influence of k_{Py} on the lateral force and self-aligning moment.

For k_{Wy} the same effect is obtained as for the other two lateral material parameters. Increasing the k_{Wy} decreases the adhesion part of the contact patch, increases the cornering, self-aligning torque and camber stiffness and moves the maximum force/torque peak to a lower slip value.

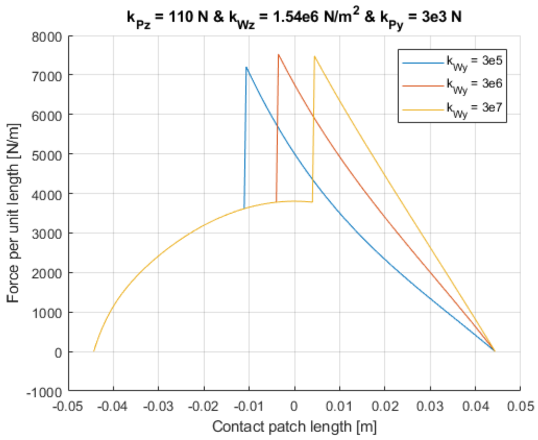

Figure 3.34: Influence of k_{Wy} on the lateral pressure distribution.

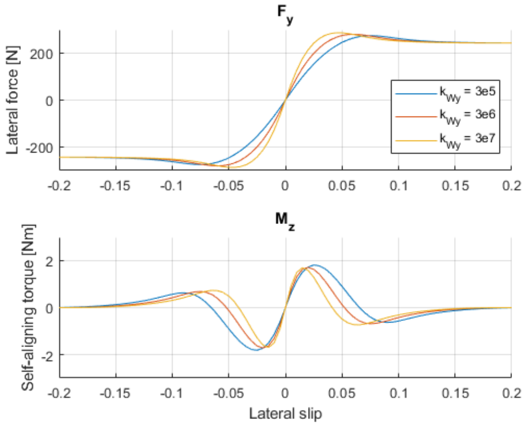

Figure 3.35: Influence of k_{Wy} on the lateral force and self-aligning moment.

Something that can be obtained from all the lateral pressure distribution graphs, is that the sliding part of the pressure distribution is always the same. It is independent of the changes in any of the stiffnesses. The only thing that changes is the length, but the curvature remains the same. This can be explained by looking at the equation for the lateral pressure distribution. As can be seen in Equation 3.3, the sliding part of the contact patch is defined as the vertical pressure distribution multiplied with the dynamic friction coefficient.

$$\begin{aligned}
p_{y,s}(x) &= \pm\mu_k p_z(x) \\
&= \pm\mu_k k_{tz}\left[-C_z\cosh(\kappa_{zi}x) + \left(1-\frac{\kappa_{zo}^2}{\kappa_{zi}^2}\right)\frac{1}{\kappa_{zi}^2 R_b}\right. \\
&\qquad \left. + \frac{\kappa_{zo}^2}{\kappa_{zi}^2}\left(\epsilon_n - \frac{x^2}{2R_b}\right)\right] \qquad (-a < x < \bar{x}), \\
p_{y,s}(x) &= k_{ty}(v_b - v_t) \\
&= k_{ty}C_{y1}(\cosh(\kappa_{yi}x) - \cosh(\kappa_{yi}a)) + k_{ty}C_{y2}(\sinh(\kappa_{yi}x) - \sinh(\kappa_{yi}a)) \\
&\qquad + k_{ty}\frac{\kappa_{yo}^2}{\kappa_{yi}^2}\left((a-x)s_y - (a^2-x^2)\frac{s_n}{2R_b}\right) \qquad (\bar{x} < x < a).
\end{aligned} \tag{3.3}$$

As the influence of the vertical material parameters on the pressure distribution already has been discussed in the previous section, it is assumed that the effects shown in previous section are also valid for the lateral pressure distribution. To be sure two extra graphs will be created where each vertical material parameter will have two different values. These graphs are depicted in Figures 3.36 and 3.37. The influence of k_{Wz} was the biggest on the vertical pressure distribution and the same is obtained here. An effect that wasn't thought of yet, is that the peak of the lateral force and self-aligning torque is a lot higher and also at a higher slip value for a higher value of k_{Wz}. A higher k_{Pz} means a less steep slope for the lateral force and self-aligning torque, but the peak is moving to a higher slip value.

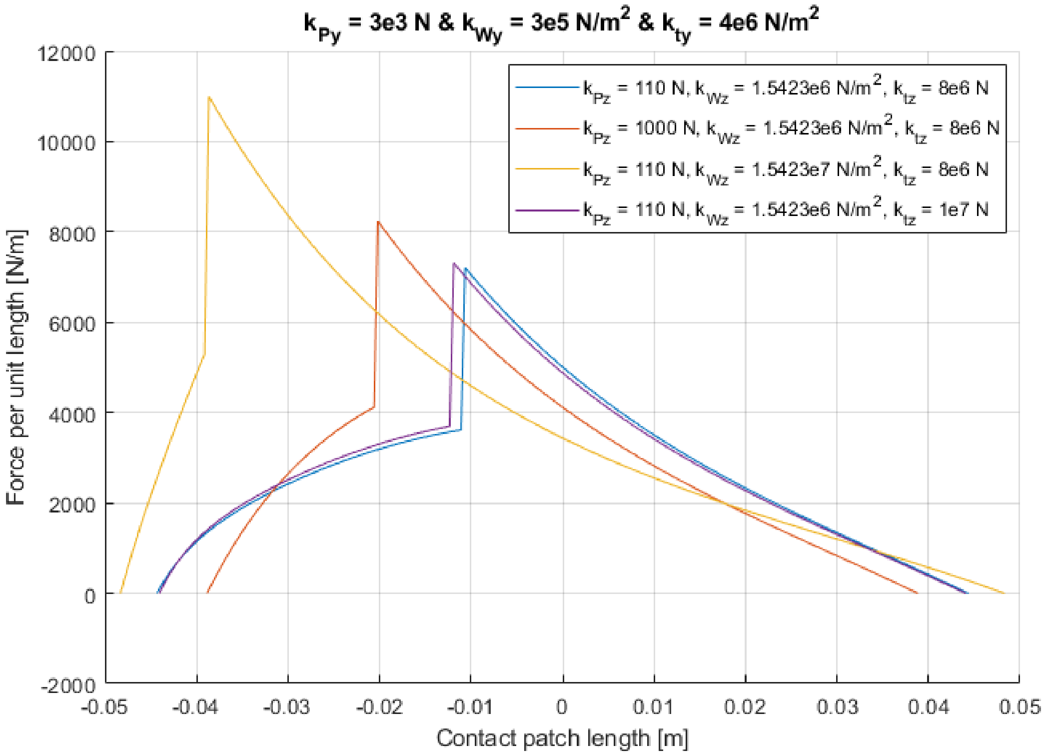

Figure 3.36: Influence of the vertical material parameters k_{Pz}, k_{Wz} and k_{tz} on the lateral pressure distribution.

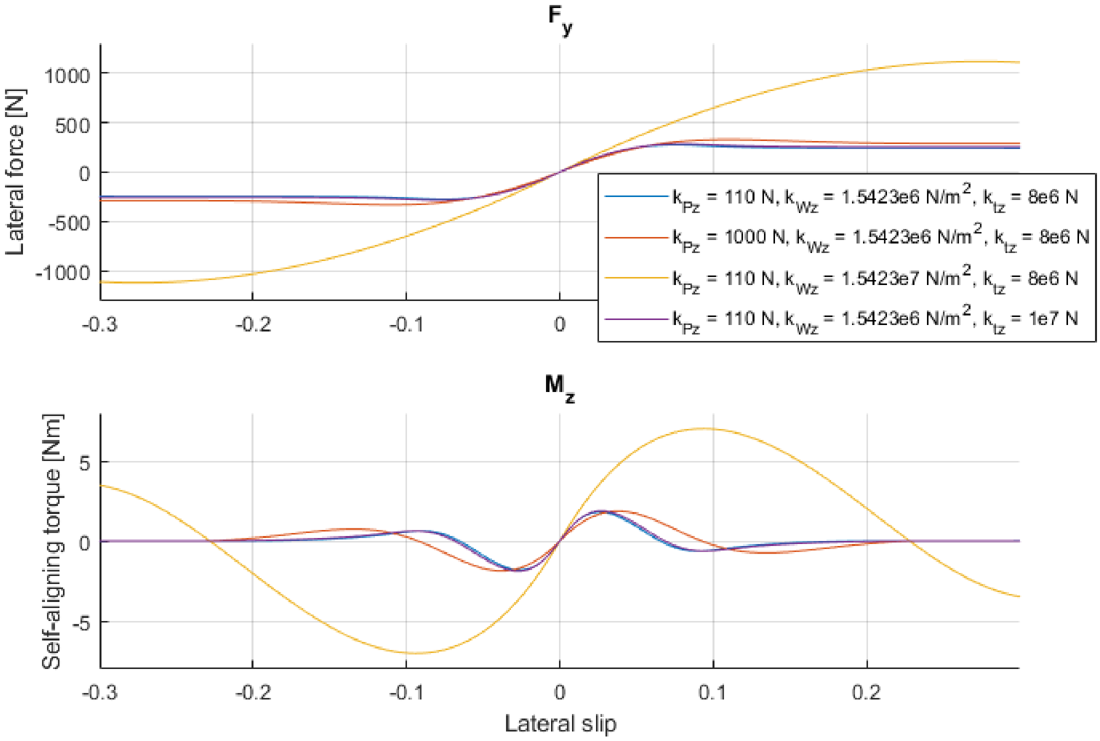

Figure 3.37: Influence of the vertical material parameters k_{Pz}, k_{Wz} and k_{tz} on the lateral force and self-aligning torque.

All the relevant outputs are shown in Table 3.2 and the changing inputs are in bold font.

Inputs								Outputs				
μ_s	μ_k	k_{Pz} (N)	k_{Wz} (Nm^{-2})	k_{tz} (Nm^{-2})	k_{Py} (N)	k_{Wy} (Nm^{-2})	k_{ty} (Nm^{-2})	F_z (kg)	$2a$ (mm)	$C_{F\alpha}$ $(N/°)$	$C_{M\alpha}$ $(Nm/°)$	C_{F_y} $N/°$
1.2	0.8	110	1.542e6	8e6	3e3	3e5	4e6	31	88.7	138.2	-1.73	6.96
1.6	0.8	110	1.542e6	8e6	3e3	3e5	4e6	31	88.7	141.4	-1.93	6.96
2	0.8	110	1.542e6	8e6	3e3	3e5	4e6	31	88.7	144.2	-2.10	6.96
1.6	**0.4**	110	1.542e6	8e6	3e3	3e5	4e6	31	88.7	137.5	-1.66	6.96
1.6	**0.8**	110	1.542e6	8e6	3e3	3e5	4e6	31	88.7	141.4	-1.93	6.96
1.6	**1.2**	110	1.542e6	8e6	3e3	3e5	4e6	31	88.7	144.8	-2.15	6.96
1.6	0.8	110	1.542e6	8e6	3e3	3e5	**3e6**	31	88.7	126	-1.78	5.83
1.6	0.8	110	1.542e6	8e6	3e3	3e5	**4e6**	31	88.7	141.4	-1.93	6.96
1.6	0.8	110	1.542e6	8e6	3e3	3e5	**6e6**	31	88.7	160.4	-2.04	8.65
1.6	0.8	110	1.542e6	8e6	**2e3**	3e5	4e6	31	88.7	119.2	-1.80	6.00
1.6	0.8	110	1.542e6	8e6	**3e3**	3e5	4e6	31	88.7	141.4	-1.93	6.96
1.6	0.8	110	1.542e6	8e6	**4e3**	3e5	4e6	31	88.7	157.6	-1.98	7.64
1.6	0.8	110	1.542e6	8e6	3e3	**3e5**	4e6	31	88.7	141.4	-1.93	6.96
1.6	0.8	110	1.542e6	8e6	3e3	**3e6**	4e6	31	88.7	189.2	-1.91	8.74
1.6	0.8	110	1.542e6	8e6	3e3	**3e7**	4e6	31	88.7	237.8	-1.77	11.02
1.6	0.8	110	1.542e6	8e6	3e3	3e5	4e6	31	88.7	141.4	-1.93	6.96
1.6	0.8	**1000**	1.542e6	8e6	3e3	3e5	4e6	36.9	77.7	125.4	-1.62	5.09
1.6	0.8	110	**1.542e7**	8e6	3e3	3e5	4e6	122.4	96.6	166.1	-3.19	8.44
1.6	0.8	110	1.542e6	**1e7**	3e3	3e5	4e6	32.1	88.1	141.5	-1.97	6.86

Table 3.2: Inputs and outputs used for creating the several figures. Note that the vertical deflection ϵ_n is 3.5 mm for all the cases in this table.

4

Methods

The equations derived in Chapter 2, will be used to find the model parameters of the tyre brush model and the enhanced string model. In this chapter it is explained how the data and equations are used to obtain the results. Obtaining the results for the tyre brush model is straightforward. However, obtaining the results for the enhanced string model is more complicated. A parameter optimisation is required. Also, in section 4.3 an explanation will be given on why there are more results for the tyre brush model than for the enhanced string model.

4.1. Data and derived equations

4.1.1. Tyre brush model

The derived equations for the tyre brush model are straightforward, as mentioned before. This means the parameter on the left side of the equality sign can be found easily by filling in the formula on the right side. All the measurement data is collected in a single Microsoft Excel file. A code written in Matlab makes it possible to obtain all the results in a fraction of a second. The formulas in the following section are used in the Matlab code.

Material parameter

There are three ways to calculate the material parameter from the tyre brush model. First the material parameter c_{py} is calculated from the measured cornering stiffness and contact patch length

$$c_{py} = \frac{C_{F_\alpha}}{2a^2} \tag{4.1}$$

Secondly, the measured self-aligning torque stiffness and contact patch length are used to calculate the material parameter

$$c_{py} = \frac{3C_{M_\alpha}}{2a^3} \tag{4.2}$$

It is chosen to not show the results from this method in the surface plots, since the self-aligning torque is the same as the cornering stiffness multiplied by the pneumatic trail ($\frac{1}{3}a$). The self-aligning torque stiffness measurements will be used for the pneumatic trail calculations shown in section 4.1.1.

Lastly, c_{py} is calculated from the measured camber stiffness, effective rolling radius and contact patch length

$$c_{py} = \frac{3C_{F_\varphi} r_e}{2a^3} \tag{4.3}$$

Pneumatic trail

There are two methods for calculating the pneumatic trail from the measurements. The first method is from the cornering stiffness and the self-aligning torque stiffness

$$t = -\frac{C_{M_\alpha}}{C_{F_\alpha}} \tag{4.4}$$

In Tire and Vehicle Dynamics [1] Pacejka shows that at vanishing slip angle, the expression for pneumatic trail reduces to:

$$t = t_0 = -\left(\frac{M_z}{F_y}\right)_{\alpha\to 0} = \frac{1}{3}a \tag{4.5}$$

So in the second method the pneumatic trail is calculated by using only the contact patch length measurements. The results from both methods are compared in 5.1.2.

4.1.2. Enhanced string model

The enhanced string model is more complicated than the tyre brush model. A result of this is that it is not possible to obtain the results in a similar fashion as the tyre brush model. In section 2.3 equations are derived for calculating the cornering, self-aligning torque and camber stiffness. Now for the tyre brush model, it was possible to rewrite these equations to use the measured stiffnesses as an input to find the model parameter. However, it is not possible to rewrite the enhanced string model equations, because it has multiple model parameters, which means that the equation is unsolvable. This is because the enhanced string model is an iterative model, which means a formula has to be solved multiple times before the solution converges to a stable value. This also means that it is not possible to put in the measured cornering, self-aligning torque or camber stiffness. To be able to find the model parameters an optimisation is needed. A parameter optimisation compares the model output with the measured data and adjusts the model parameters accordingly, such that after a certain amount of iterations the model output converges to the measured data value. The corresponding model parameters will be saved and these are shown in Chapter 5. More explanation on the parameter optimisation is done in section 4.2.

Contact patch length

The model elaborated by Meijaard [9] is a model that should be solved by an iterative process. In that process an initial value for the contact patch length is needed. A good approximation for an initial value is given by

$$a = (2R_b\epsilon_n)^{1/2} \tag{4.6}$$

This value will be calculated using the data from the Bachelor thesis [5] and put into the iterative process for calculating the vertical pressure distribution and the final contact patch length.

Material parameters

The enhanced string model contains more material parameters than the brush tyre model. The material parameters from the enhanced string model are: k_{Wi}, k_{ti} and k_{Pi}. The subscript i is the directional indicator and can stand for x, y or z. The measurements done by Dressel are all done for the lateral direction and the bachelor group did measurements for the vertical direction. So it is only possible to find the parameters for these two directions. The following relation between the vertical stiffness and the material parameters was found:

$$\left(\frac{\partial F_z}{\partial \epsilon_n}\right)_{\epsilon_n=0} = 2k_{tz}\left(-\frac{1}{\frac{\kappa_{zo}}{\tanh(\kappa_{zi}a)}+\kappa_{zi}}\frac{\kappa_{zo}}{\kappa_{zi}}\left(\frac{\kappa_{zo}^2}{\kappa_{zi}^2}-1\right)+a\frac{\kappa_{zo}^2}{\kappa_{zi}^2}\right). \tag{4.7}$$

In this equation $\kappa_{zo} = (k_{Wz}/k_{Pz})^{1/2}$ and $\kappa_{zi} = [(k_{Wz}+k_{tz})/k_{Pz}]^{1/2}$. It is visible that it is not possible to solve Equation 4.7, since there are three unknown parameters and only two known parameters. For this a parameter optimisation will be made, but this will be discussed in section 4.2. Also as explained in section 3.1, k_{tz} will be kept constant at $8\cdot 10^6$ N m^{-2}.

The relation for the cornering stiffness that was obtained in Chapter 2 is:

$$\begin{aligned}\left(\frac{\partial F_{y,s}}{\partial s_y}\right)_{s_y=0} = \int_{\bar{x}}^{a}\Bigg[&k_{ty}\frac{\partial C_{y1}}{\partial s_y}(\cosh(\kappa_{yi}x)-\cosh(\kappa_{yi}a))\\ &+k_{ty}\frac{\partial C_{y2}}{\partial s_y}(\sinh(\kappa_{yi}x)-\sinh(\kappa_{yi}a))+k_{ty}\frac{\kappa_{yo}^2}{\kappa_{yi}^2}(a-x)\Bigg]dx\end{aligned} \tag{4.8}$$

in which $\kappa_{yo} = (k_{Wy}/k_{Py})^{1/2}$ and $\kappa_{yi} = [(k_{Wy} + k_{ty})/k_{Py}]^{1/2}$. The self-aligning torque stiffness is defined by the following equation:

$$\begin{aligned}\left(\frac{\partial M_{z,s}}{\partial s_y}\right)_{s_y=0} = \int_{\bar{x}}^{a} x\Bigg[&k_{ty}\frac{\partial C_{y1}}{\partial s_y}(\cosh(\kappa_{yi}x) - \cosh(\kappa_{yi}a)) \\ &+ k_{ty}\frac{\partial C_{y2}}{\partial s_y}(\sinh(\kappa_{yi}x) - \sinh(\kappa_{yi}a)) + k_{ty}\frac{\kappa_{yo}^2}{\kappa_{yi}^2}(a - x)\Bigg]dx\end{aligned} \tag{4.9}$$

Both these equations are obtained with the Matlab symbolic toolbox, because the expressions are really long and it is easy to make mistakes in a manual derivation. Evidently, these two equations for the cornering and self-aligning torque stiffness also cannot be solved, since there are three unknown parameters. The values of the parameters will be found using a parameter optimisation. Equally to the vertical version of this parameter, k_{Py} will be kept constant at $4 \cdot 10^6$ N m^{-2} as explained in section 3.3.

The last method to find the material parameters is with the equation for the camber stiffness. The camber stiffness is given by:

$$\begin{aligned}\left(\frac{\partial F_{y,s}}{\partial s_n}\right)_{s_n=0} = \int_{\bar{x}}^{a} \Bigg[&k_{ty}\frac{\partial C_{y1}}{\partial s_n}(\cosh(\kappa_{yi}x) - \cosh(\kappa_{yi}a)) \\ &+ k_{ty}\frac{\partial C_{y2}}{\partial s_n}(\sinh(\kappa_{yi}x) - \sinh(\kappa_{yi}a)) - k_{ty}\frac{\kappa_{yo}^2}{\kappa_{yi}^2}\left(\frac{(a^2 - x^2)}{2R_b}\right)\Bigg]dx\end{aligned} \tag{4.10}$$

Just as with the earlier equations, this equation is also obtained with the Matlab symbolic toolbox.

4.2. Parameter optimisation

A parameter optimisation has to be done in order to find the material parameters from the enhanced string model. In Matlab four different optimisation methods are used and compared to each other to make sure the right parameter values are found and not just a local minimum. Also different initial values will be used for the same reason. The following Matlab functions are used: *fminsearch*, *fminunc*, *fmincon* and *lsqnonlin*. For a parameter optimisation with Matlab a parameter vector p, output data y, input data u and a model equation $\hat{y}$ are needed. First the material parameters for the vertical direction will be found. It is important that the right values are found for the vertical parameters, because as shown in Table 3.2 the vertical parameters influence the contact patch and this in its turn has an effect on the cornering and self-aligning torque stiffness. Once this is done, the parameters for the lateral direction will be found.

4.2.1. Optimisation algorithms

fminsearch

The *fminsearch* command in Matlab uses the Nelder-Mead simplex algorithm. This is a direct search method for multidimensional unconstrained minimisation [21]. The Nelder-Mead method attempts to minimise a scalar-valued nonlinear function of n real variables using only function values, without any derivative information. The Nelder-Mead method maintains a non-degenerate simplex, a geometric figure in n dimensions of nonzero volume that is the convex hull of $n + 1$ vertices, at each step. Each iteration of a simplex-based direct search method begins with a simplex specified by its $n + 1$ vertices and the associated function values. One or more test points are computed, along with their function values, and the iteration terminates with bounded level sets.

The Nelder-Mead algorithm was proposed as a method to minimising a real-values function $f(\mathbf{x})$ for $\mathbf{x} \in \Re^n$. Four scalar parameters must be specified do define a complete Nelder-Mead method: coefficients of *reflection* (ρ), *expansion* (χ), *contraction* (γ) and *shrinkage* (σ). According to the original Nelder-Mead paper [22], these parameters should satisfy

$$\rho > 0,\ \chi > 1,\ \chi > \rho,\ 0 < \gamma < 1 \text{ and } 0 < \sigma < 1. \tag{4.11}$$

At the beginning of the kth iteration, $k \geq 0$, a non-degenerate simplex Δ_k is given, along with its $n + 1$ vertices, each of which is a point in $\Re^n$. It is always assumed that iteration k begins by ordering and labelling these vertices as $\mathbf{x}_1^{(k)}, \ldots, \mathbf{x}_{n+1}^{(k)}$, such that

$$f_1^{(k)} \leq f_2^{(k)} \leq \ldots \leq f_{n+1}^{(k)}, \tag{4.12}$$

where $f_i^{(k)}$ denotes $f(\mathbf{x}_i^{(k)})$. The kth iteration generates a set of $n + 1$ vertices that define a different simplex for the next iteration, so that $\Delta_{k+1} \neq \Delta_k$. Because the goal is to minimise f, $\mathbf{x}_1^{(k)}$ is the *best* point or vertex, $\mathbf{x}_{n+1}^{(k)}$ is the *worst* point, and $\mathbf{x}_n^{(k)}$ is the *next-worst* point. Similarly, $f_{n+1}^{(k)}$ is the worst function value, and so on.

A single generic iteration is specified. The result of each iteration is either a single new vertex - the *accepted point* - which replaces $\mathbf{x}_{n+1}$ in the set of vertices for the next iteration, or if a shrink is performed, a set of n new points that, together with $\mathbf{x}_1$ form the simplex at the next iteration. One iteration of the Nelder-Mead can be read in [21].

fminunc

The *fminunc* function in Matlab uses the BFGS Quasi-Newton algorithm with a cubic line search procedure. The search for a minimum of maximum of a scalar-valued function is the search for the zeroes of the gradient of that function. In Newton's method, a second-order approximation is used to find the minimum of a function $f(x)$ [23]. The Taylor series of $f(x)$ around an iterate is

$$f(x_k + \Delta x) \approx F(x_k) + \nabla f(x_k)^T \Delta x + \frac{1}{2} \Delta x^T B \Delta x, \tag{4.13}$$

where (∇f) is the gradient, and B an approximation to the Hessian matrix. The gradient of this approximation with respect to Δx is

$$\nabla f(x_k + \Delta x) \approx \nabla f(x_k) + B\Delta x, \tag{4.14}$$

and setting this gradient to zero provides the Newton step:

$$\Delta x = -B^{-1} \nabla f(x_k). \tag{4.15}$$

Hessian approximation B is chosen to satisfy

$$\nabla f(x_k + \Delta x) = \nabla f(x_k) + B\Delta x, \tag{4.16}$$

which is the Taylor series of the gradient itself. The unknown x_k is updated by applying the Newton's step calculated using the current approximate Hessian matrix B_k:

$$\Delta x_k = -\alpha B_k^{-1} \nabla f(x_k) \tag{4.17}$$

$$x_{k+1} = x_k + \Delta x_k \tag{4.18}$$

The gradient computed at the new point $\nabla f(x_{k+1})$ and

$$y_k = \nabla f(x_{k+1}) - \nabla f(x_k) \tag{4.19}$$

is used to update the approximate Hessian B_{k+1}, or directly its inverse $H_{k+1} = B_{k+1}^{-1}$. The update formula that the BFGS Quasi-Newton algorithm uses for B_{k+1} is

$$B_k + \frac{y_k y_k^T}{y_k^T \Delta x_k} - \frac{B_k \Delta x_k (B_k \Delta x_k)^T}{\Delta x_k^T B_k \Delta x_k}. \tag{4.20}$$

fmincon

The interior-point approach to constrained minimisation is to solve a sequence of approximate minimisation problems. The inequality constrained problems are in the form

$$\begin{gathered} \min_x f(x) \\ \text{subject to } g(x) \leq 0, \end{gathered} \tag{4.21}$$

where $f\colon \mathfrak{R}^n \to \mathfrak{R}$ and $g : \mathfrak{R}^n \to \mathfrak{R}^m$ are smooth functions. Following the strategy of interior point methods, the following barrier problem in the variables x and s is

$$\begin{gathered}\min_{x,s} f(x) - \mu \sum_{i=1}^{m} \ln s^{(i)} \\ \text{subject to } g(x) + s = 0,\end{gathered} \tag{4.22}$$

where $\mu > 0$ and where the vector of slack variables $s = (s^{(1)}, ..., s^{(m)})^\top$ is implicitly assumed to be positive. More on this optimisation algorithm can be read in [24].

lsqnonlin

The *lsqnonlin* command in Matlab solves nonlinear least-squares curve fitting problems of the form

$$\min_x ||f(x)||_2^2 = \min_x \left(f_1(x)^2 + f_2(x)^2 + \ldots + f_n(x)^2\right) \tag{4.23}$$

with optional lower and upper bounds on the components of x. Rather than computing the sum of squares, this function requires the user-defined function to compute the vector-valued function

$$f(x) = \begin{bmatrix} f_1(x) \\ f_2(x) \\ \vdots \\ f_n(x) \end{bmatrix}. \tag{4.24}$$

4.2.2. Vertical direction

The vertical stiffnesses are measured by the guys from the bachelor thesis [5] and the contact lengths are measured by Dressel [4]. In order to find the values of the parameters from Equation 4.7, in which $\kappa_{zo} = (k_{Wz}/k_{Pz})^{1/2}$ and $\kappa_{zi} = [(k_{Wz} + k_{tz})/k_{Pz}]^{1/2}$, k_{tz} will be kept constant. The influence of this parameter on the vertical stiffness is shown in section 3.1 and it is elaborated why this parameter will be kept constant at $8 \cdot 10^6$ N m^{-2}. The parameter vector p consists of (k_{Pz} and k_{Wz}), Equation 4.7 will be the model equation $\hat{y}$, output data y consists of the vertical stiffnesses measured by the Bachelor group and the contact patch length measured by Dressel is the input data u.

Wrong results from the optimisation

The first results from the optimisation are not satisfying, because the results from all the different optimisation methods are not corresponding to each other. Moreover, changing the initial values for the parameters have a huge effect on the outcome of the optimisation. However, entering the values found by the optimisation into Equation 4.7 gives the right vertical stiffnesses, so the optimisation is doing its work correctly. Now, when these values are entered into the enhanced string model, the wrong normal load and contact patch length are found. This indicates that the obtained values are indeed wrong.

Considering the fact that the optimisation is doing what it should do, it can only mean that the model equation $\hat{y}$ is wrong. This model equation is derived by hand and checked by using the symbolic toolbox of Matlab. In both situations this equation is found, so it is expected that the condition of $\epsilon_n = 0$ is not applicable for the stiffnesses measured by the Bachelor group. To support this expectation a graph is created where the normal load as a function of the vertical deflection is shown. This graph is shown in Figure 4.1. This graph is created with constant values for the material parameters. As can be seen, the slope of the line is increasing for higher deflections, which means that the vertical stiffness is increasing. The slope of the line around 31, 53.5 and 74.5 kg of normal load is definitely different than the slope around 0.1 kg of normal load. From this it can be concluded that Equation 4.7 cannot be used as a model equation for the parameter optimisation.

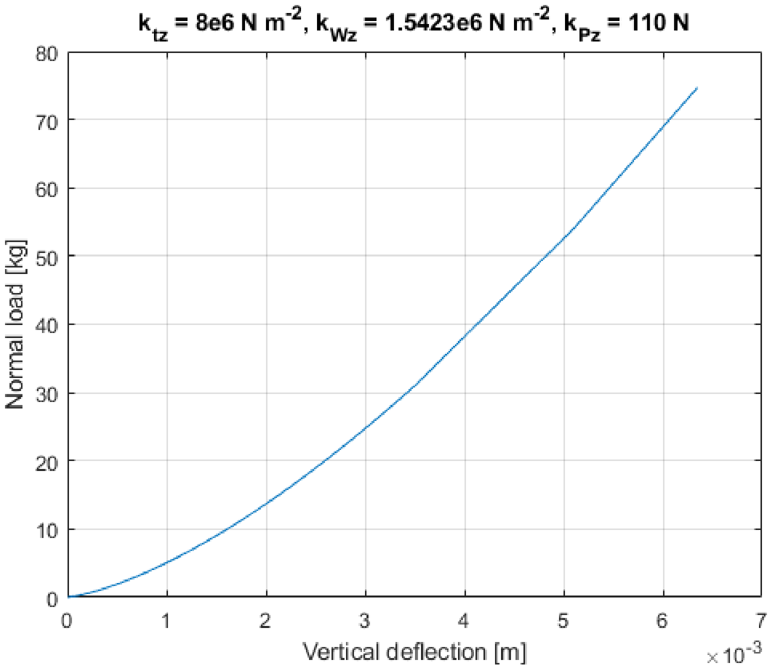

Figure 4.1: Influence of the vertical deflection on the normal load.

Solution for the parameter optimisation

Since the previously chosen model equation cannot be used for the parameter optimisation, a solution has to be found. An idea is to use the whole iterative model to find the parameters. As explained before in section 3.1, the enhanced string model uses the vertical deflection ϵ_n and the material parameters k_{Pz}, k_{Wz} and k_{tz} as an input to calculate the contact patch length and the normal load. Of course the same parameter vector p with k_{Pz} and k_{Wz} will be used. k_{tz} will still be kept constant, but the input for the parameter optimisation will be ϵ_n. From the measured vertical stiffnesses of the Bachelor group, the vertical deflection ϵ_n for each normal load on the tyre can be calculated. As mentioned before the model outputs $\hat{y}$ will be the normal load and the contact patch length. So this vector now consists of two things. The output data y also has to consists of these two things: the normal load and the contact patch length.

A note has to be made for the model output and data vector. The error is calculated by subtracting the the model output from the data, $e = y - \hat{y}$. The contact length is in metres (around 0.005 m) and the normal load in Newton (around 500 N). Because of this big difference in value, the absolute error is probably a lot bigger for the normal load than the contact patch. Therefor the contact patch error will be multiplied by 100000, such that both errors are equally important for the optimisation to consider in finding the optimal parameters.

The results from this optimisation are satisfying. Three of the four methods give the same results and these are independent of the initial values. The results will be discussed in section 5.2.

4.2.3. Lateral direction

The cornering, self-aligning torque and camber stiffness measured by Dressel will be used to find the material parameters k_{Wy} and k_{Py}. Before that will be done, an assumption will be made. As might be recalled, the k_{Pz} and k_{Py} are the shear stiffness of the foundation, so the shear stiffness of a string under tension. It is plausible to assume that the shear stiffness in vertical direction is equal to the shear stiffness in lateral direction. So the k_{Pz} values found in the parameter optimisation for the vertical direction, will be used for the k_{Py} parameter. The only parameter that needs to be found now is the k_{Wy}. The parameter vector p now will consist only of k_{Wy}. Equations 4.8, 4.9 and 4.10 will be the model equations $\hat{y}$ and the output data y consists of the cornering, self-aligning torque and camber stiffness measured by Dressel. The results from this optimisation are shown in section 5.2. One might wonder, why not use all three model equations in the same optimisation, like was done for the vertical parameter optimisation instead of running three different optimisations. Well, since there is only one parameter to change (k_{Wy}), it is not possible to find combinations of parameters such that all three model equations are met.

4.3. Limitations in acquiring results

Dressel tested a large variety of tyres which are displayed in Table 4.1. The size in this table indicates the width of the inflated tyres in millimetres. Unfortunately, the data sets for some of the tyres are incomplete. This is due to various reasons.

The first reason is that Dressel skipped some of the inflation pressures, the reason for this is unknown. Most likely these pressures were skipped because they were lower than the recommended pressures.

Secondly, Dressel did his measurements with three different devices. The first measuring device was a wooden frame which holds the wheel under a certain slip and camber angle and was pulled over a flat surface. The final iteration is shown in Figure 4.2. The second device was a welded steel frame to hold the wheel stationary in a desired orientation on top of a small track of flat-top chain. Test device 2 is shown in Figure 4.4. The last test device, is the device on which he did most of the measurements. This is the tyre testing drum at Delft University of Technology. This device is shown in Figure 4.3. Since the data is measured by 3 different devices, some data is incomplete. For instance, the contact patch measurements are only done at Delft, because a comparison is made between a contact patch on the drum and a flat plate. This means that there is no contact patch data available for the tyres measured at the University of Wisconsin-Milwaukee.

Another reason for incomplete data is the fact that the vertical stiffness data is acquired by a group of four students for their Bachelor Thesis and most of the tyres that they tested do not have contact patch data. Vice versa, most tyres that do have contact patch data are not measured by the Bachelor group. In the next sections the limitations for each model will be explained.

Table 4.1: The tyres that Andrew Dressel tested.

Brand	**Model**	**Size**	**Tread**	**Bead**
Bontrager	All Weather	23	Semi-smooth	Foldable
Bontrager	All Weather	25	Semi-smooth	Foldable
Bontrager	All Weather	28	Semi-smooth	Foldable
Cheng Shin	Classic Zeppelin	50	-	Wire
Continental	Top Contact Winter	37	-	Wire
Maxxis	Radial Prototype	22	Smooth	Foldable
Michelin	Dynamic	23	Semi-smooth	Wire
Schwalbe	Big Apple	55	-	Wire
Schwalbe	Kojak	35	-	Foldable
Schwalbe	Marathon Plus	37	-	Wire
Vittoria	Randonneur Hyper	37	-	Foldable
Vredestein	Perfect Tour	37	Semi-smooth	Wire
Vredestein	Fortezza DuoComp	23	Smooth	Foldable
Vredestein	Fortezza TriComp	23	Smooth	Foldable

4.3.1. Tyre brush model

To be able to calculate the material parameter from the tyre brush model only the contact patch data and one of the stiffnesses (cornering, self-aligning torque or camber) is needed. So missing the vertical stiffness measurements is not a problem.

There is no contact patch data provided for the Bontrager All Weather 23, such that material parameter c_{py} cannot be calculated. For the other two Bontrager tyres complete measurements are missing, this means no data about the cornering stiffness, self-aligning torque stiffness, contact patch size etc. This means that it is not possible to create a good surface plot with the available data. Furthermore, there is no contact patch data provided for the Maxxis, Michelin, Vredestein Fortezza DuoComp and TriComp tyres. The data for the rest of the tyres is complete, so these will be shown in the results section.

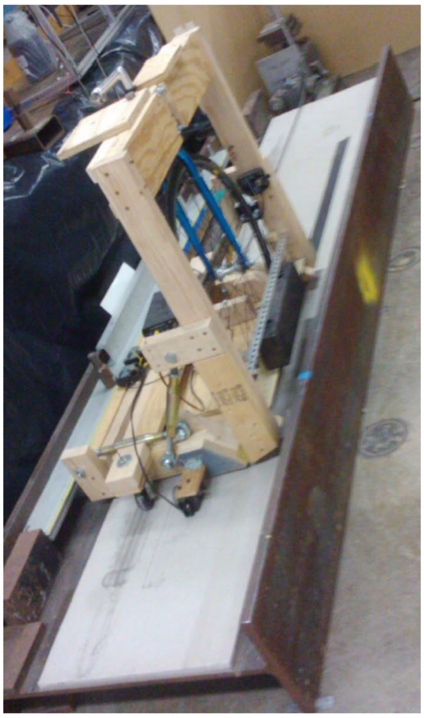

Figure 4.2: Test device 1

Figure 4.3: Test device 3

Figure 4.4: Test device 2

4.3.2. Enhanced string model

For the enhanced string model the vertical stiffness is important. The vertical deformation of the tyre is an input of the model, so the vertical stiffness is needed to calculate the vertical deformation under the different normal loads.

The remaining tyres that can be fully analysed with the enhanced string model are the Cheng Shin Classic Zeppelin and the Vredestein Perfect Tour. The Bontrager All Weather 25 and 28 can be partially used.

5

Results

5.1. Results of the tyre brush model

In this section the results of the measurement data linked to the tyre brush model will be discussed. First the results for material parameter c_{py} are shown. Then the pneumatic trail comes to discussion and as last a comparison between the self-aligning torque stiffness and the spin stiffness.

5.1.1. Material parameter

The calculated c_{py} values from the cornering stiffness and camber stiffness for the Cheng Shin Classic Zeppelin tyres are shown in Figure 5.1 and Table 5.1. The material parameter c_{py} increases with increasing inflation pressure. The influence of the normal load on the material parameter is not unambiguously for this specific tyre, at least, that is when both the results of cornering and camber stiffness are considered. When looking at the results of the cornering stiffness, c_{py} is decreasing as the normal load increases. For the camber stiffness this relation is opposite. The results for the other tested tyres are depicted in Appendix A.1. In these graphs and tables the general relation between the material parameter and the inflation pressure is that the material parameter increases with increasing inflation pressure. This is true for both, the cornering and camber stiffness data. Not a lot can be concluded about the relation between the material parameter and the normal load. For some of the tyres the c_{py} increases as the normal load increases and for others the c_{py} decreases as the normal load increases. There is even differences between the cornering and camber stiffness data. An interesting observation though, is that for every single tyre the shape of the surface plots from the cornering stiffness C_{F_α} and camber stiffness C_{F_γ} are relatively similar. This is noteworthy, since the cornering stiffness measurement is independent from the camber stiffness measurement.

Table 5.1: Cheng Shin Classic Zeppelin

Normal load [kg]	Pressure [bar]	$c_{py} \times 10^4$ (cornering)	$c_{py} \times 10^4$ (camber)
33	2.0	1.82	1.70
33	3.0	1.94	1.31
33	4.0	2.88	2.03
55	2.0	1.37	1.64
55	3.0	1.87	1.99
55	4.0	2.57	2.65
74	2.0	0.96	1.27
74	3.0	1.64	2.09
74	4.0	2.28	2.84

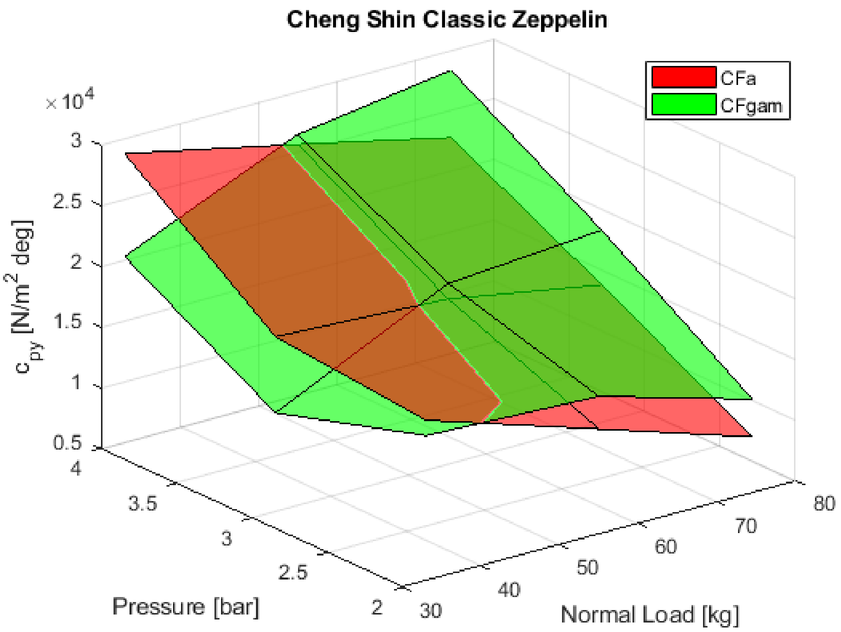

Figure 5.1: Material parameter c_{py} for Cheng Shin Classic Zeppelin.

In Figure 5.2 the material parameter for every measured tyre (with a complete data set) is shown. The pink vertical lines indicate a change in tyre and one should keep in mind that the slope of the three lines is not important here. They just give a better indication of where the points are. From this graph it is visible that for most of the tyres the material parameters calculated in three different ways are relatively close to each other. With a bit better agreement between the blue and yellow points, rather than the red points. This might indicate that the cornering stiffness measurement and the spin stiffness measurement are more reliable. An interesting thing is that the material parameter calculated from the spin stiffness for both the Bontrager tyres and the Maxxis tyre, is really off from the rest of the calculated material parameter. Since all three lines are calculated using the same contact patch length, the difference lies in the cornering, self-aligning torque and spin stiffness. Looking back at Table 4.1, it can be seen that the tyres that are off with the material parameter have a smaller size, so this might be a reason for the relatively different material parameter.

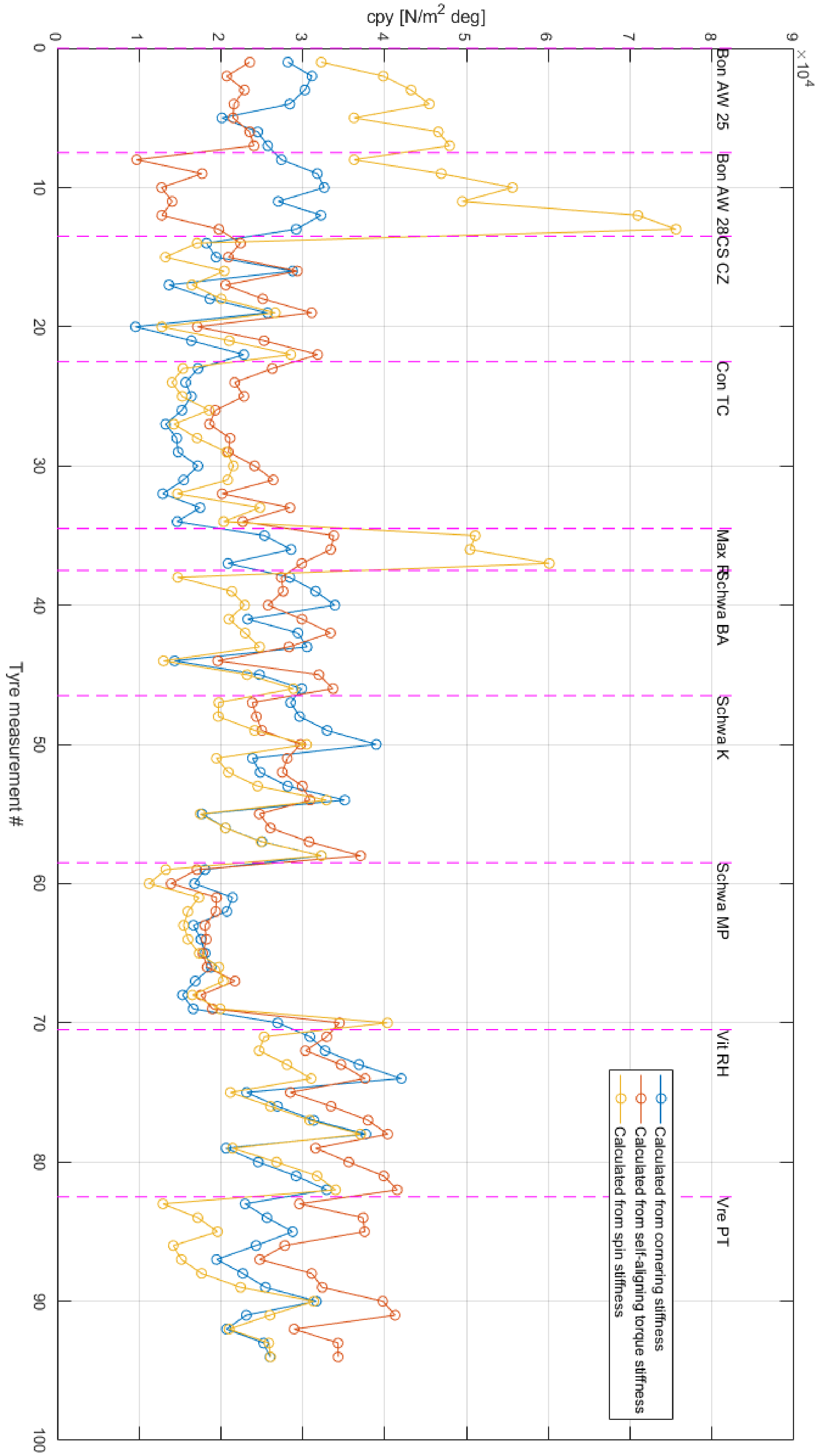

Figure 5.2: Material parameter from all the tested tyres obtained in three different ways.

5.1.2. Pneumatic trail

In Figure 5.3 the pneumatic trail t is depicted as a function of the normal load and the inflation pressure. Both the pneumatic trail calculated by the self-aligning torque stiffness over the cornering stiffness as the one calculated by one third of half the contact length are shown. For this specific tyre the values are close together for a high inflation pressure and low normal load and start to become more apart as the normal load increases and/or the inflation pressure decreases. It is expected that the pneumatic trail is small for high inflation pressure and low normal load, since the contact length is also smaller. The contact patch length increases for increasing normal load and/or decreasing inflation pressure. The results for the other tested tyres regarding the pneumatic trail are shown in Appendix A.2. All these graphs show the same relations as the graph from the Cheng Shin Classic Zeppelin, which is to be expected. However, the relation between pneumatic trail and inflation pressure is slightly hard to discover in the graphs in general. This can be explained by the fact that the step size of the inflation pressure does not change the contact length as much as the step size of the normal load does. Something else that is noticeable, is that in general the pneumatic trail calculated by the self-aligning torque stiffness over the cornering stiffness is bigger than one third of half the contact patch length.

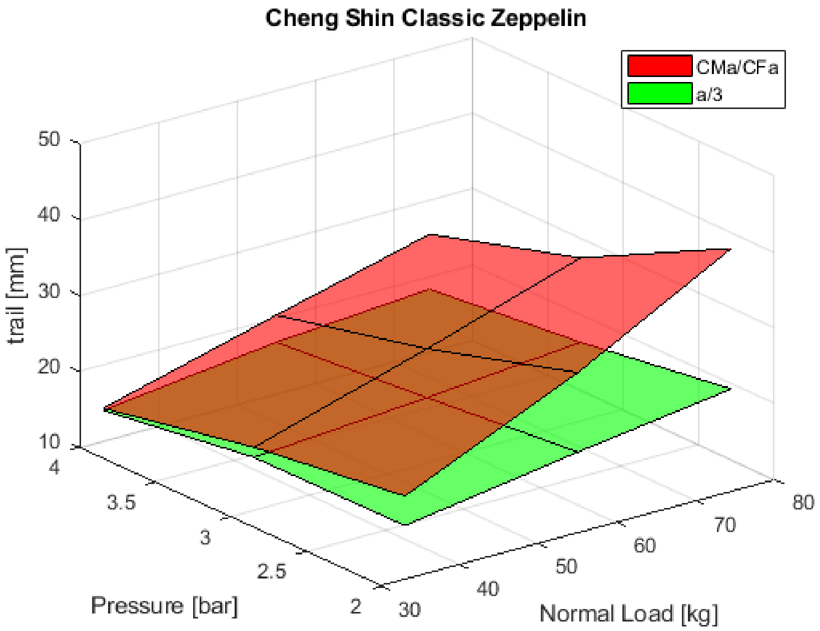

Figure 5.3: Trail t for Cheng Shin Classic Zeppelin.

In Figure 5.4 the pneumatic trail is depicted for every measured tyre (with a complete data set). It is remarkable that for most tyres the calculated pneumatic trail is higher than the rule of thumb. Except for the Bontrager tyres it is the other way around. To give more insight in this graph, the order of measurements is shown in Table 5.2. Depending on the tyre, inflation pressure values and normal loads can be different. This table shows that the first measurements are with the lowest normal load and increasing pressure followed by the same sequence for a higher normal load. From the graph it seems that the calculated pneumatic trail approaches the rule of thumb value for the highest pressure from the sequence. This is also visible in all the individual tyre surface plots, because the line corresponding to the highest inflation pressure is closest to the rule of thumb line.

Measurement #	Load [kg]	Inflation pressure [bar]
1	33	4.00
2	33	4.83
3	33	6.21
4	55	4.00
5	55	4.83
6	55	6.21
7	74.5	4.00
8	74.5	4.83
9	74.5	6.21

Table 5.2: Order of the tyre measurements

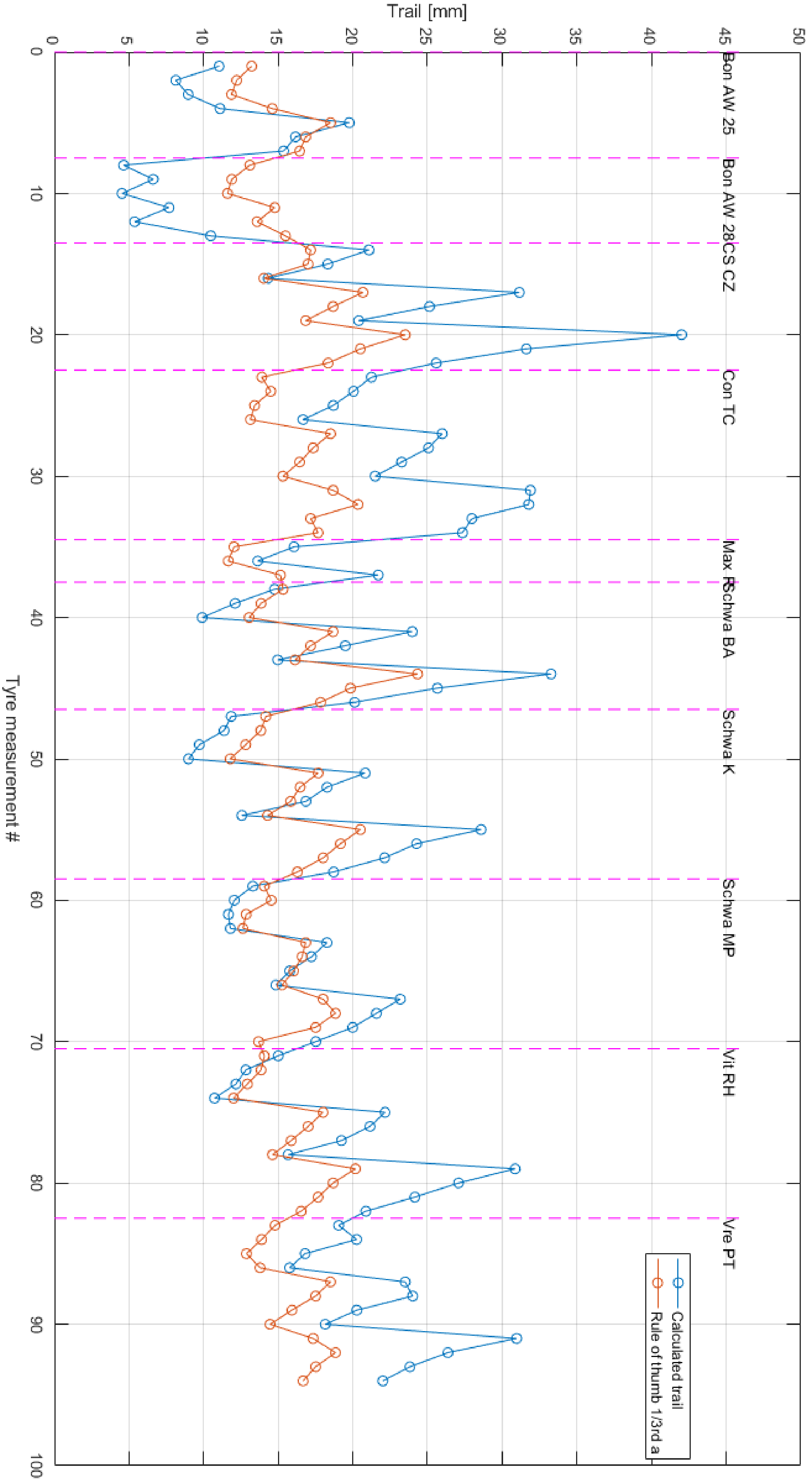

Figure 5.4: Pneumatic trail from all the tested tyres obtained in two different ways.

5.1.3. Self-aligning torque and spin stiffness

Figure 5.5 shows the self-aligning torque stiffness and spin stiffness. As shown in section 2.1.2 these two stiffnesses are equal to each other. A closer look at the measurement graphs for the self-aligning torque from Dressel [4], shows that these measurements are not that smooth as the ones for cornering stiffness and camber stiffness. Therefore the self-aligning torque stiffness will be calculated from the cornering stiffness (the red line). The measured self-aligning torque stiffness is shown in blue. These will be compared with each other and also with the spin stiffness. The spin stiffness is calculated in two ways: one with the undeformed tyre radius (the yellow line) and the other one with the deformed tyre radius (the purple line). The deformed tyre radius is calculated using the data from the Bachelor Thesis [5]. This data is not available for every tyre. It can be seen that there is only a small difference between the yellow and purple line. In general the data from the spin stiffness is matching relatively well with the calculated self-aligning torque. Even the measured self-aligning torque is not that far off from matching with the others. Again exceptions are the Bontrager and Maxxis tyres. For these it seems that the measured self-aligning torque and the calculated self-aligning torque are matching and the spin stiffness is way off. From this it can be cautiously said that small tyres have a bigger difference between self-aligning torque stiffness and spin stiffness.

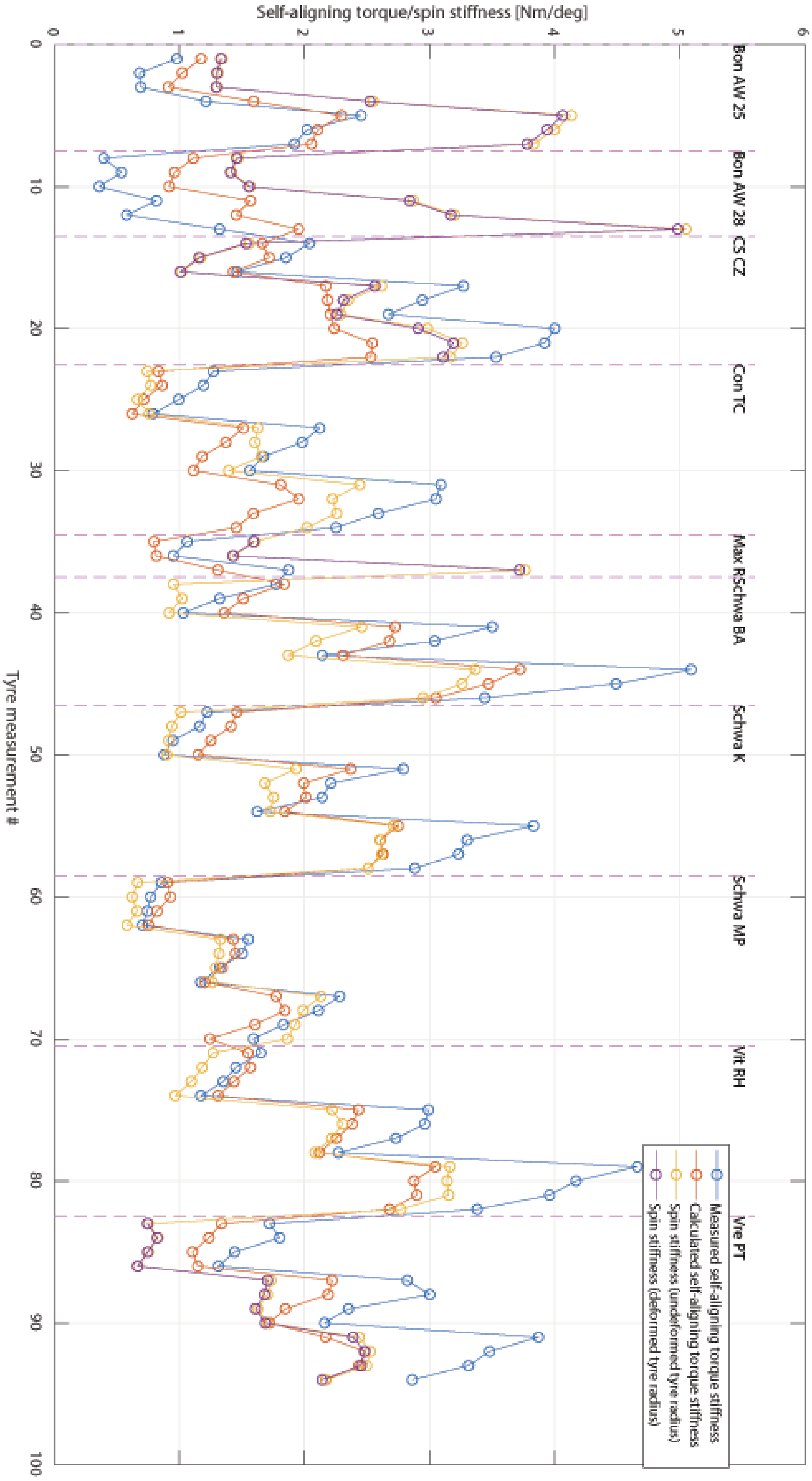

Figure 5.5: Self-aligning torque stiffness from all the tested tyres obtained in four different ways.

5.2. Results of the enhanced string model

5.2.1. Vertical parameters

As explained in Chapter 4 the data for the Bontrager tyres is not 100% complete, so for these tyres two dimensional graphs are created. These graphs are depicted in Appendix B. The data from the Cheng Shin Classic Zeppelin and the Vredestein Perfect Tour is complete, so for these two tyres a surface plot can be created. These give a more complete view on how the k_{Wz} and k_{Pz} are related to the inflation pressure and the normal load. These graphs are shown in Figures 5.6, 5.8, 5.10 and 5.12. Both the Classic Zeppelin and the Perfect Tour have a nice tilted plane for the k_{Wz} and there is not so much difference between values calculated from the drum and plate contact lengths. The relation between the inflation pressure and the k_{Wz} is nicely linear. As the inflation pressure increases, k_{Wz} also increases. It seems that for the Vredestein Perfect Tour the k_{Wz} is slightly decreasing for increasing normal loads and that it stays constant for the Cheng Shin Classic Zeppelin. The relation for k_{Pz} is not unambiguous. The relation between the normal load and the k_{Pz} cannot be found when looking at the values in Table 5.3 & 5.4. It is expected that the k_{Pz} increases for increasing inflation pressure. This effect is mildly visible for the contact patch data from the drum, but not really for the flat plate data. Also for some data points of k_{Pz} there is a big difference between the drum and flat plate. This might be caused by the contact patch length data. Studying the contact length data, some "outliers" are spotted. An outlier in this case means that the contact patch length is expected to be lower or higher than it actually is. For example, the inflation pressure is increased, so the contact patch length should decrease, but this is not seen in the values. To be able to say something more about this, the inverse of the contact patch length will be plotted. These graphs are shown in Figures 5.9 and 5.13. The reason for choosing the inverse of the contact length patch, is that a smaller contact patch appears bigger in the graph, just as is expected with the k_{Pz}.

For the Cheng Shin Classic Zeppelin, it can be seen that the k_{Pz} along the 31 kg line is influenced by values of the contact patch length data. Even k_{Wz} is slightly influenced by this. The outlier at the highest load and pressure combination in the k_{Pz} graph cannot be explained by the inverted contact patch length graph.

The found k_{Pz} values for the Vredestein Perfect Tour are very much relatable to the inverted contact patch lengths. The lines along the different inflation pressures are very much similar. Even the outlier at lowest pressure and highest normal load shows the same behaviour with the inverted contact patch length.

Another observation is that the k_{Wz} value is mostly determined by the vertical stiffness. The planes of the vertical stiffnesses in Figures 5.7 and 5.11 show a similar behaviour to the planes of the calculated k_{Wz} values. Figure 5.14 shows the vertical stiffness as a function of k_{Wz} and k_{Pz}. Here it is indeed visible that k_{Wz} influences the vertical stiffness more than k_{Pz}. Note that the range of both values differ a lot, this definitely has an effect on how much they each influence the vertical stiffness, but these range of parameters are extracted from the measurements.

Comparing Figure 5.14 to Figures 5.7 and 5.11, it seems that the lines along the axis of the increasing normal load, are similar to the lines along the axis of increasing k_{Pz}. The same goes for the lines along the axis of increasing pressure, these are similar to the lines along the axis of increasing k_{Wz}. This means that the expectation of constant k_{Pz} for constant inflation pressure and increasing normal load is unfulfilled. Since the k_{Wz} influences the vertical stiffness more than the k_{Pz} in the same way that the inflation pressure has more influence on the vertical stiffness than the normal load, it seems that the k_{Wz} is closely related to the inflation pressure and k_{Pz} is closely related to the normal load.

Table 5.3: Cheng Shin Classic Zeppelin

Normal load [kg]	Pressure [bar]	$k_{Wz} \times 10^5$ (drum)	$k_{Wz} \times 10^5$ (plate)	k_{Pz} (drum)	k_{Pz} (plate)
33	2.0	7.58	8.04	178	40
33	3.0	13.31	12.36	8	216
33	4.0	16.72	17.51	268	113
55	2.0	8.32	8.69	161	17
55	3.0	12.84	13.38	159	1
55	4.0	17.08	18.03	305	57
74.5	2.0	8.30	8.54	132	22
74.5	3.0	10.27	10.73	409	200
74.5	4.0	13.48	15.05	732	129

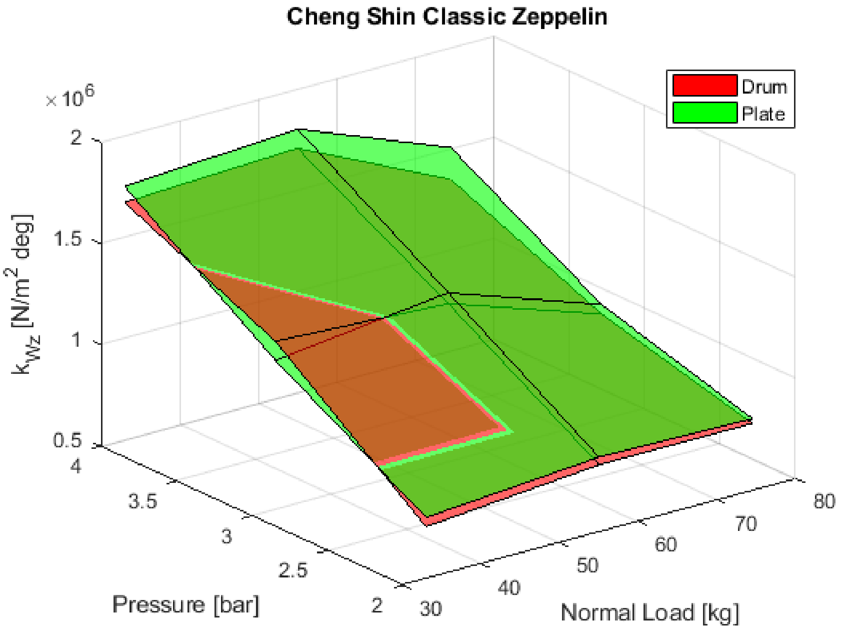

Figure 5.6: Results from the parameter optimisation for the Cheng Shin Classic Zeppelin 50.

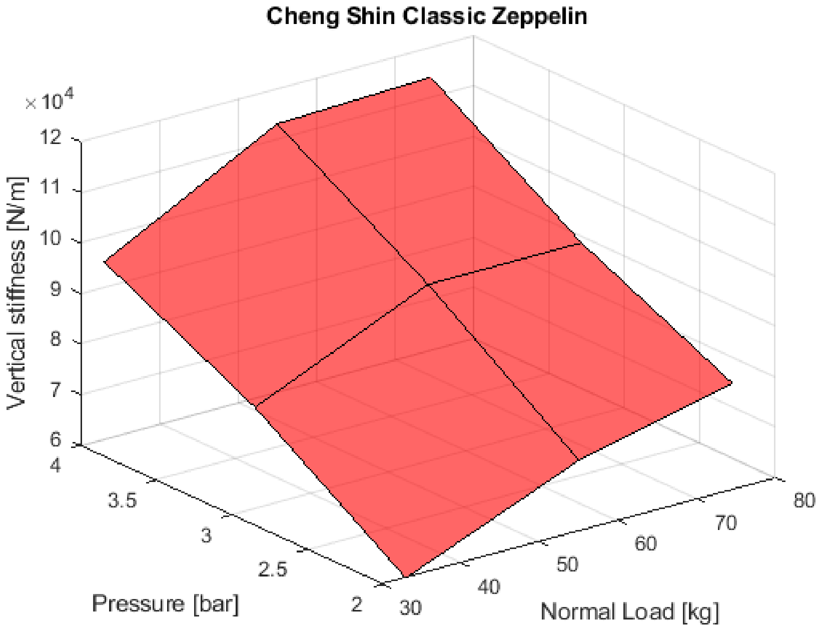

Figure 5.7: Vertical stiffness of the Cheng Shin Classic Zeppelin 50.

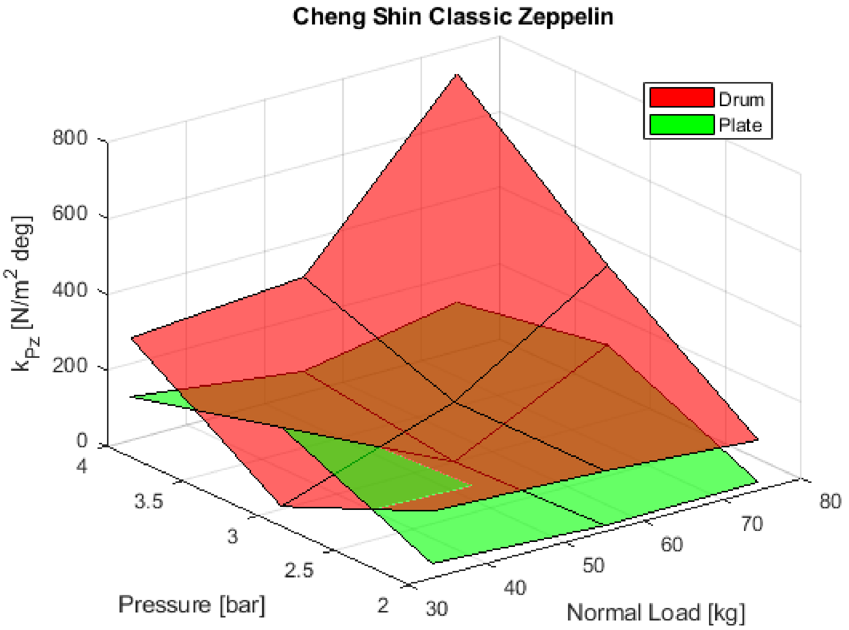

Figure 5.8: Results from the parameter optimisation for the Cheng Shin Classic Zeppelin 50.

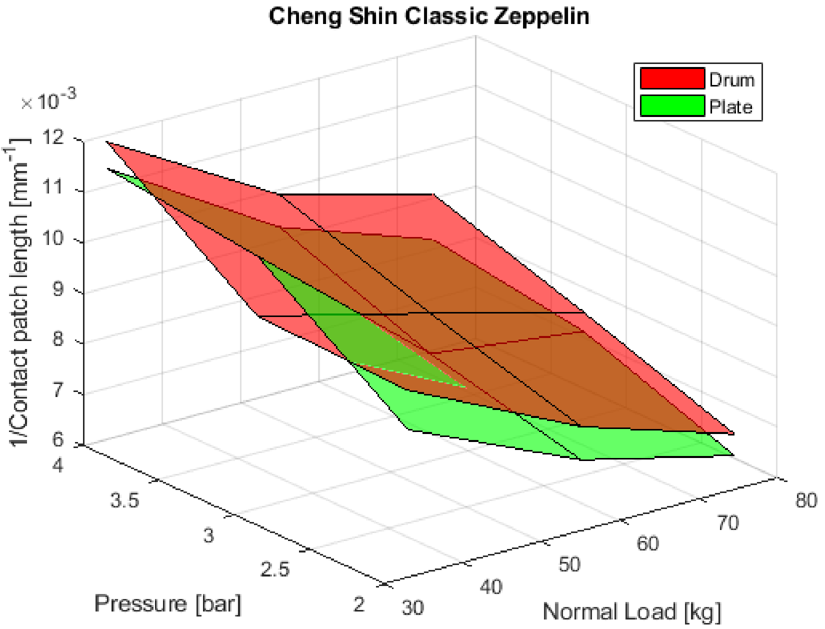

Figure 5.9: Inverted contact patch lengths for the Cheng Shin Classic Zeppelin 50.

Table 5.4: Vredestein Perfect Tour

Normal load [kg]	Pressure [bar]	$k_{Wz} \times 10^5$ (drum)	$k_{Wz} \times 10^5$ (plate)	k_{Pz} (drum)	k_{Pz} (plate)
31	3.4	15.09	15.63	120	19
31	4.0	19.08	19.87	150	19
31	4.8	18.15	19.91	464	136
31	6.2	30.77	30.77	0	0
53.5	3.4	13.97	14.31	107	14
53.5	4.0	16.49	17.10	153	0
53.5	4.8	19.41	21.06	408	13
53.5	6.2	25.18	27.42	812	294
74.5	3.4	9.36	12.35	1616	127
74.5	4.0	13.15	14.04	591	237
74.5	4.8	15.36	17.59	922	120
74.5	6.2	21.02	23.81	938	96

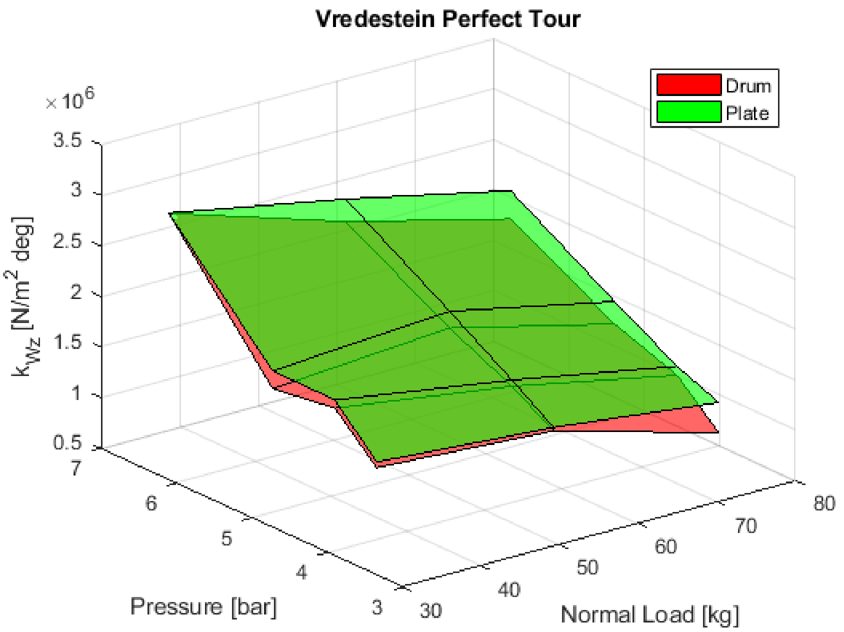

Figure 5.10: Results from the parameter optimisation for the Vredestein Perfect Tour 37.

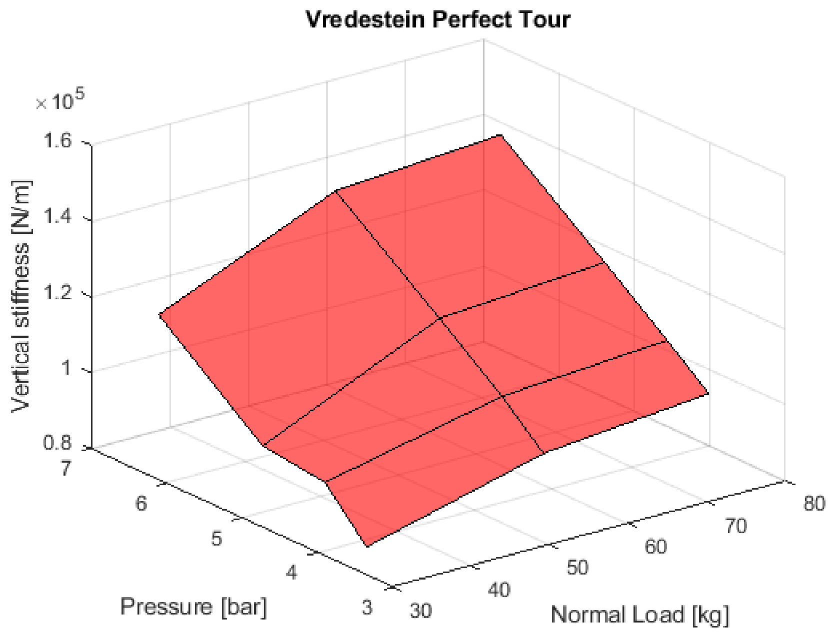

Figure 5.11: Vertical stiffness of the Vredestein Perfect Tour 37.

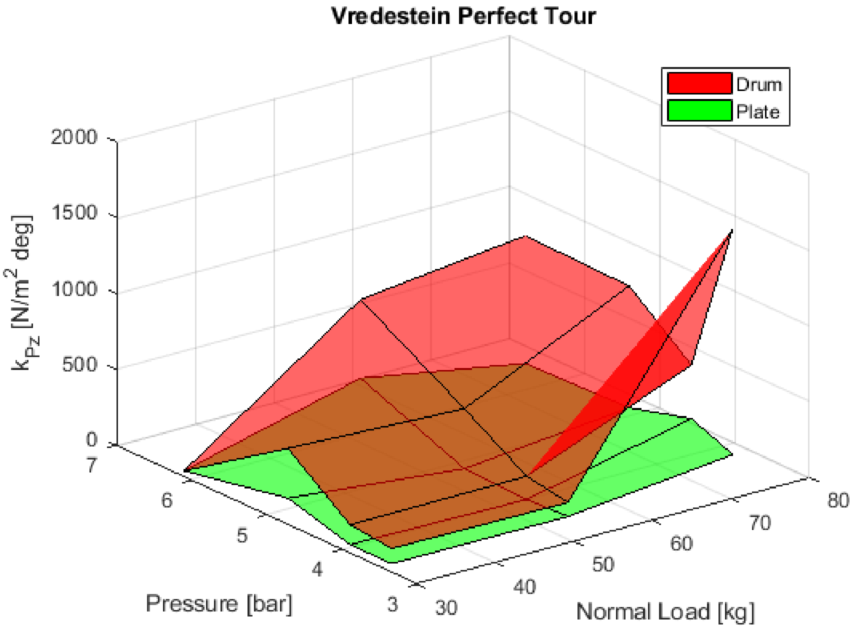

Figure 5.12: Results from the parameter optimisation for the Vredestein Perfect Tour 37.

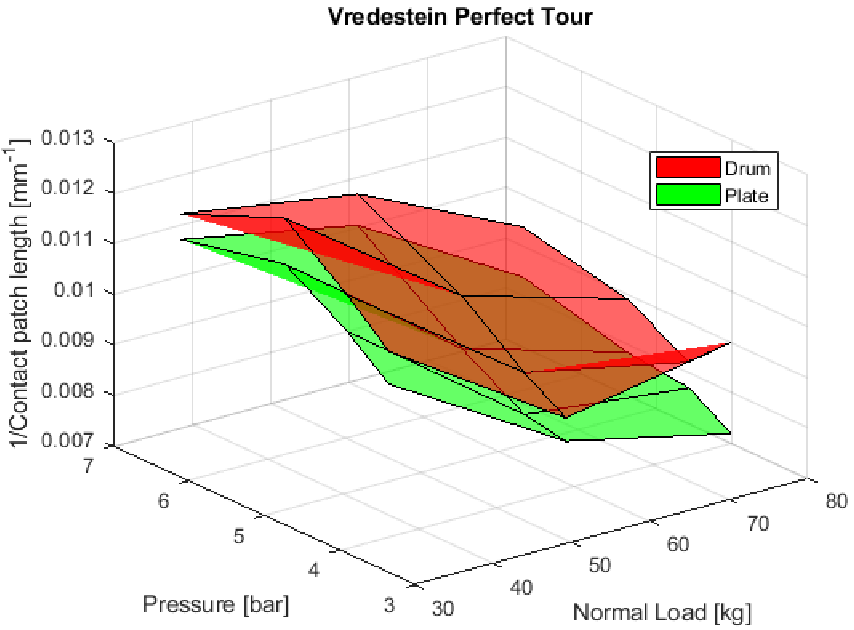

Figure 5.13: Inverted contact patch lengths for the Vredestein Perfect Tour 37.

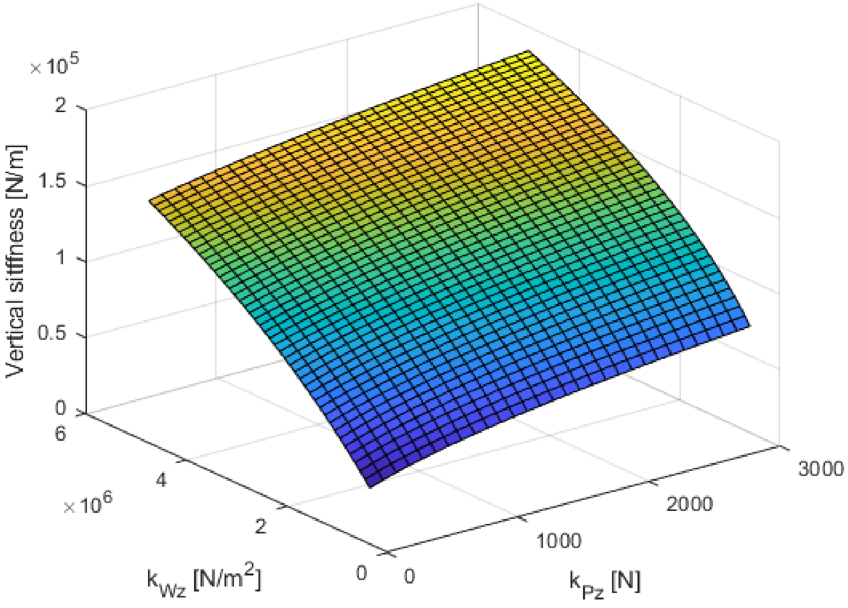

Figure 5.14: The vertical stiffness as a function of k_{Wz} and k_{Pz}

5.2.2. Lateral parameters

The results of the optimisation for the lateral parameters are shown in this section. Two comparisons are made with the results. The first one is the parameter difference due to a flat plate or drum contact patch length. The second comparison is between the cornering, self-aligning torque and camber stiffness. As mentioned before in the vertical parameter section, the data for the Bontrager tyres is not 100% complete such that only two dimensional graphs can be created. These graphs are shown in Appendix B.

Drum-plate comparison

The surface plots from the Cheng Shin Classic Zeppelin and the Vredestein Perfect Tour are shown in Figures 5.15 and 5.16. The corresponding values are depicted in Table 5.5 & 5.6.

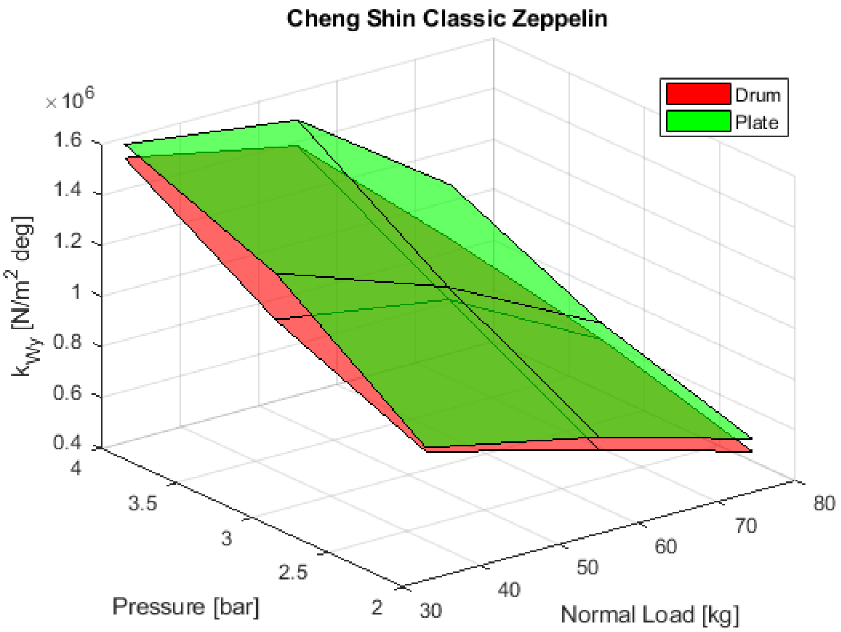

Figure 5.15: Results from the parameter optimisation for the Cheng Shin Classic Zeppelin 50.

From these figures it can be concluded that the k_{Wy} decreases when the normal load increases. The influence of the inflation pressure on this parameter is not unambiguous. For the Cheng Shin Classic Zeppelin the k_{Wy} increases with increasing pressure. For the Vredestein Perfect Tour it seems more like the k_{Wy} stays around the same value or increases a bit for increasing inflation pressure. The influence of the pressure on k_{Wy} for Bontrager All Weather seems to be negligible, k_{Wy} remains fairly constant as can be seen in Figures B.7 and B.8.

Table 5.5: Cheng Shin Classic Zeppelin

Normal load [kg]	Pressure [bar]	$k_{Wy} \times 10^5$ (drum)	$k_{Wy} \times 10^5$ (plate)
33	2.0	7.75	7.98
33	3.0	11.57	11.59
33	4.0	14.48	15.01
55	2.0	5.24	5.76
55	3.0	8.25	11.00
55	4.0	11.83	12.81
74.5	2.0	3.38	3.83
74.5	3.0	5.13	5.73
74.5	4.0	6.66	8.67

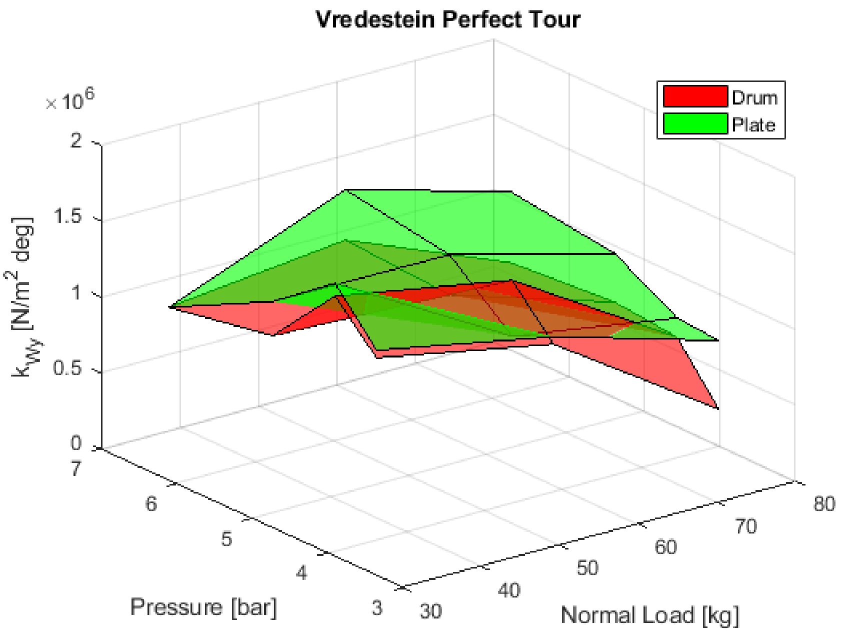

Figure 5.16: Results from the parameter optimisation for the Vredestein Perfect Tour 37.

Table 5.6: Vredestein Perfect Tour

Normal load [kg]	Pressure [bar]	$k_{Wy} \times 10^5$ (drum)	$k_{Wy} \times 10^5$ (plate)
31	3.4	11.71	12.24
31	4.0	13.22	14.15
31	4.8	10.59	12.72
31	6.2	11.00	11.00
53.5	3.4	9.52	9.98
53.5	4.0	11.27	11.00
53.5	4.8	10.05	12.39
53.5	6.2	10.59	13.68
74.5	3.4	2.33	6.54
74.5	4.0	6.26	7.42
74.5	4.8	6.77	9.73
74.5	6.2	6.65	10.72

Cornering, self-aligning torque and camber stiffness comparison

The comparison between the k_{Wy} parameters found from different measurements are shown in Figures 5.17 and 5.18. For the Cheng Shin Classic Zeppelin the three surfaces are relatively similar, especially for the lower normal load. However, the difference between the surfaces is a lot bigger than for the drum-plate comparison. The k_{Wy} increases as the inflation pressure increases for every stiffness and the k_{Wy} seems to decrease as the normal force increases, except for the camber stiffness. For this stiffness it is not really possible to say something useful about the relation.

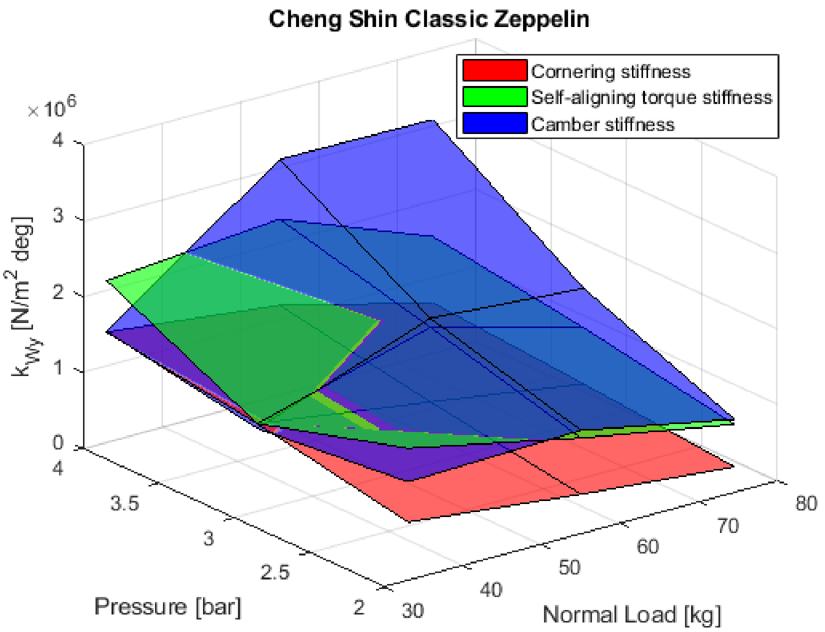

Figure 5.17: Results from the parameter optimisation for the Cheng Shin Classic Zeppelin 50.

Table 5.7: Cheng Shin Classic Zeppelin

Normal load [kg]	Pressure [bar]	$k_{Wy} \times 10^5$ (corner)	$k_{Wy} \times 10^5$ (self-aligning)	$k_{Wy} \times 10^5$ (camber)
33	2.0	7.75	17.48	13.07
33	3.0	11.57	11.57	10.94
33	4.0	14.48	21.26	14.58
55	2.0	5.24	12.65	13.66
55	3.0	8.25	18.08	19.28
55	4.0	11.83	23.18	31.04
74.5	2.0	3.38	8.97	9.64
74.5	3.0	5.13	12.55	17.72
74.5	4.0	6.66	15.39	30.83

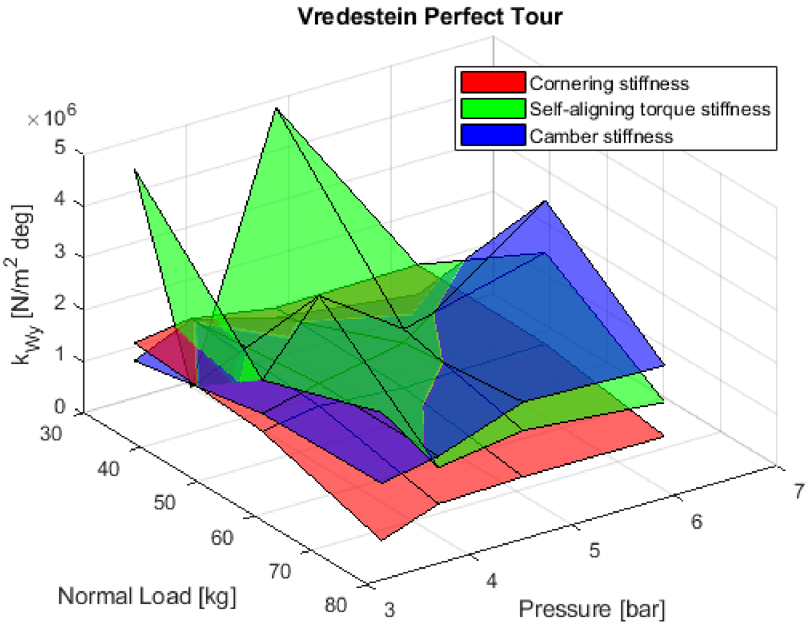

Figure 5.18: Results from the parameter optimisation for the Vredestein Perfect Tour 37.

Table 5.8: Vredestein Perfect Tour

Normal load [kg]	Pressure [bar]	$k_{Wy} \times 10^5$ (corner)	$k_{Wy} \times 10^5$ (self-aligning)	$k_{Wy} \times 10^5$ (camber)
31	3.4	11.71	45.22	8.27
31	4.0	13.22	0	13.03
31	4.8	10.59	49.21	8.74
31	6.2	11.00	11	5.22
53.5	3.4	9.52	19.40	12.96
53.5	4.0	11.27	32.52	15.58
53.5	4.8	10.05	21.38	18.69
53.5	6.2	10.59	28.22	38.30
74.5	3.4	2.33	27.07	13.42
74.5	4.0	6.26	13.28	15.44
74.5	4.8	6.77	15.67	21.19
74.5	6.2	6.65	13.26	20.30

For the Vredestein Perfect Tour tyre, the camber stiffness surface is relatively similar to the surface of the cornering stiffness. Also for this tyre, this similarity is more valid for the lower normal load. The self-aligning torque stiffness has some outlying results. In general the k_{Wy} seems to increase with increasing inflation pressure for the cornering and camber stiffness. The self-aligning torque data is so scattered, that it is not possible to find the relations.

Something noticeable, is that this single material parameter k_{Wy} determines the cornering, self-aligning torque and camber stiffness. This also means that putting the found values into the enhanced string model, only one of these stiffnesses will be correct. So for instance, putting the k_{Wy} corresponding to the cornering stiffness into the model, only the cornering stiffness will match with the value of the measured tyre and the self-aligning torque and camber stiffness will not be exactly matching. This can be seen in most of the Figures in Appendix B.3. Appendix B.3 contains the measured data from Dressel (black lines) with an overlay that shows the model output (blue line). The extracted stiffness value from Dressel is shown as a solid grey line, which should also be the constant slope of the model output (as the parameter optimisation did its work correctly). Interestingly, for the Cheng Shin Classic Zeppelin some are matching quite closely for all three values, for example Figure 5.19 below. Also the overlays of the Vredestein Perfect Tour are not too bad. The overlays for the Bontrager All Weather are most off from these three tyres, but as can be seen in the tables in the bottom right corner of the figures, the model stiffness values are still matching the measured stiffness values, which indicates that the parameter optimisation worked. However, the enhanced string model is not able to describe the full lateral force graph accurately in the case of the Bontrager All Weather tyre.

The strange thing is that in Table 5.7, the values of k_{Wy} corresponding to the different stiffnesses are quite different from each other, however, in Figure 5.19 the graphs are quite accurately matched, even for the self-aligning torque and camber stiffness, while the k_{Wy} of the cornering stiffness was used.

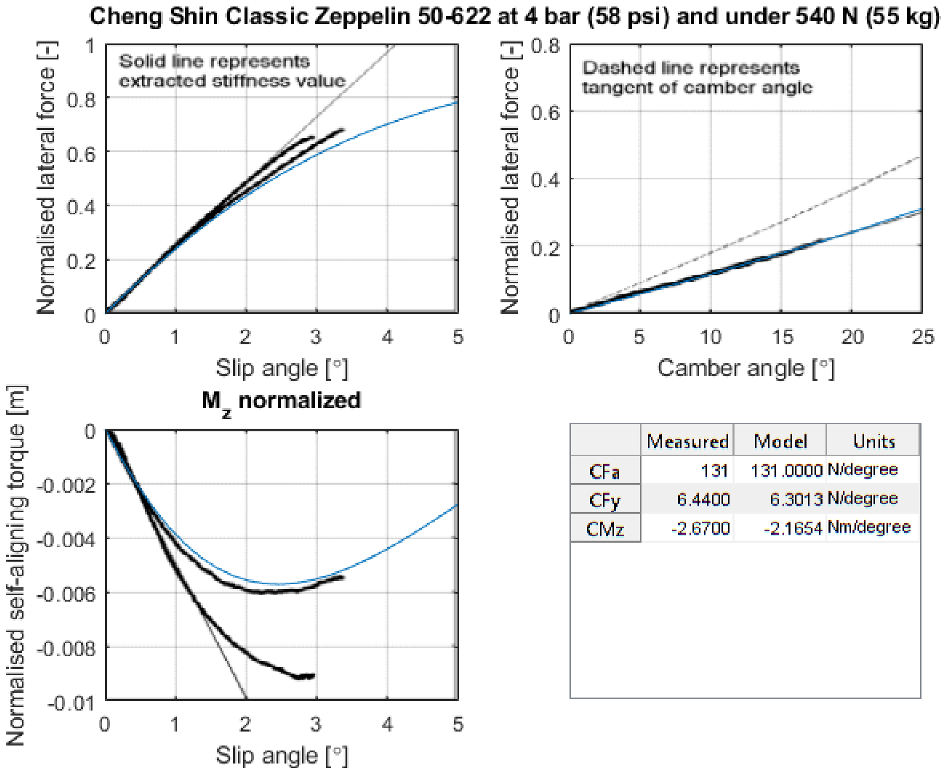

	Measured	Model	Units
CFa	131	131.0000	N/degree
CFy	6.4400	6.3013	N/degree
CMz	-2.6700	-2.1654	Nm/degree

Figure 5.19: Measurement results from Andrew Dressel and an overlay of the model output.

The fact that material parameter k_{Wy} determines all three values and the quality of the overlays becomes better as the width of the tyre increases, one might wonder if this a coincidence or not. As the name already suggests, the enhanced string model models the tyre as a string and does not take the width of the tyre into account. It is remarkable that as the width increases the values of the camber and self-aligning torque stiffness are more closely matched.

5.2.3. Influence of alterations in the obtained values

It is interesting to know the influence of the material parameters on the contact patch length, cornering and camber stiffness. The obtained values from the parameter optimisation will be altered by 20% and then normalised to see the influence. Furthermore an alteration in normal load is made to compare its influence to the influence of the material parameters. The results are shown in Figures 5.20, 5.21 and 5.22. For every tyre a single situation (normal load and inflation pressure) is chosen. The 20% alteration of the normal load has the most influence on contact patch length, cornering and camber stiffness. This is valid for all the tyres. From the figures it is also visible that the lateral material parameters have more influence on the cornering and camber stiffness than the vertical material parameters.

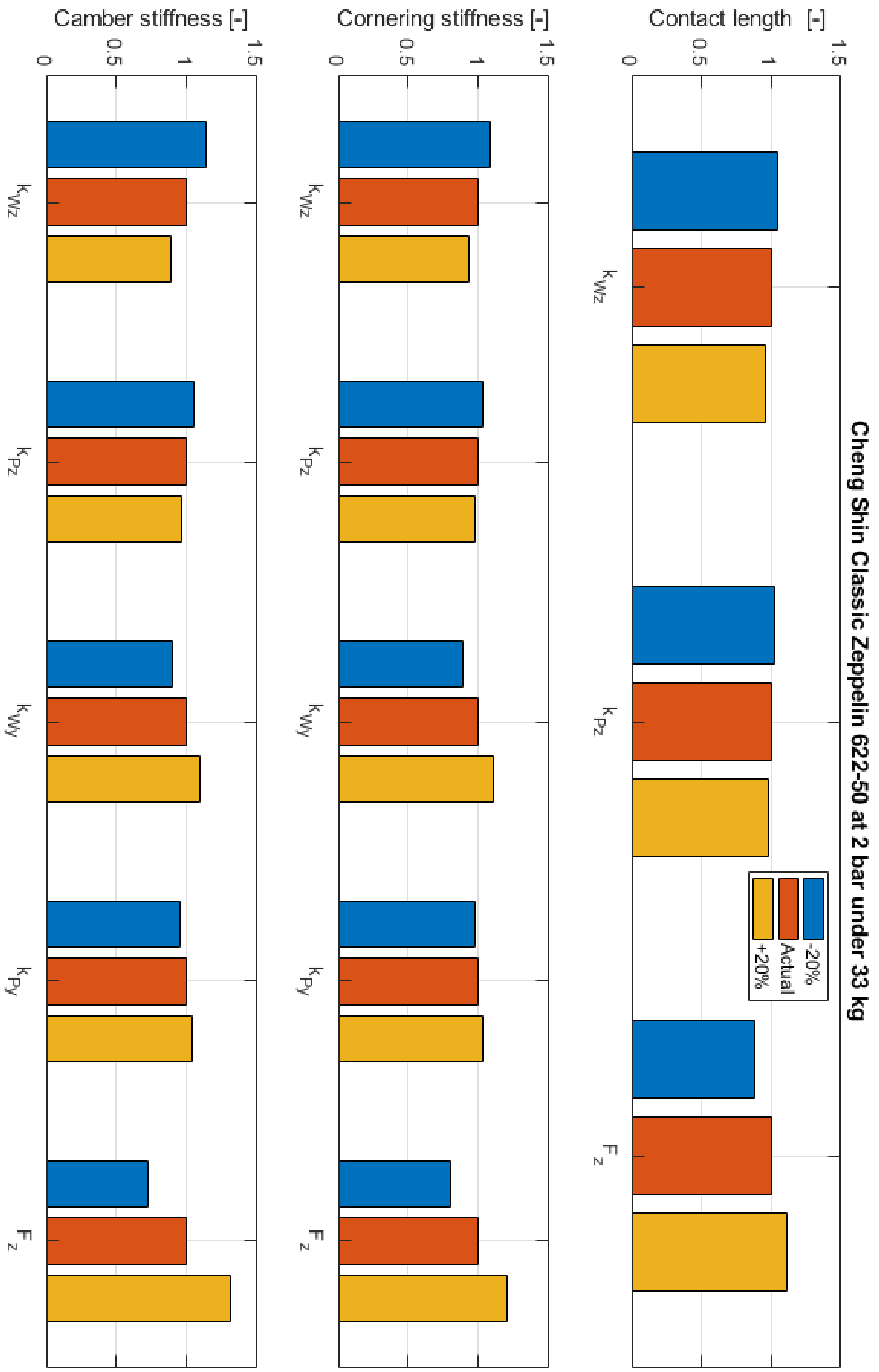

Figure 5.20: Altering the parameters to see the influence for the Cheng Shin Classic Zeppelin at 2 bar under 33 kg.

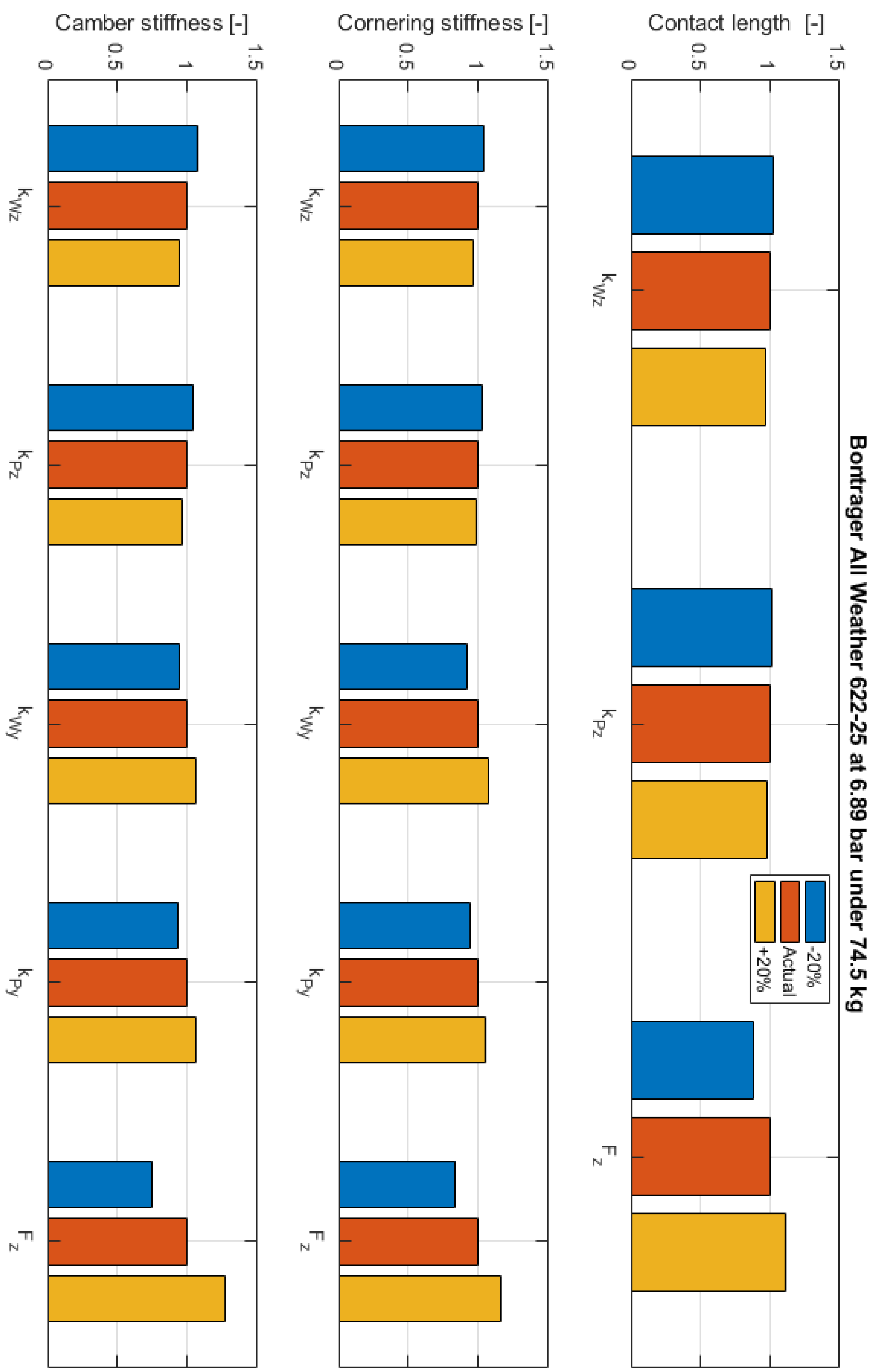

Figure 5.21: Altering the parameters to see the influence for the Bontrager All Weather at 6.89 bar under 74.5 kg.

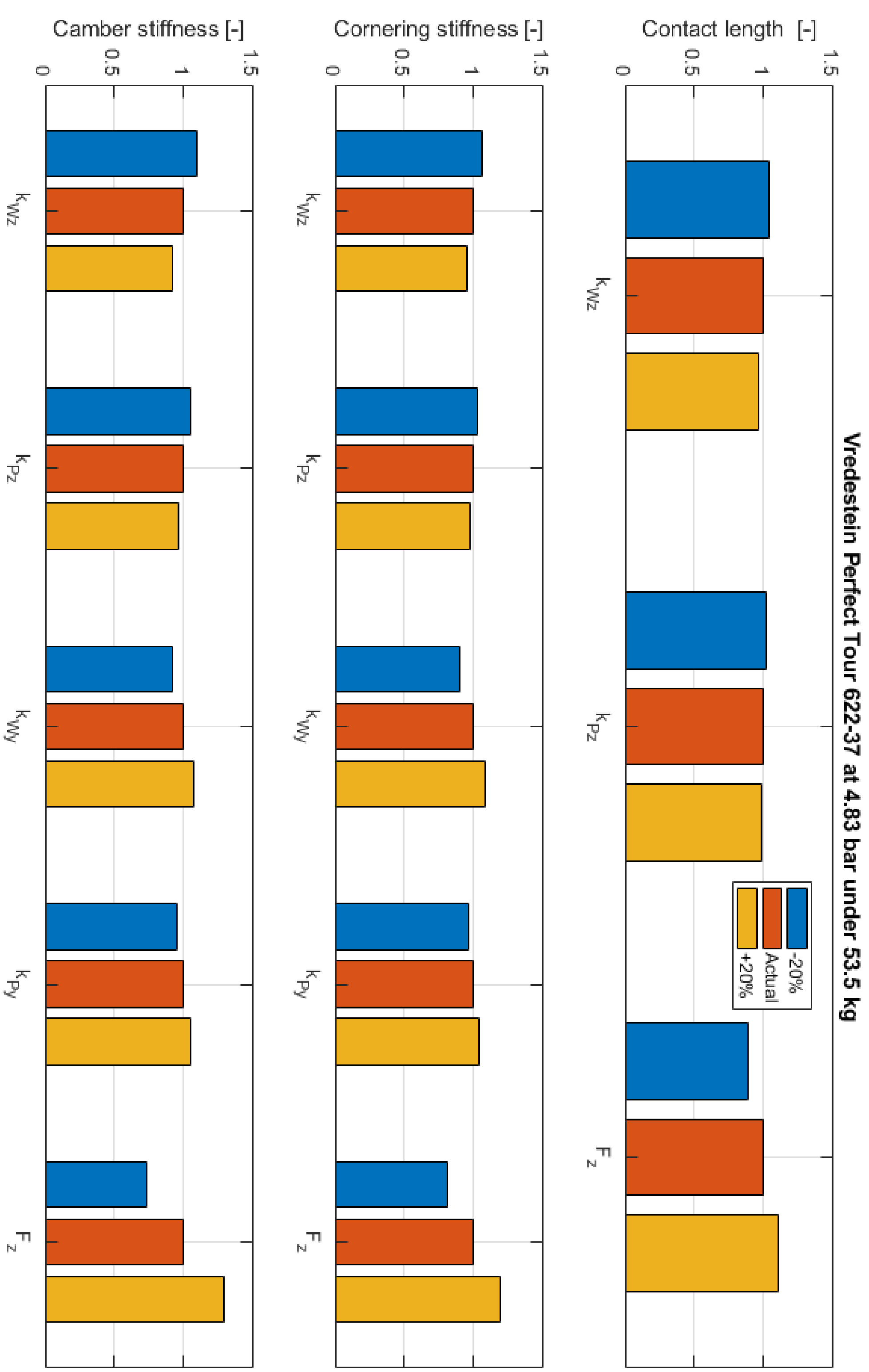

Figure 5.22: Altering the parameters to see the influence for the Vredestein Perfect Tour at 4.83 bar under 53.5 kg.

6

Discussion

6.1. Discussion of the tyre brush model results

As mentioned in the Chapter 2, a drawback of the single parameter model is that all known tyre parameters are included in that single model parameter. The results show this very well, since material parameter c_{py} is dependent on the normal load, inflation pressure and probably also the tyre width, rim width and kind of rubber because the c_{py} surface plot is different for every tyre. This makes it hard to find the exact relation between the material parameter and the known tyre parameters.

An interesting observations is that the foldable tyres have a slightly higher c_{py} value calculated from the camber stiffness compared to the ones with a wire and similar width. Also the general relation between c_{py} and the inflation pressure is that it increases with increasing inflation pressure. Not a lot can be concluded in general about the influence of the normal load on c_{py}, because for increasing normal load the c_{py} for some tyres increases, for others it decreases and for some others it stays the same or even oscillates.

The calculated pneumatic trail is larger than one-sixth of the contact patch length, Pacejka's rule of thumb for pneumatic trail. The calculated pneumatic trail approaches one-sixth of the contact patch length as the inflation pressure increases and the normal load decreases.

6.2. Discussion of the enhanced string model results

The advantage of the enhanced string model over the tyre brush model from previous chapter is that this model has multiple material parameters. It was expected that the shear stiffness of the foundation represented by k_{Pz} and k_{Py} for the vertical and lateral direction respectively would be more, if not completely be influenced by the inflation pressure. This suspicion was created by inspecting the influence of k_{Pz} on the contact patch length (Figure 3.2). Increasing the k_{Pz}, shortened the contact patch length. However, the results show that k_{Wz} is pressure dependent and the influence of k_{Pz} is questionable. There is no clear relation between k_{Pz}, the inflation pressure and the normal load. Interestingly, as was found during the investigation of the enhanced string model in Chapter 3, the contact patch does influence the k_{Pz}. This is also seen when the inverse contact patch length is plotted under the results of k_{Pz} for both the Cheng Shin Classic Zeppelin and the Vredestein Perfect Tour. However, apparently the influence that the inflation pressure has on the vertical stiffness, which in its turn influences k_{Wz}, is bigger than the effect of the inflation pressure on the contact patch length and therefor also affecting k_{Pz} less. One thing is clear and that is that k_{Pz} is not equal to the inflation pressure.

The model output agrees fairly well with the measurements as turns out from the many overlay plots shown in Appendix B.3 and this seems to be more true as the width of the tyre increases. To be able to say more about this, more complete measurements are needed. Something unexpected is that the overlays that match quite closely both in graph lines and in stiffness values, have quite different values of k_{Wy}. An explanation for this might be that the influence of changing k_{Wy} has a bigger effect on the cornering stiffness than on the self-aligning torque and the camber stiffness. However, this is not really seen in Figure 5.20.

It might be still possible to estimate the model parameters for a given tyre with a certain inflation pressure, tyre width and rim width. However, in order to do that, more complete measurements are needed and these measurements should be put through the parameter optimisation in order to find the corresponding material parameters. Then the relation between the material parameters and inflation pressure, tyre width and rim width can be investigated further.

Something to take into account when using a tyre model is that small alterations (20% of its normal value) in the model parameters do not affect the tyre behaviour by a huge amount. It seems that similar alterations in the normal load have the most affect on tyre behaviour.

7

Conclusions and Future Work

7.1. Conclusion

The research question was formulated as: *Is it possible to estimate bicycle tyre behaviour in terms of vertical stiffness, cornering stiffness and camber stiffness based on known parameters like the inflation pressure, tyre width, rim width, vertical load and the rubber compound using a tyre model?*

The answer to this question for the tyre brush model is no. For the enhanced string model the answer is also no for now, but this is a less definite no than for the tyre brush model for the reasons explained below.

The results from both tyre models show that the material parameters are within a certain value range for the measured bicycle tyres. Moreover, the enhanced string model showed that it can replicate the measured tyre behaviour quite accurately. The problem is that for now it requires a lot of work to obtain the right model parameter values. The tests needed to find these are almost just as extensive as the tests needed for finding the parameters for Pacejka's Magic Formula. The motivation for this research is to be able to make an estimation of any bicycle tyre behaviour based on it's known parameters. Unfortunately there were only two sets of complete measurement data (Cheng Shin Classic Zeppelin and Vredestein Perfect Tour). These only give a rough estimation of the model parameter range and a small indication of the relation between the model parameters and the vertical, cornering, self-aligning torque and camber stiffness.

It would be interesting to see results with more sets of complete measurement data and also measurements carried out in a single research. More sets of complete measurement data means more data points for a single tyre, but also more different types of tyres. Also a single research means experiments carried out by the same person in the same environment and in the same period, since in this research, data from the Bachelor group was combined with Dressels data in order to come to these results. This could lead to a much better indication of whether it is possible to estimate bicycle tyre behaviour based on known parameters using a tyre model. The current results are promising, in my opinion. The extracted relations are not entirely according to what was expected, but that does not mean that it is not possible to estimate bicycle tyre behaviour based on known parameters using a tyre model.

7.2. Future work

With the methods described in this research it is possible to find the model parameters from bicycle tyre measurements. As the answer to the research question now remains negative, it would be interesting to know how more complete sets of measurement data would affect the answer to the research question. To make this more specific: As mentioned in the discussion, the model output agrees fairly well with the measurements and this seems to be more true as the width of the tyre increases. So for a future research it would be interesting to do the following: pick two or three different brand tyres, preferably fat tyres but all with an equal width and on the same rim. Do the measurements like Dressel did, but now with smaller increments for the pressure and normal load. Also more than three data points are needed. It is very important to also measure the vertical stiffness of the tyre and the contact patch for each pressure and normal load combination. All of this should be executed very accurate, because as has been observed in the results, small deviations lead to incorrect model parameters. It is expected that a significant amount of these deviations are caused by combining measurements from separate researches (Dressel and the Bachelor group). Once the measurements have been performed, the parameter optimisation from this research can be used to find the enhanced string model parameters. It is expected that for the two or three different tyres similar enhanced string model parameters will be found. If this indeed seems to be true, it would be interesting to see how the tyre width influences the model parameters and if the model output can also also agree with the measurement for thinner tyres.

A

Results for the tyre brush model

A.1. Material parameter

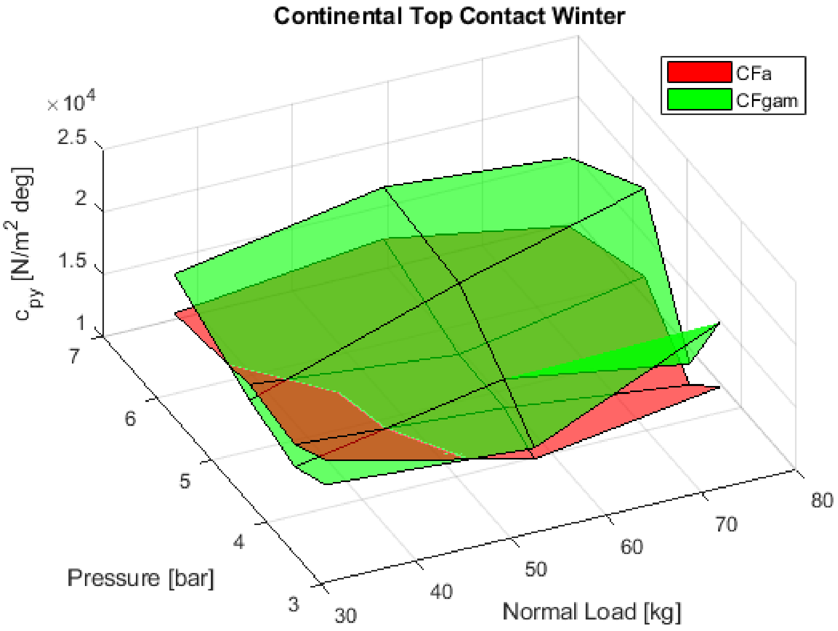

Figure A.1: Material parameter c_{py} for Continental Top Contact Winter.

Table A.1: Continental Top Contact Winter

Normal load [kg]	Pressure [bar]	$c_{py} \times 10^4$ (cornering)	$c_{py} \times 10^4$ (camber)
33	3.4	1.72	1.52
33	4.0	1.57	1.39
33	4.8	1.64	1.51
33	6.2	1.52	1.84
55	3.4	1.32	1.41
55	4.0	1.46	1.69
55	4.8	1.48	2.05
55	6.2	1.72	2.13
74.5	3.4	1.55	2.07
74.5	4.0	1.29	1.46
74.5	4.8	1.75	2.45
74.5	6.2	1.46	2.02

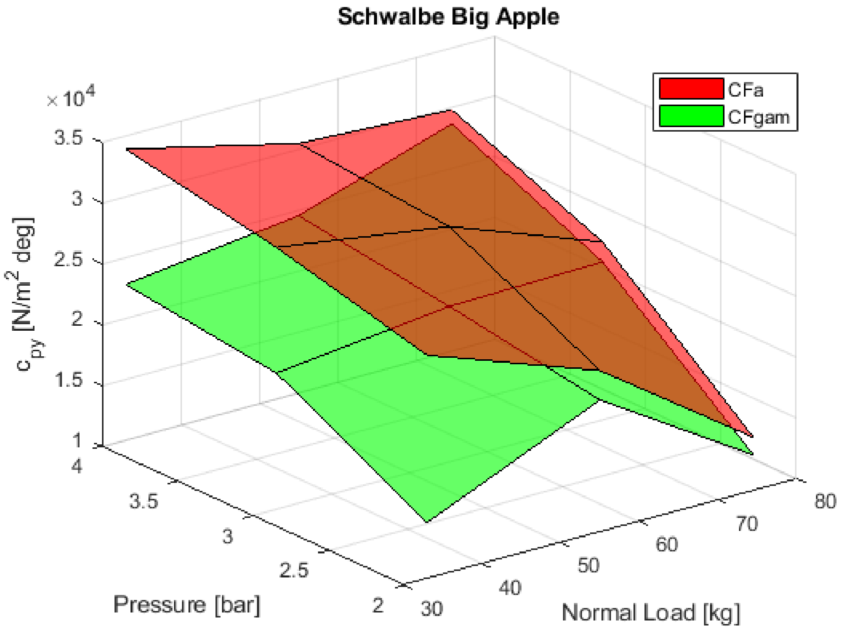

Figure A.2: Material parameter c_{py} for Schwalbe Big Apple.

Table A.2: Schwalbe Big Apple

Normal load [kg]	Pressure [bar]	$c_{py} \times 10^4$ (cornering)	$c_{py} \times 10^4$ (camber)
33	2.0	2.84	1.46
33	3.0	3.16	2.12
33	4.0	3.39	2.28
55	2.0	2.33	2.09
55	3.0	2.94	2.28
55	4.0	3.05	2.46
74.5	2.0	1.44	1.29
74.5	3.0	2.47	2.30
74.5	4.0	2.99	2.87

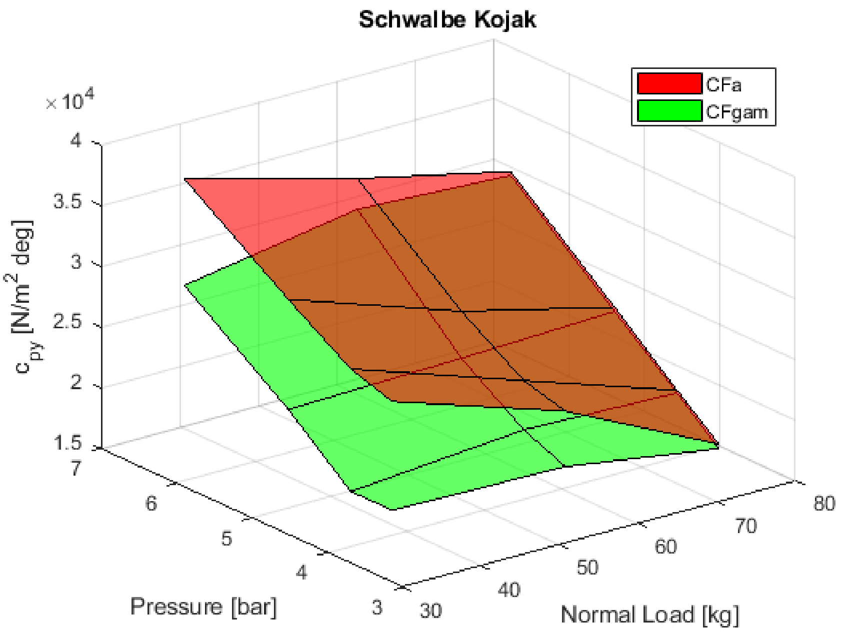

Figure A.3: Material parameter c_{py} for Schwalbe Kojak.

Table A.3: Schwalbe Kojak

Normal load [kg]	Pressure [bar]	$c_{py} \times 10^4$ (cornering)	$c_{py} \times 10^4$ (camber)
33	3.4	2.85	1.96
33	4.0	2.96	1.95
33	4.8	3.30	2.39
33	6.2	3.90	3.02
55	3.4	2.39	1.93
55	4.0	2.48	2.07
55	4.8	2.81	2.43
55	6.2	3.51	3.26
74.5	3.4	1.77	1.73
74.5	4.0	2.06	2.03
74.5	4.8	2.50	2.47
74.5	6.2	3.23	3.20

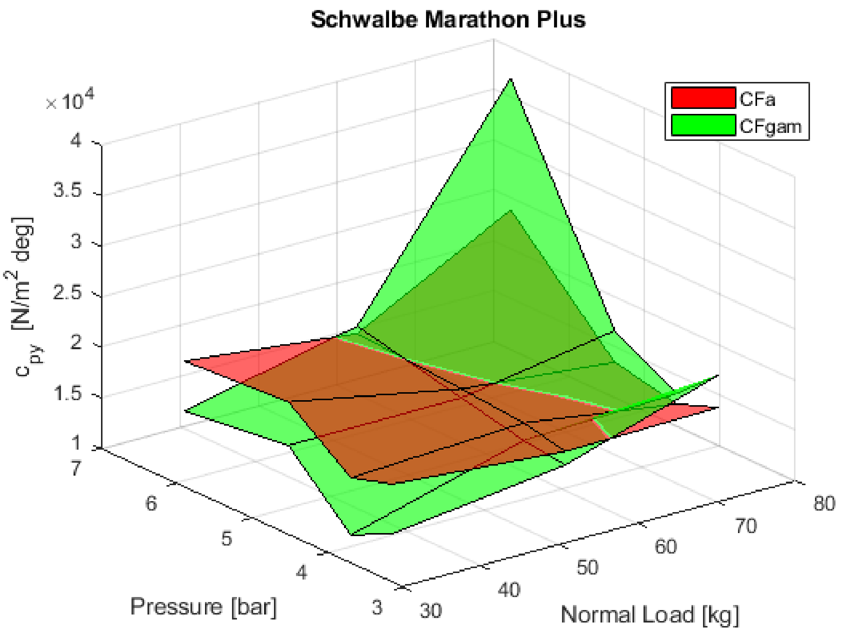

Figure A.4: Material parameter c_{py} for Schwalbe Marathon Plus.

Table A.4: Schwalbe Marathon Plus

Normal load [kg]	Pressure [bar]	$c_{py} \times 10^4$ (cornering)	$c_{py} \times 10^4$ (camber)
33	3.4	2.38	1.31
33	4.0	2.43	1.11
33	4.8	2.50	1.71
33	6.2	2.97	1.58
55	3.4	2.81	1.53
55	4.0	2.75	1.58
55	4.8	3.00	1.72
55	6.2	3.09	1.96
74.5	3.4	2.47	2.01
74.5	4.0	2.60	1.64
74.5	4.8	3.08	1.97
74.5	6.2	3.71	4.00

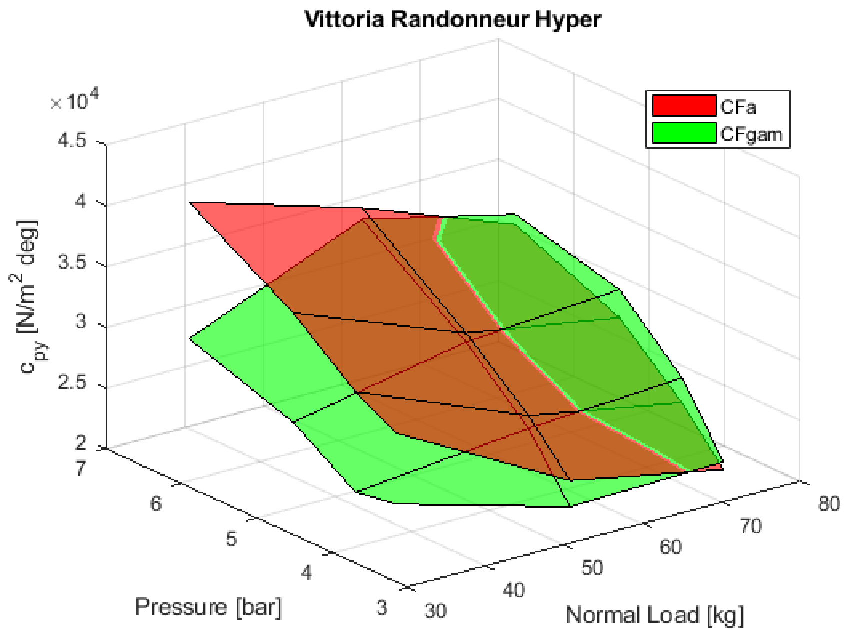

Figure A.5: Material parameter c_{py} for Vittoria Randonneur Hyper.

Table A.5: Vittoria Randonneur Hyper

Normal load [kg]	Pressure [bar]	$c_{py} \times 10^4$ (cornering)	$c_{py} \times 10^4$ (camber)
33	3.4	3.29	2.51
33	4.0	3.03	2.45
33	4.8	3.47	2.79
33	6.2	3.76	3.08
55	3.4	2.85	2.10
55	4.0	3.35	2.59
55	4.8	3.80	3.06
55	6.2	4.04	3.68
74.5	3.4	3.16	2.13
74.5	4.0	3.56	2.66
74.5	4.8	3.99	3.15
74.5	6.2	4.15	3.38

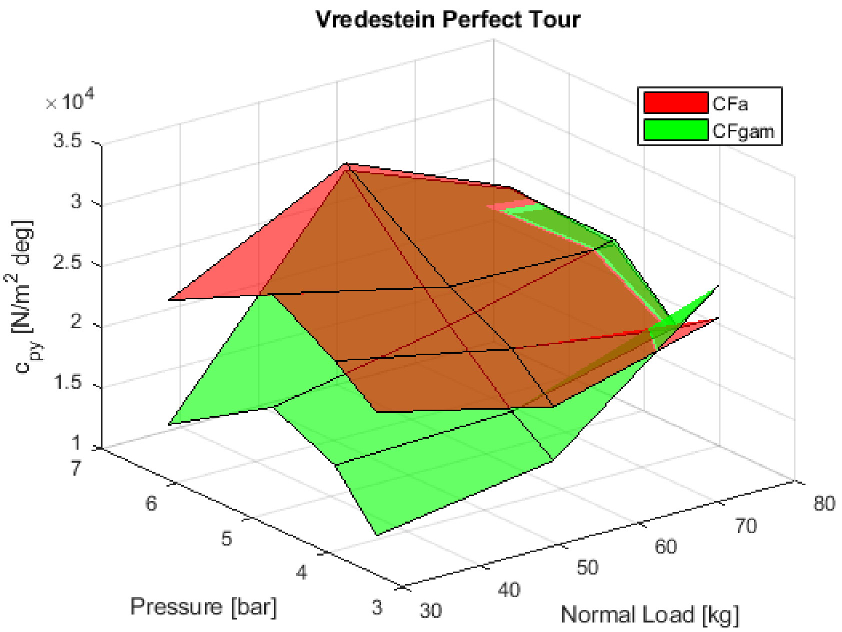

Figure A.6: Material parameter c_{py} for Vredestein Perfect Tour.

Table A.6: Vredestein Perfect Tour

Normal load [kg]	Pressure [bar]	$c_{py} \times 10^4$ (cornering)	$c_{py} \times 10^4$ (camber)
31	3.4	2.96	1.28
31	4.0	3.74	1.70
31	4.8	3.76	1.94
31	6.2	2.78	1.41
53.5	3.4	2.47	1.51
53.5	4.0	3.11	1.75
53.5	4.8	3.24	2.22
53.5	6.2	3.98	3.11
74.5	3.4	4.13	2.58
74.5	4.0	2.89	2.08
74.5	4.8	3.43	2.56
74.5	6.2	3.43	2.58

A.2. Pneumatic trail

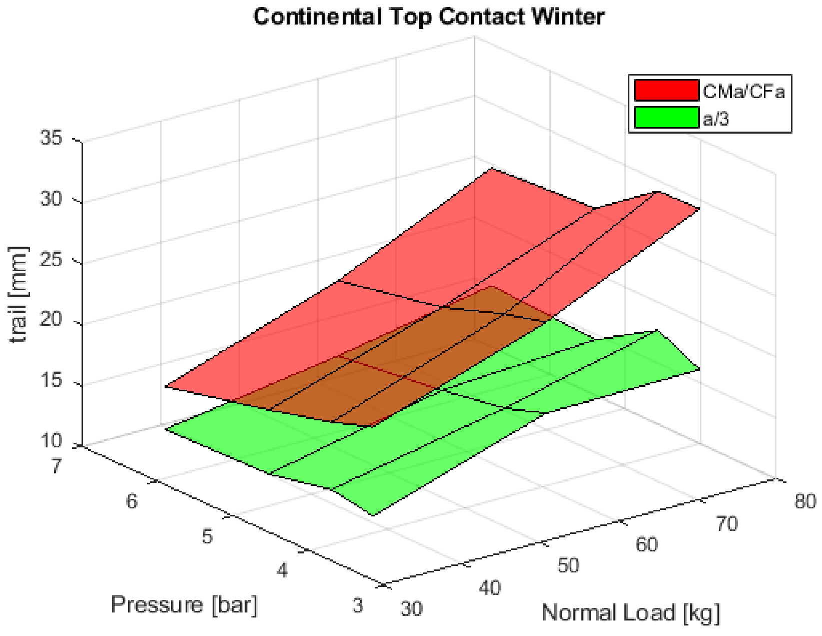

Figure A.7: Trail t for Continental Top Contact Winter.

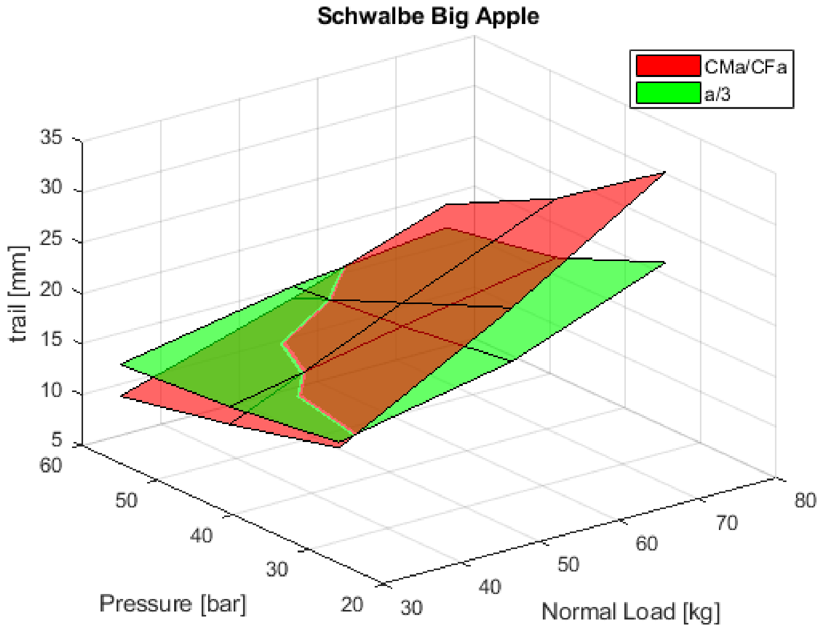

Figure A.8: Trail t for Schwalbe Big Apple.

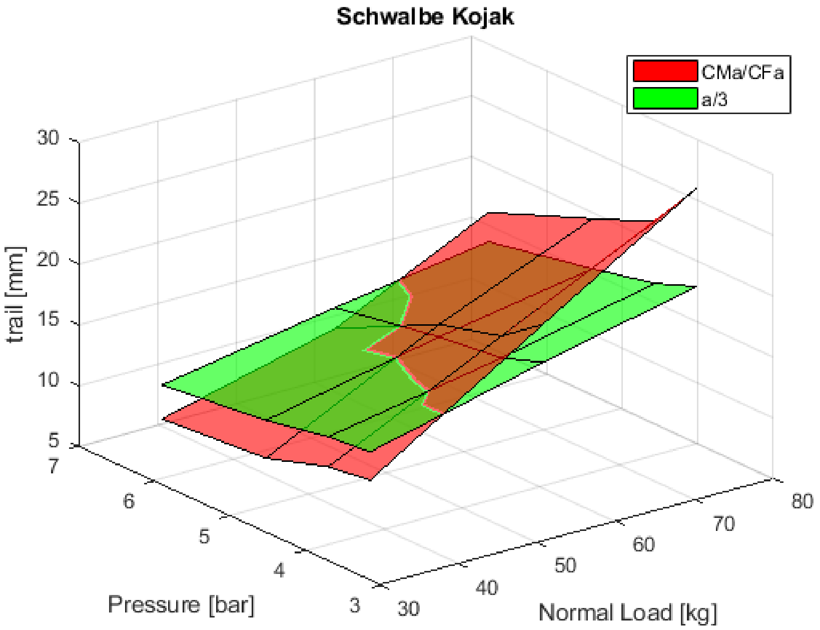

Figure A.9: Trail t for Schwalbe Kojak.

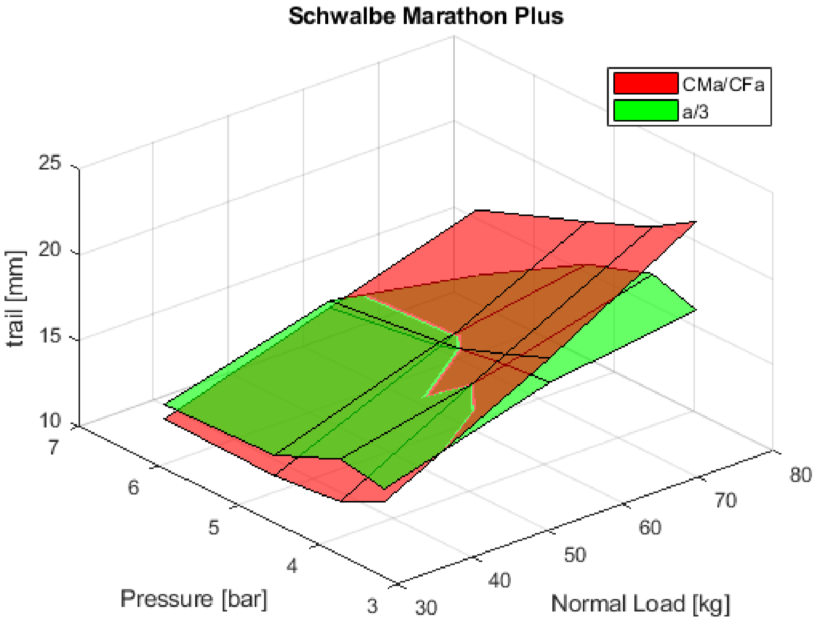

Figure A.10: Trail t for Schwalbe Marathon Plus.

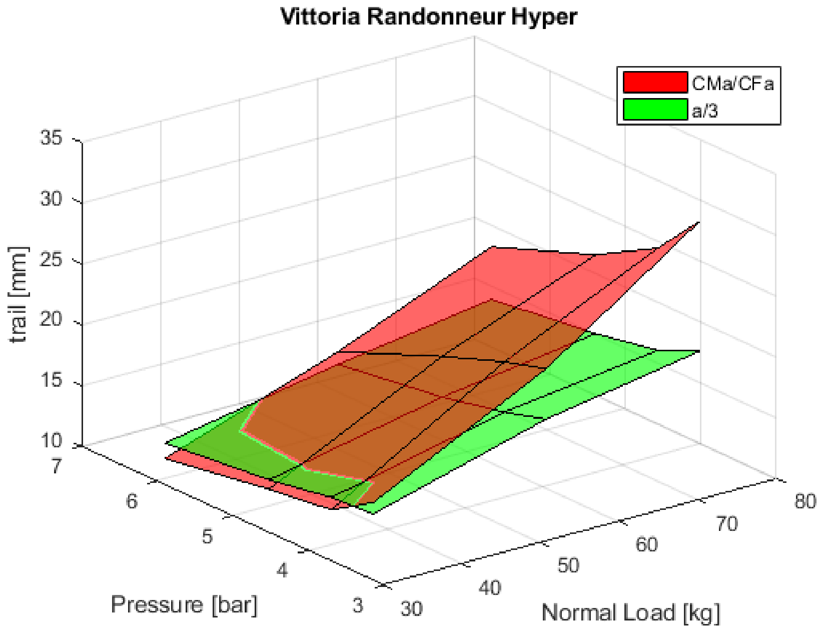

Figure A.11: Trail t for Vittoria Randonneur Hyper.

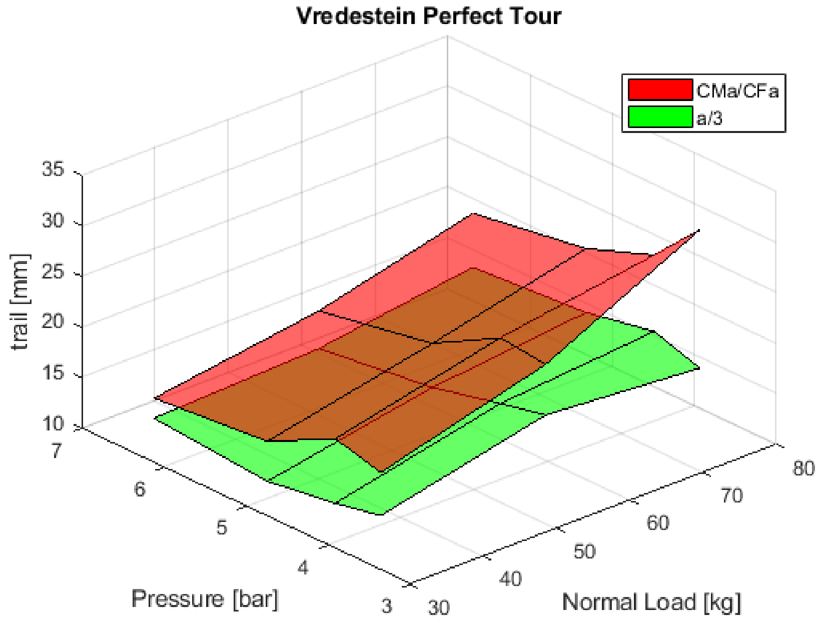

Figure A.12: Trail t for Vredestein Perfect Tour.

B

Results for the enhanced string model

B.1. Vertical direction parameters

Constant normal load

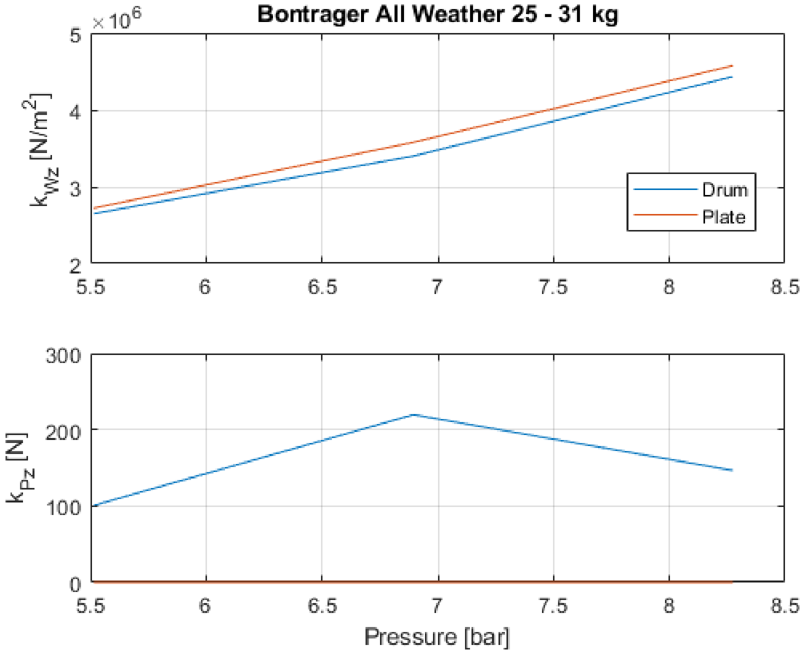

Figure B.1: Results from the parameter optimisation for the Bontrager All Weather 25 at 31 kg.

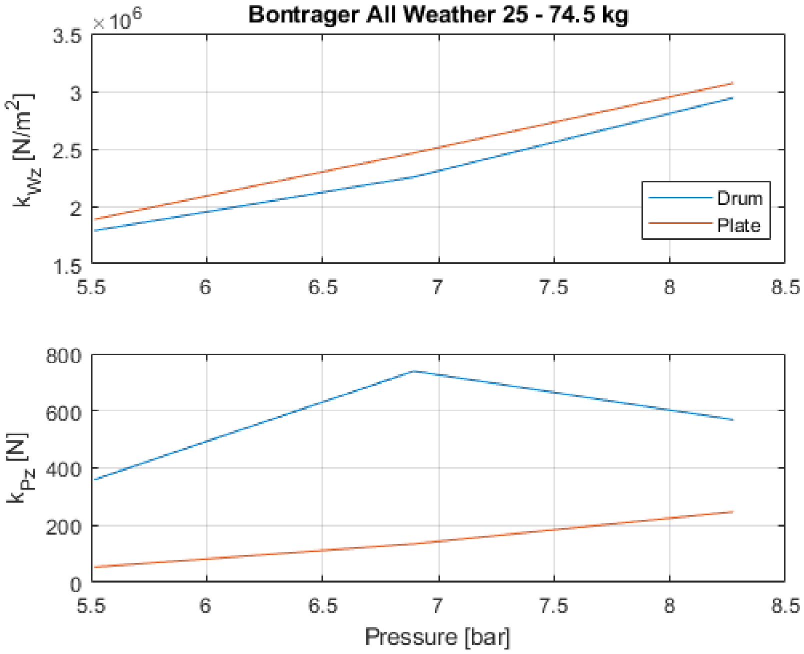

Figure B.2: Results from the parameter optimisation for the Bontrager All Weather 25 at 74.5 kg.

Constant pressure

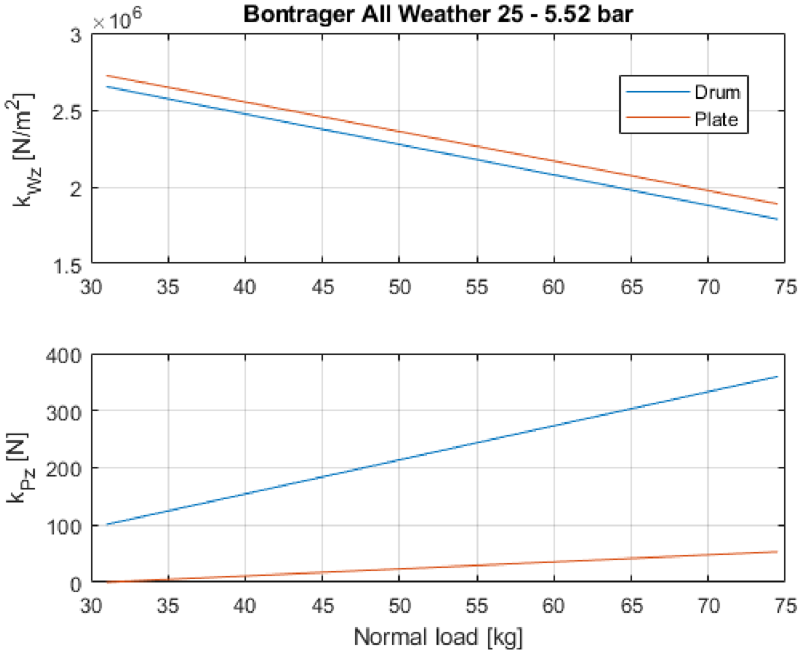

Figure B.3: Results from the parameter optimisation for the Bontrager All Weather 25 at 5.52 bar.

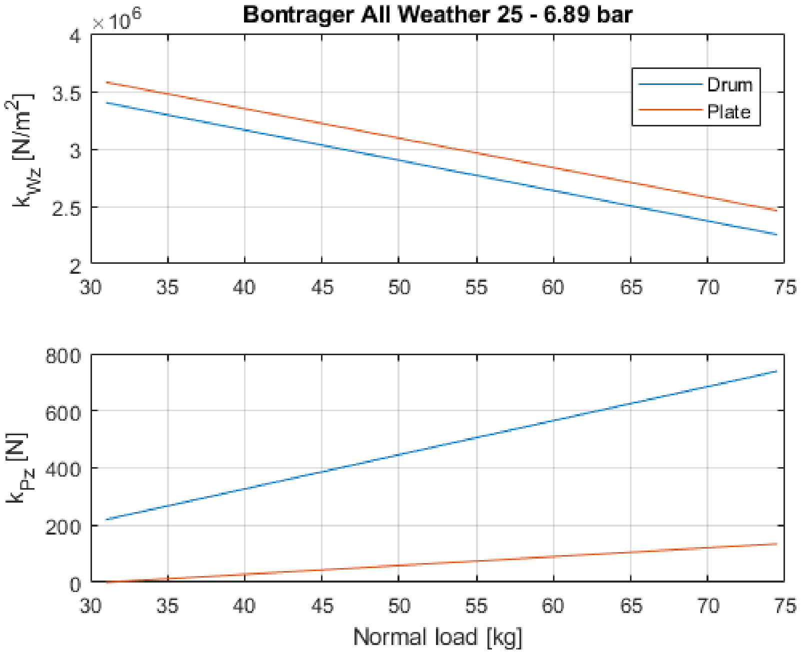

Figure B.4: Results from the parameter optimisation for the Bontrager All Weather 25 at 6.89 bar.

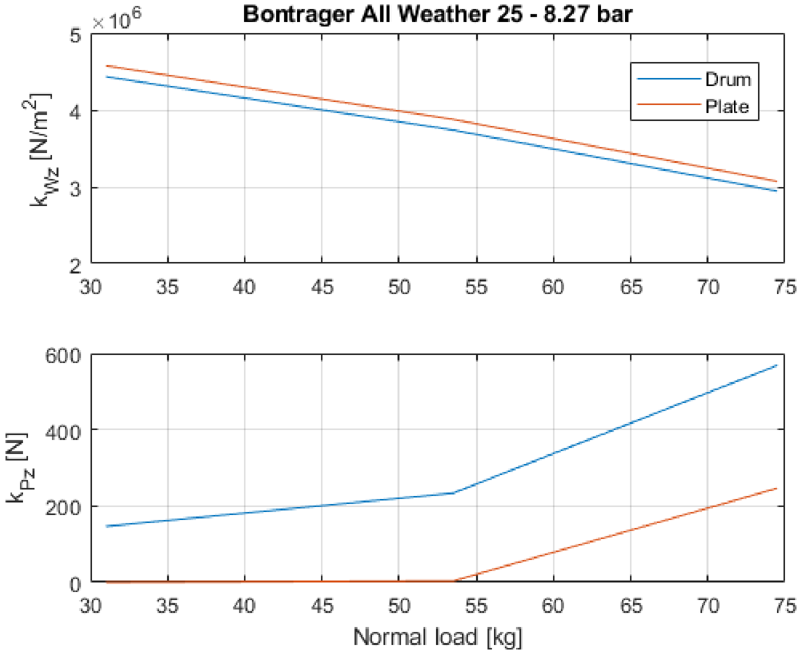

Figure B.5: Results from the parameter optimisation for the Bontrager All Weather 25 at 8.27 bar.

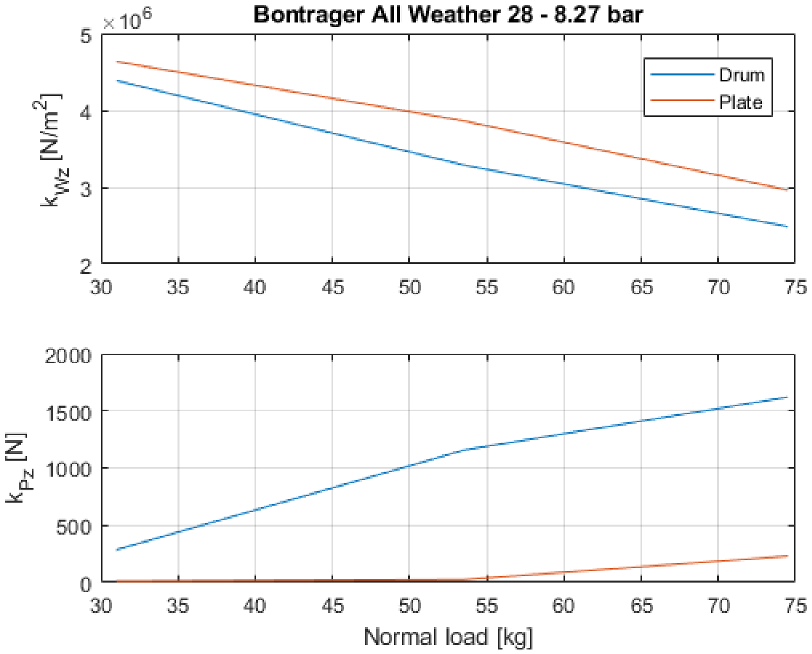

Figure B.6: Results from the parameter optimisation for the Bontrager All Weather 28 at 8.27 bar.

B.2. Lateral direction parameters

Constant normal load

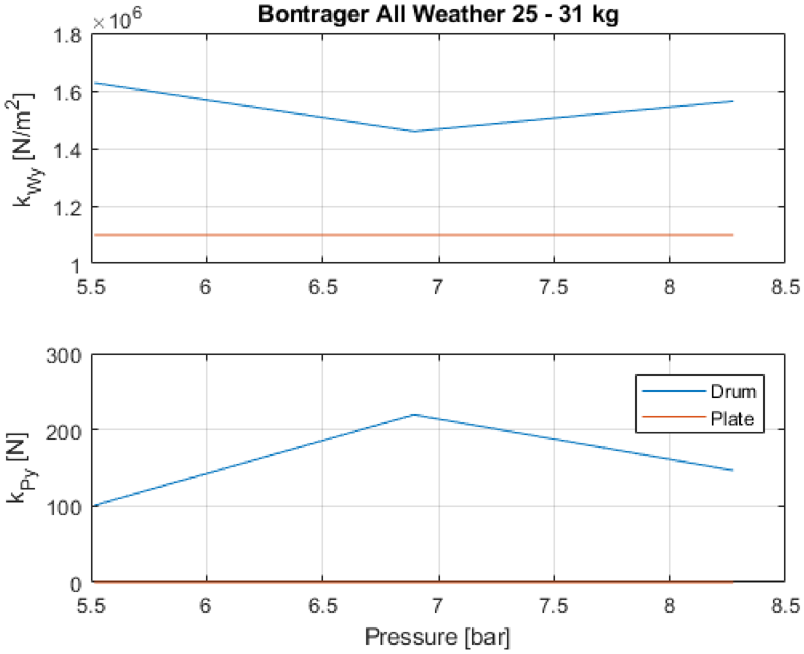

Figure B.7: Results from the parameter optimisation for the Bontrager All Weather 25 at 31 kg.

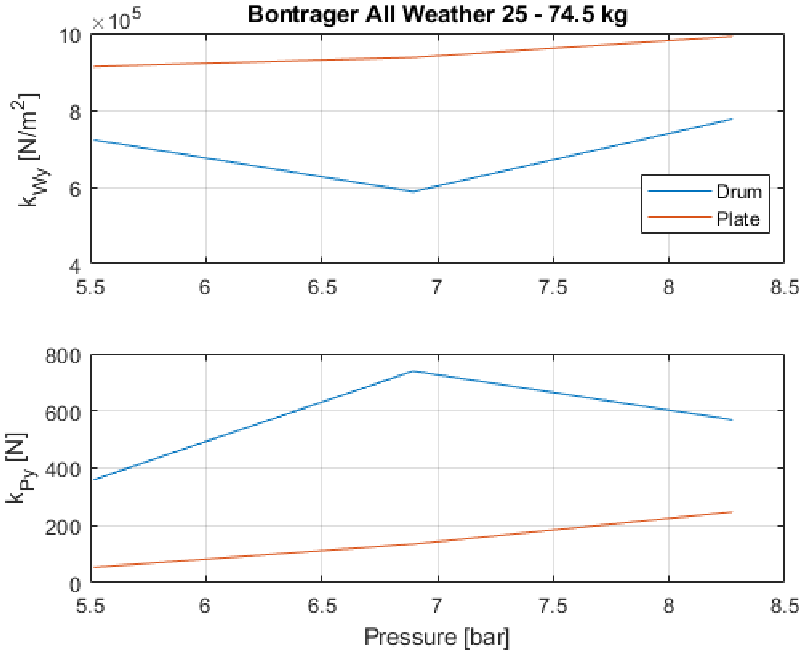

Figure B.8: Results from the parameter optimisation for the Bontrager All Weather 25 at 74.5 kg.

Constant pressure

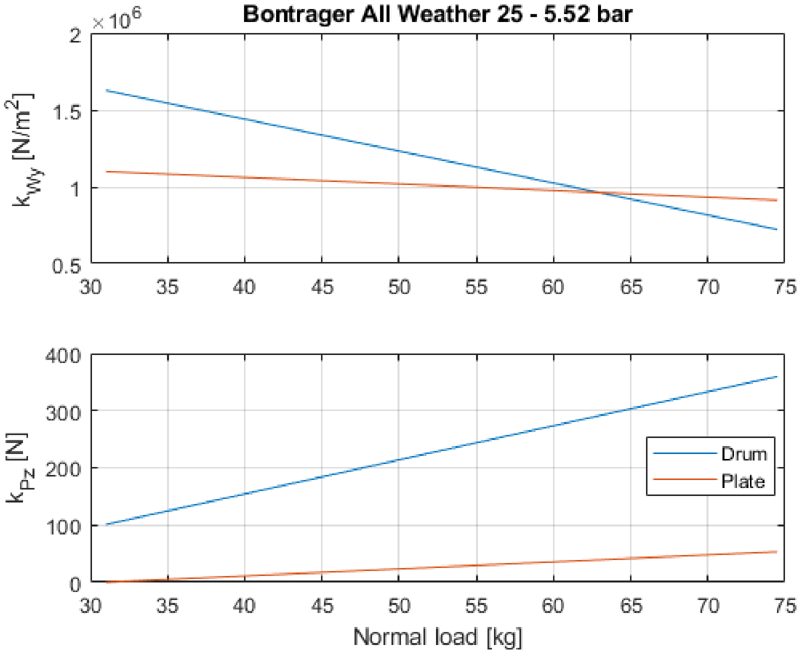

Figure B.9: Results from the parameter optimisation for the Bontrager All Weather 25 at 5.52 bar.

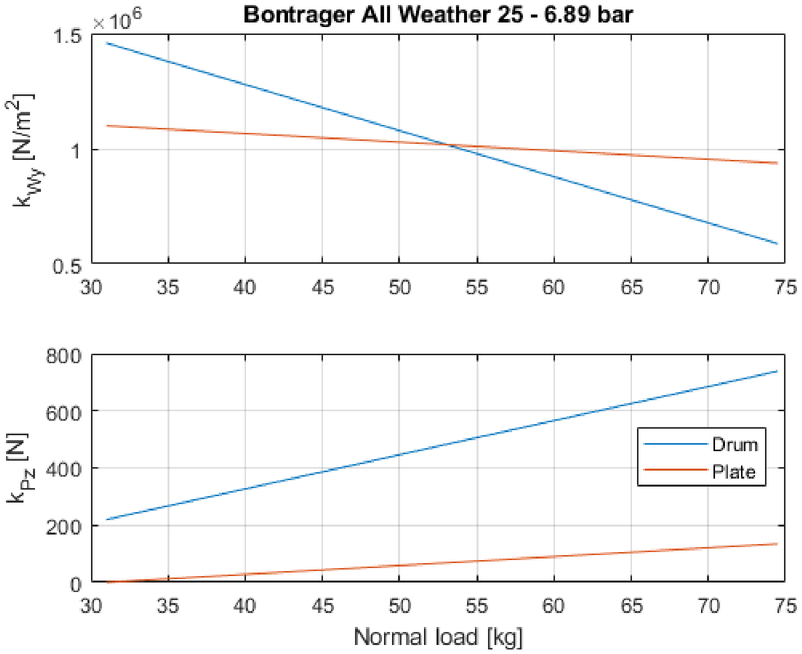

Figure B.10: Results from the parameter optimisation for the Bontrager All Weather 25 at 6.89 bar.

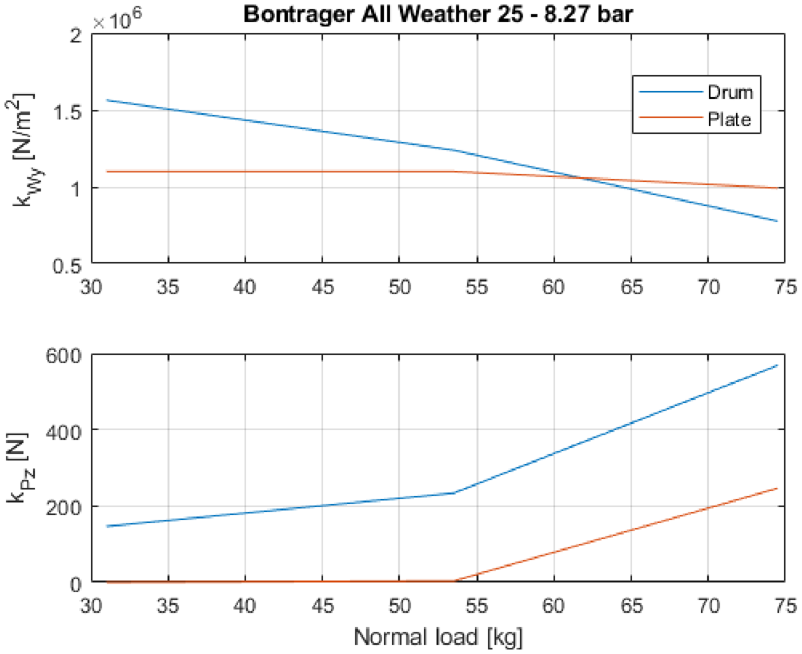

Figure B.11: Results from the parameter optimisation for the Bontrager All Weather 25 at 8.27 bar.

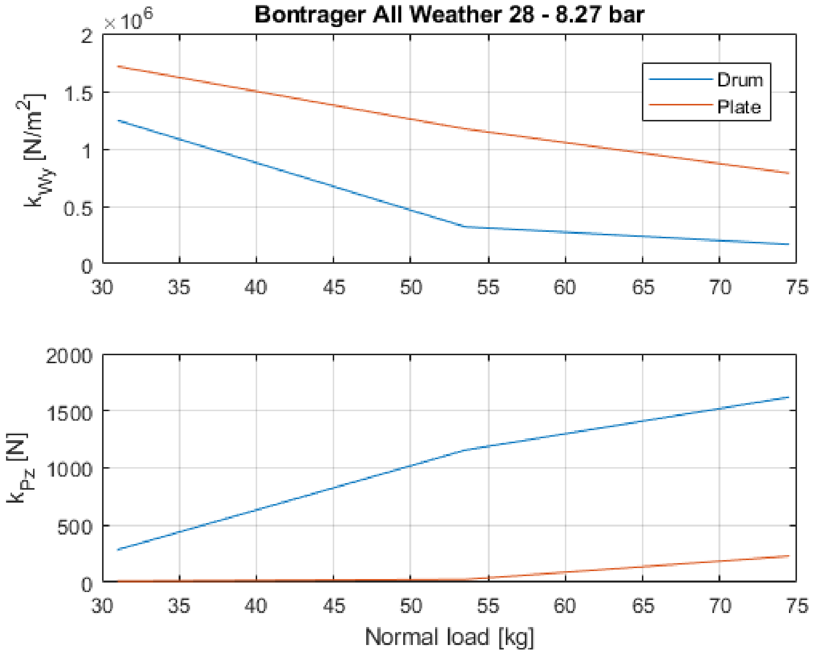

Figure B.12: Results from the parameter optimisation for the Bontrager All Weather 28 at 8.27 bar.

B.3. Individual tyre measurements compared with model output

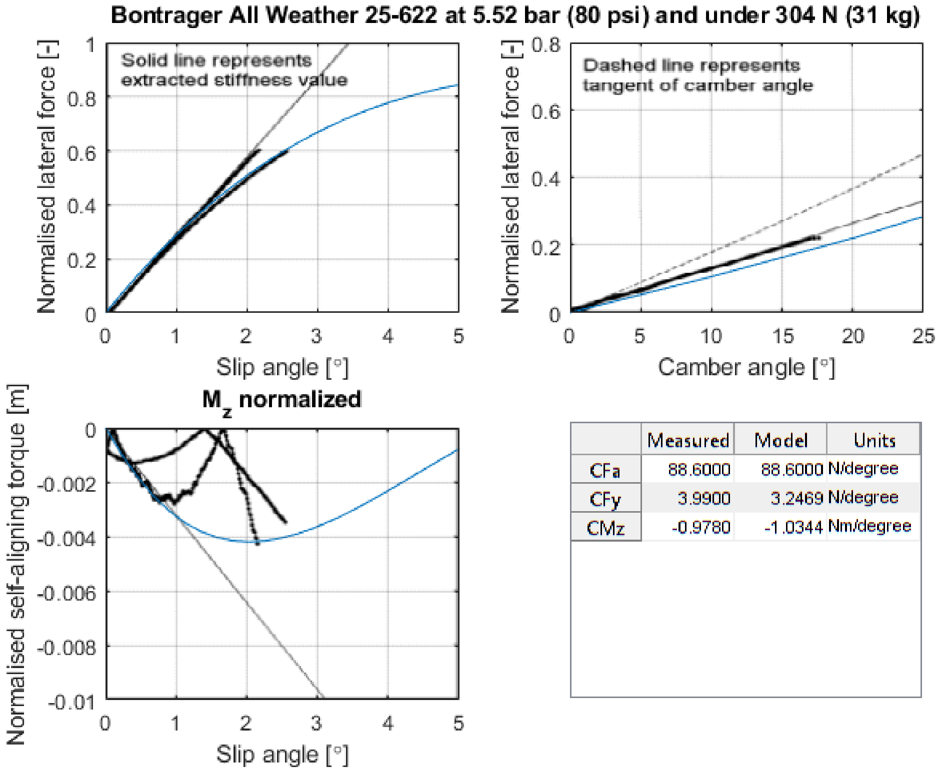

	Measured	Model	Units
CFa	88.6000	88.6000	N/degree
CFy	3.9900	3.2469	N/degree
CMz	-0.9780	-1.0344	Nm/degree

Figure B.13

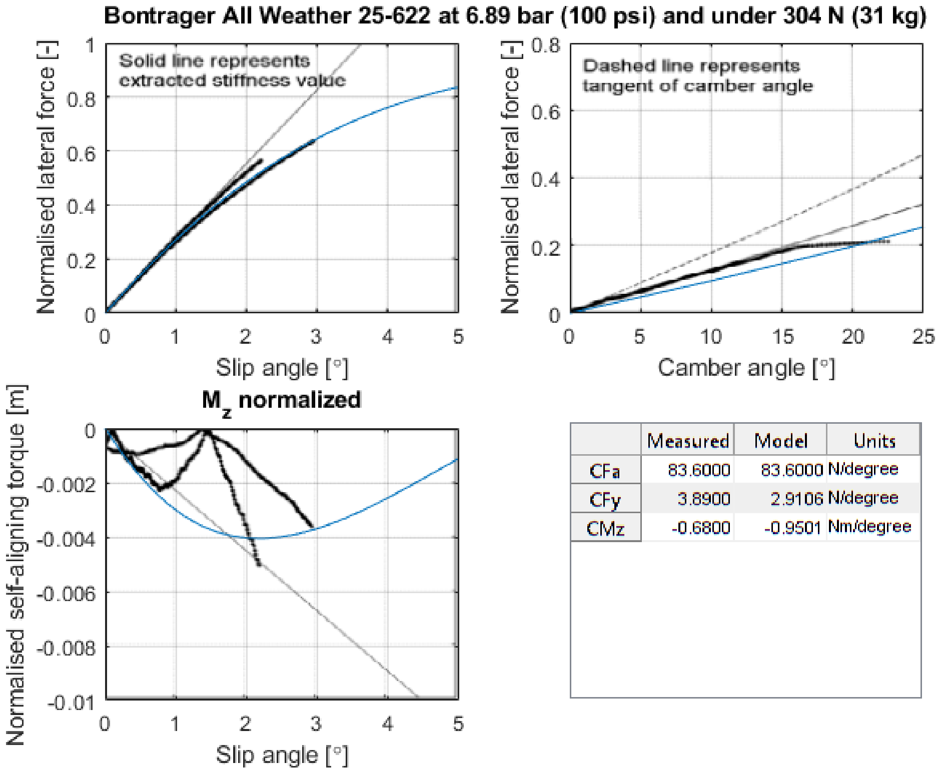

	Measured	Model	Units
CFa	83.6000	83.6000	N/degree
CFy	3.8900	2.9106	N/degree
CMz	-0.6800	-0.9501	Nm/degree

Figure B.14

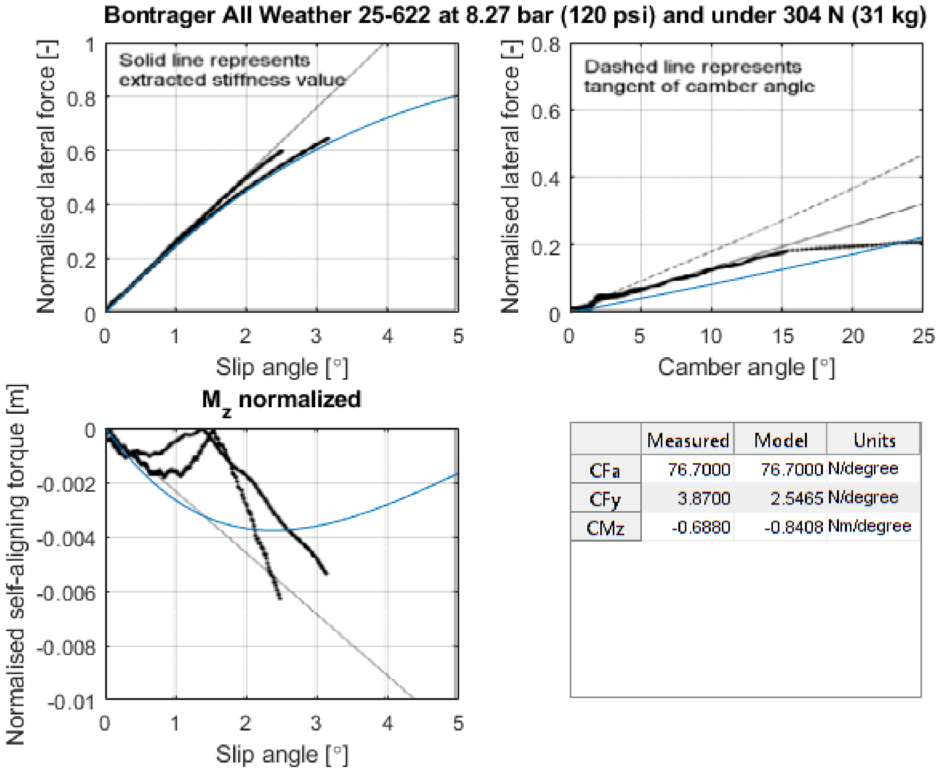

	Measured	Model	Units
CFa	76.7000	76.7000	N/degree
CFy	3.8700	2.5465	N/degree
CMz	-0.6880	-0.8408	Nm/degree

Figure B.15

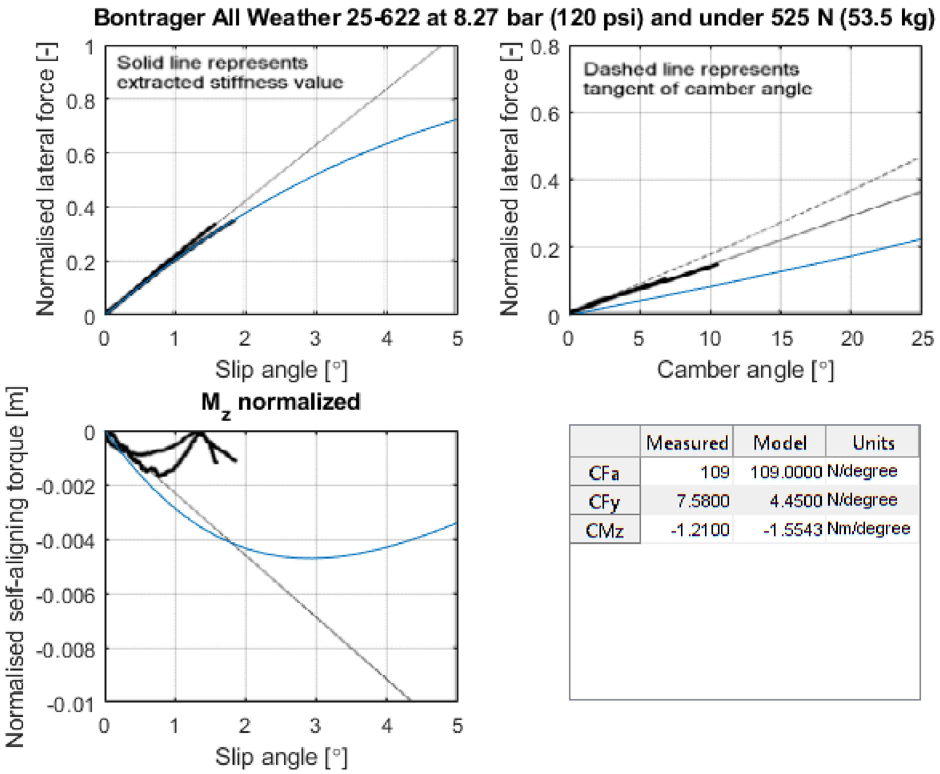

	Measured	Model	Units
CFa	109	109.0000	N/degree
CFy	7.5800	4.4500	N/degree
CMz	-1.2100	-1.5543	Nm/degree

Figure B.16

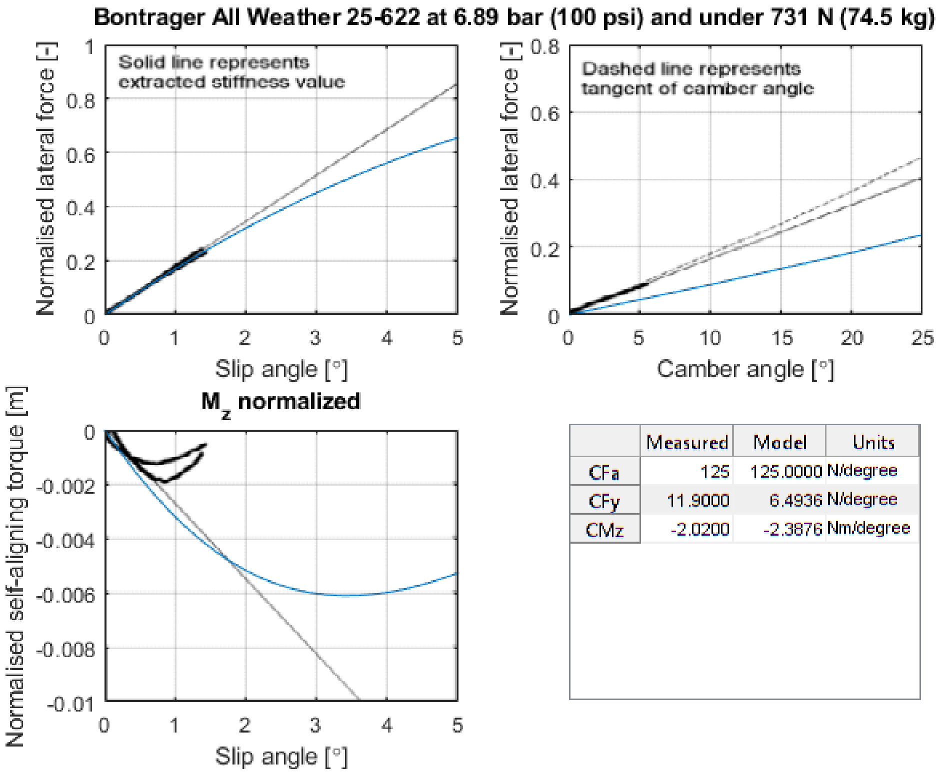

	Measured	Model	Units
CFa	125	125.0000	N/degree
CFy	11.9000	6.4936	N/degree
CMz	-2.0200	-2.3876	Nm/degree

Figure B.17

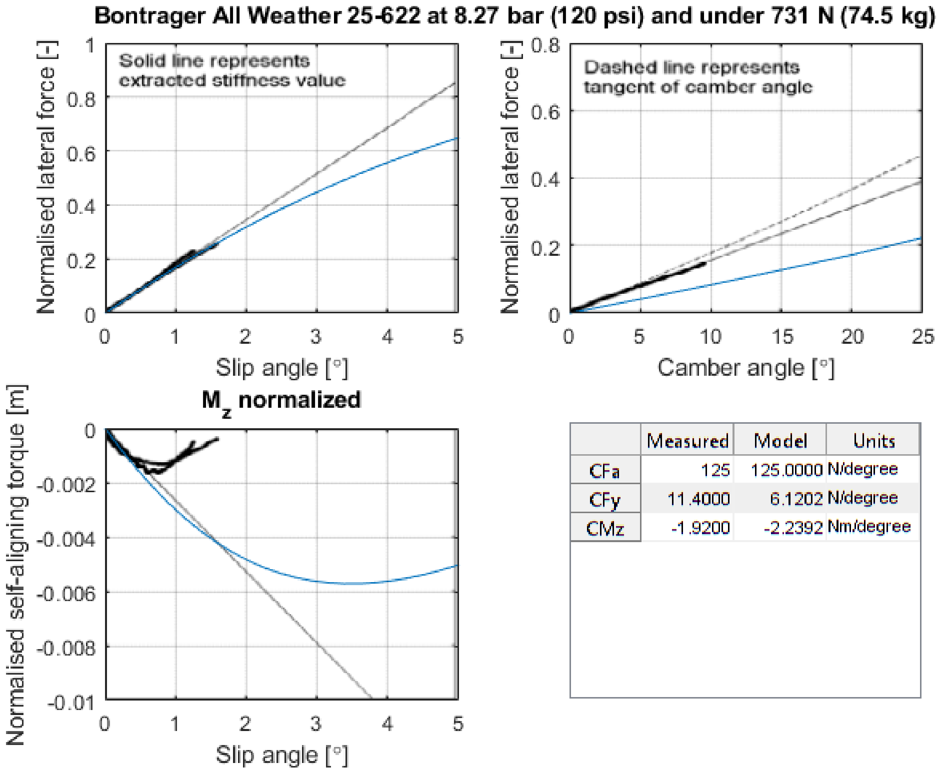

	Measured	Model	Units
CFa	125	125.0000	N/degree
CFy	11.4000	6.1202	N/degree
CMz	-1.9200	-2.2392	Nm/degree

Figure B.18

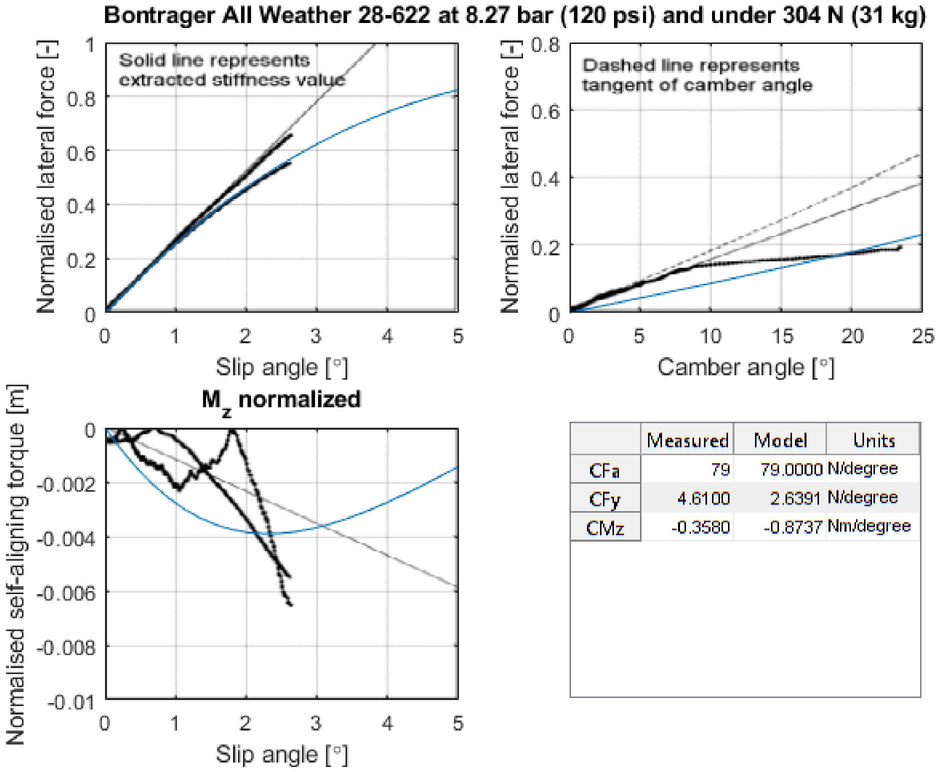

	Measured	Model	Units
CFa	79	79.0000	N/degree
CFy	4.6100	2.6391	N/degree
CMz	-0.3580	-0.8737	Nm/degree

Figure B.19

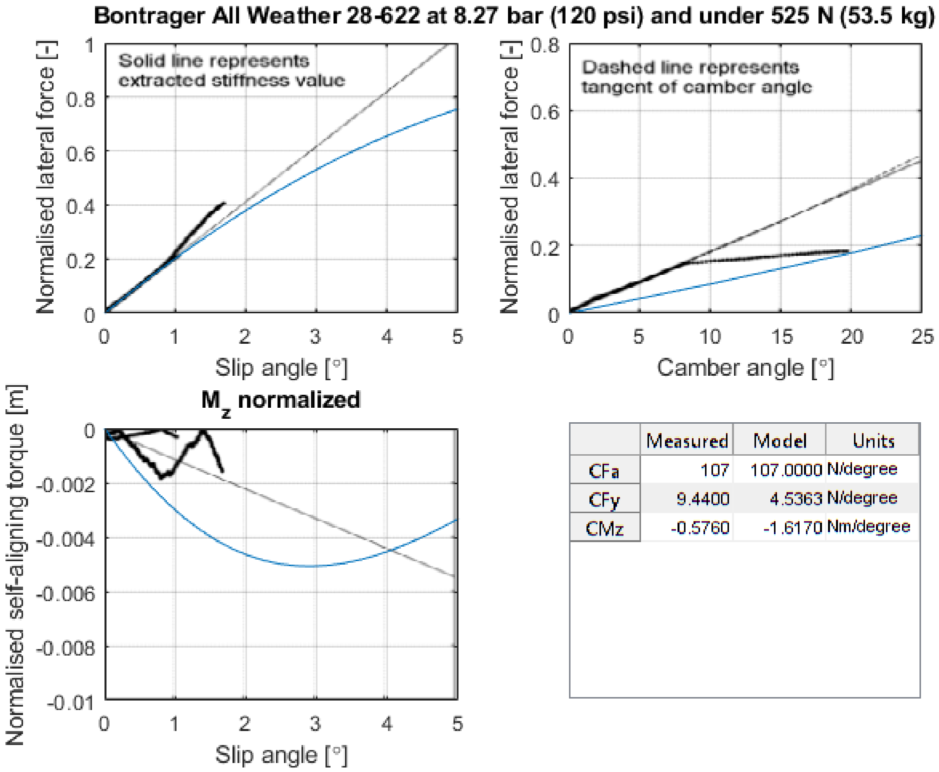

	Measured	Model	Units
CFa	107	107.0000	N/degree
CFy	9.4400	4.5363	N/degree
CMz	-0.5760	-1.6170	Nm/degree

Figure B.20

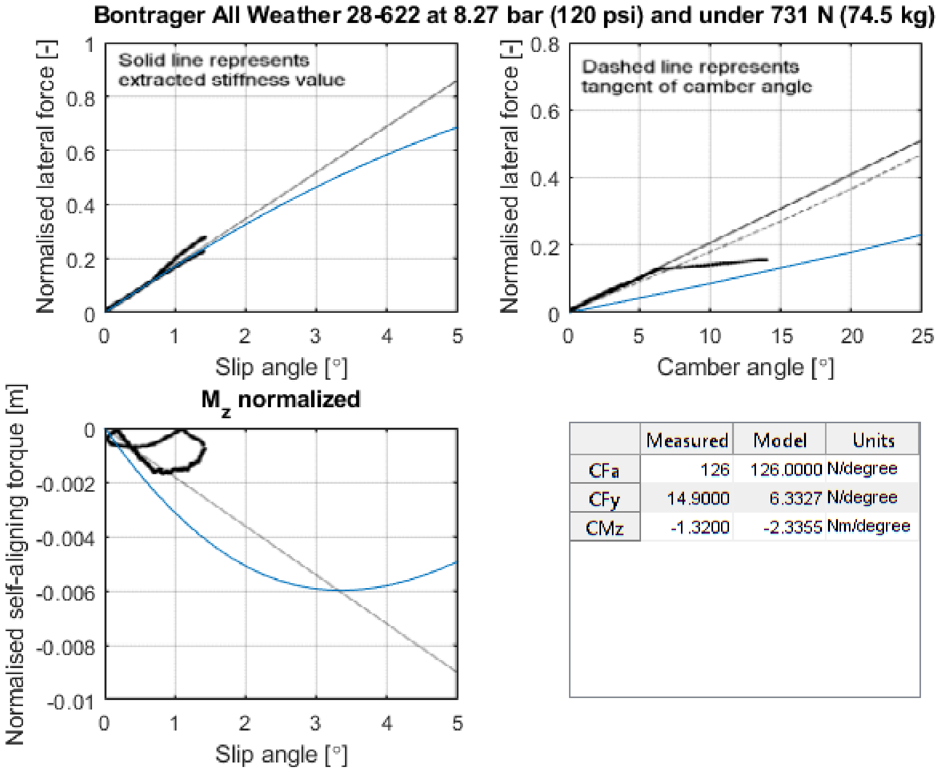

	Measured	Model	Units
CFa	126	126.0000	N/degree
CFy	14.9000	6.3327	N/degree
CMz	-1.3200	-2.3355	Nm/degree

Figure B.21

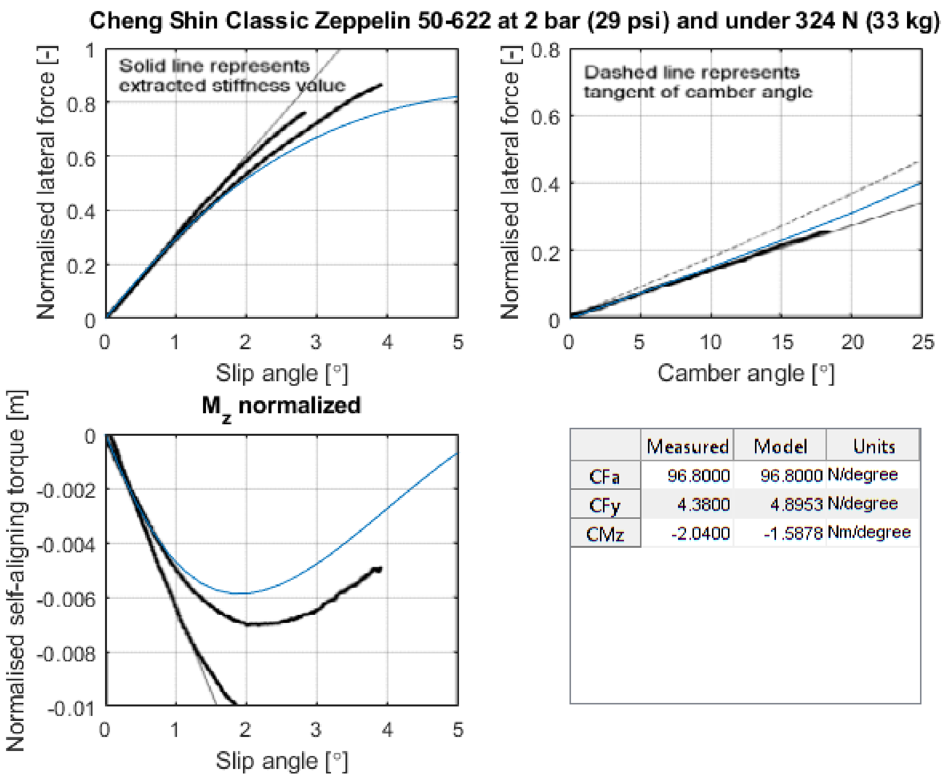

	Measured	Model	Units
CFa	96.8000	96.8000	N/degree
CFy	4.3800	4.8953	N/degree
CMz	-2.0400	-1.5878	Nm/degree

Figure B.22

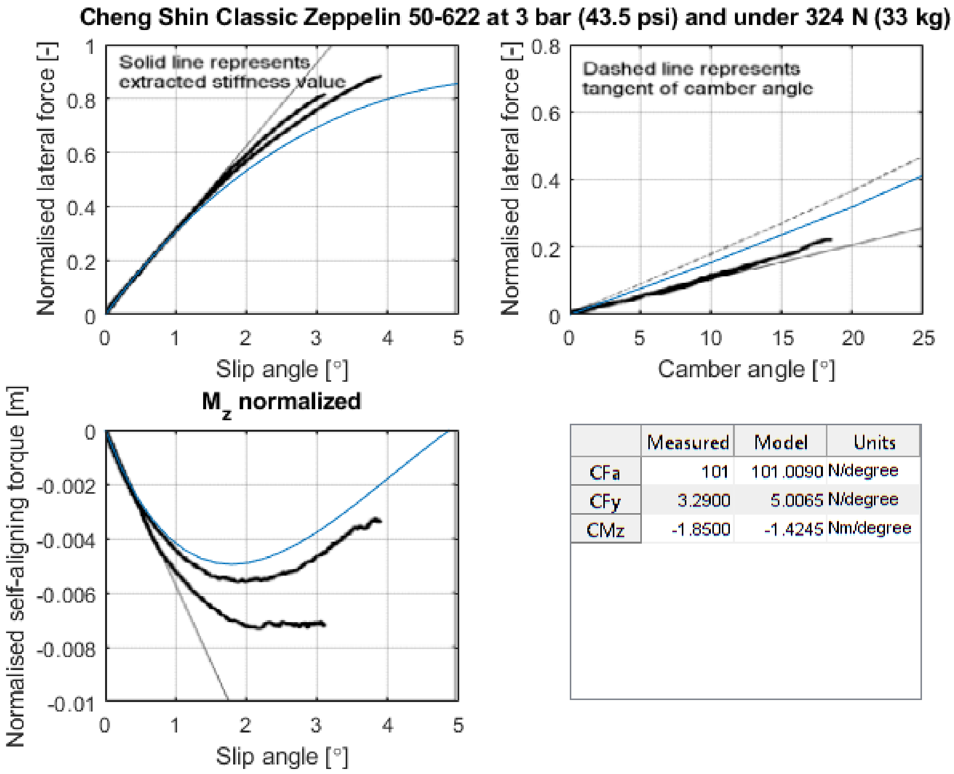

	Measured	Model	Units
CFa	101	101.0090	N/degree
CFy	3.2900	5.0065	N/degree
CMz	-1.8500	-1.4245	Nm/degree

Figure B.23

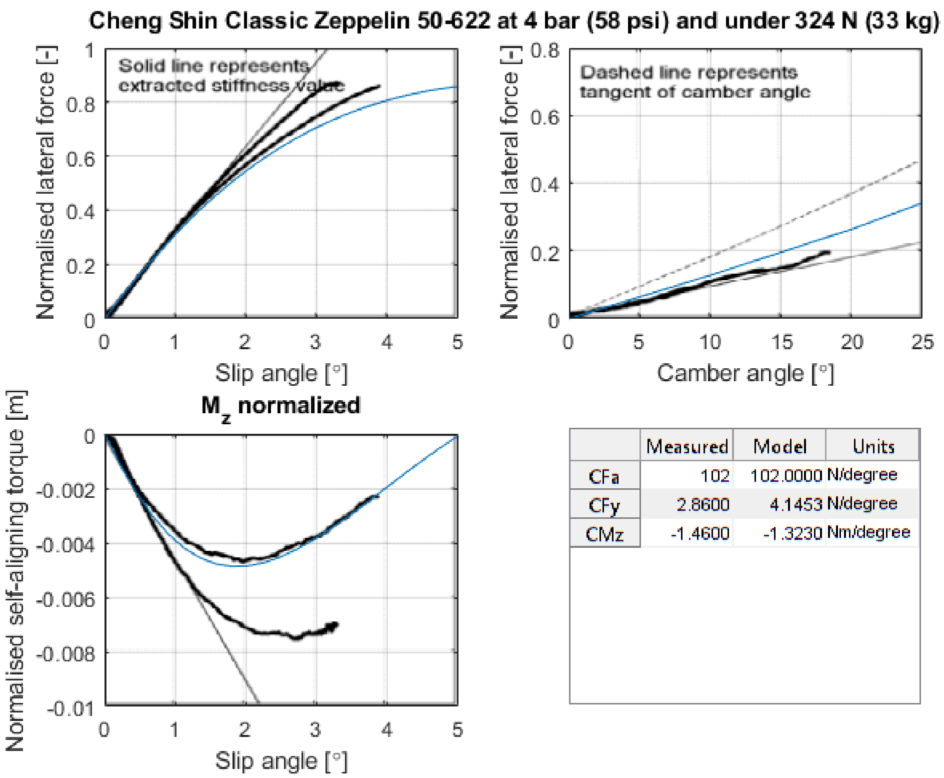

	Measured	Model	Units
CFa	102	102.0000	N/degree
CFy	2.8600	4.1453	N/degree
CMz	-1.4600	-1.3230	Nm/degree

Figure B.24

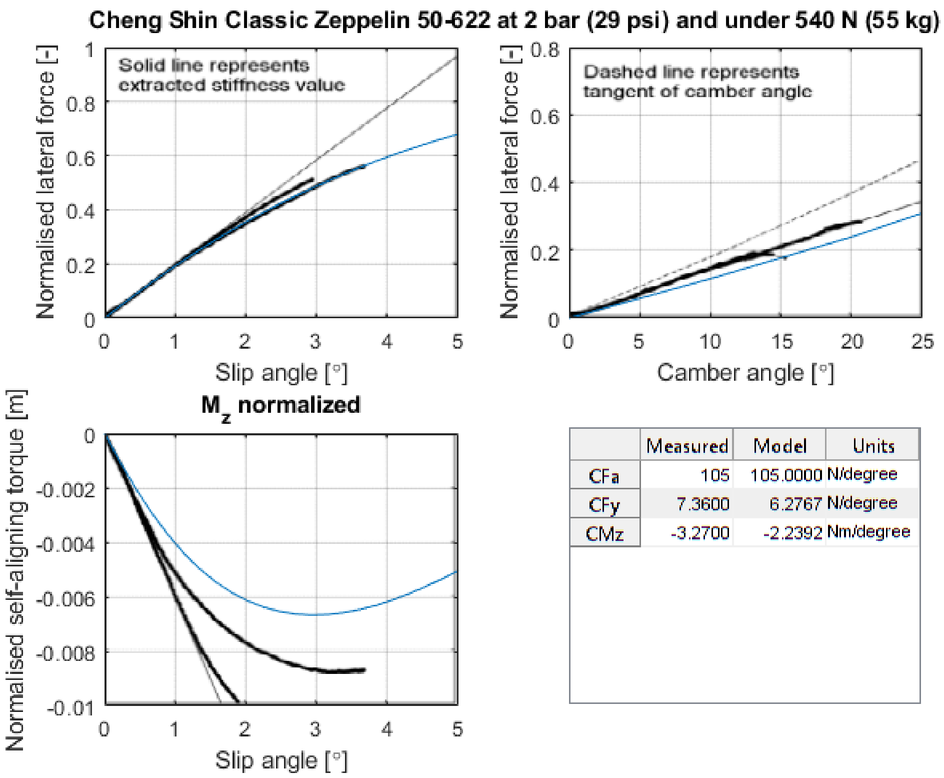

	Measured	Model	Units
CFa	105	105.0000	N/degree
CFy	7.3600	6.2767	N/degree
CMz	-3.2700	-2.2392	Nm/degree

Figure B.25

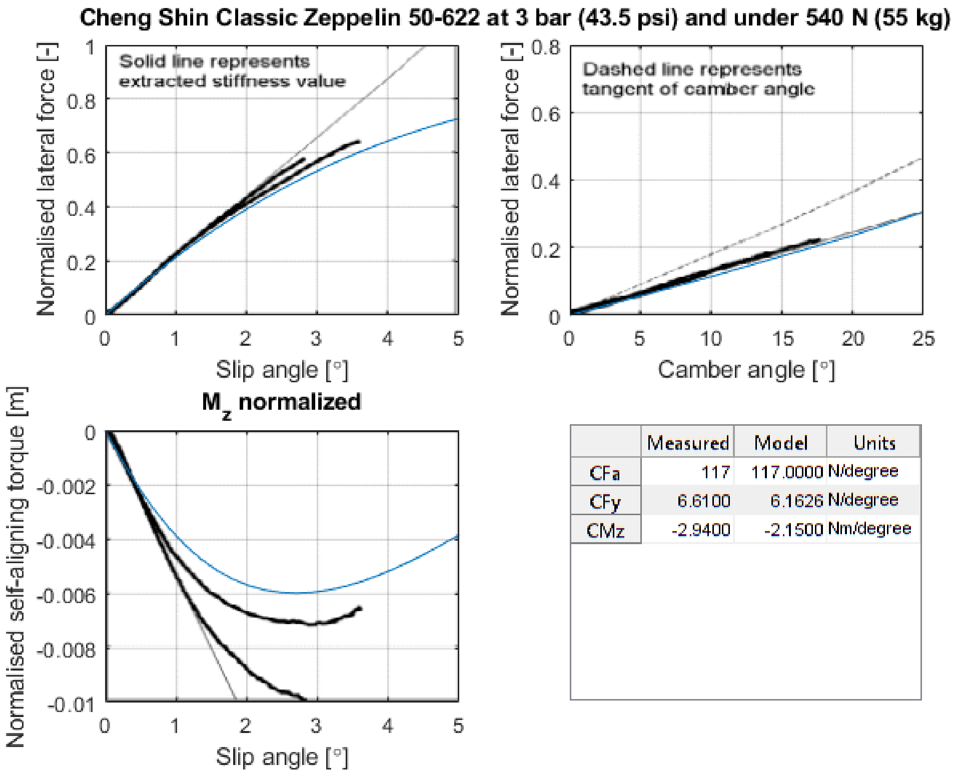

	Measured	Model	Units
CFa	117	117.0000	N/degree
CFy	6.6100	6.1626	N/degree
CMz	-2.9400	-2.1500	Nm/degree

Figure B.26

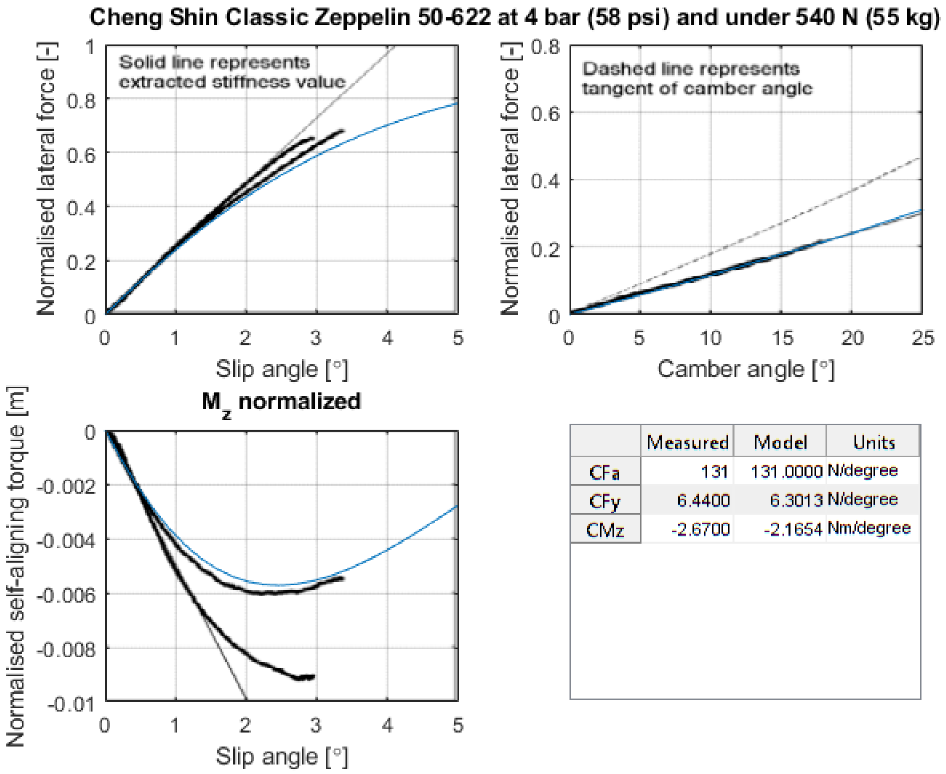

	Measured	Model	Units
CFa	131	131.0000	N/degree
CFy	6.4400	6.3013	N/degree
CMz	-2.6700	-2.1654	Nm/degree

Figure B.27

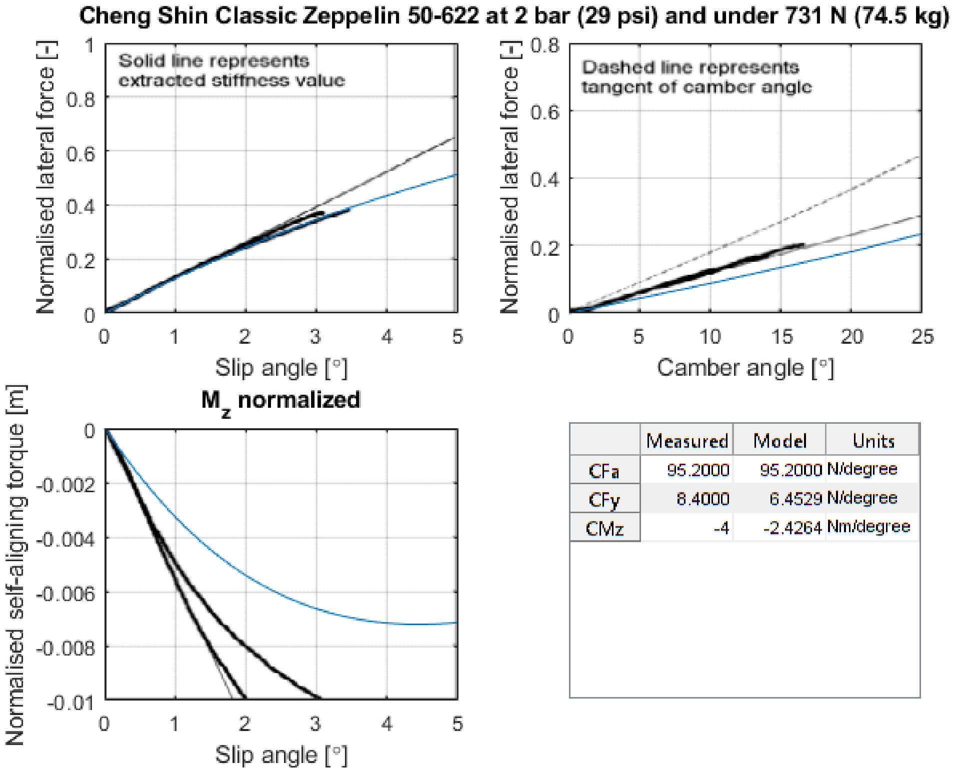

Cheng Shin Classic Zeppelin 50-622 at 2 bar (29 psi) and under 731 N (74.5 kg)

	Measured	Model	Units
CFa	95.2000	95.2000	N/degree
CFy	8.4000	6.4529	N/degree
CMz	-4	-2.4264	Nm/degree

Figure B.28

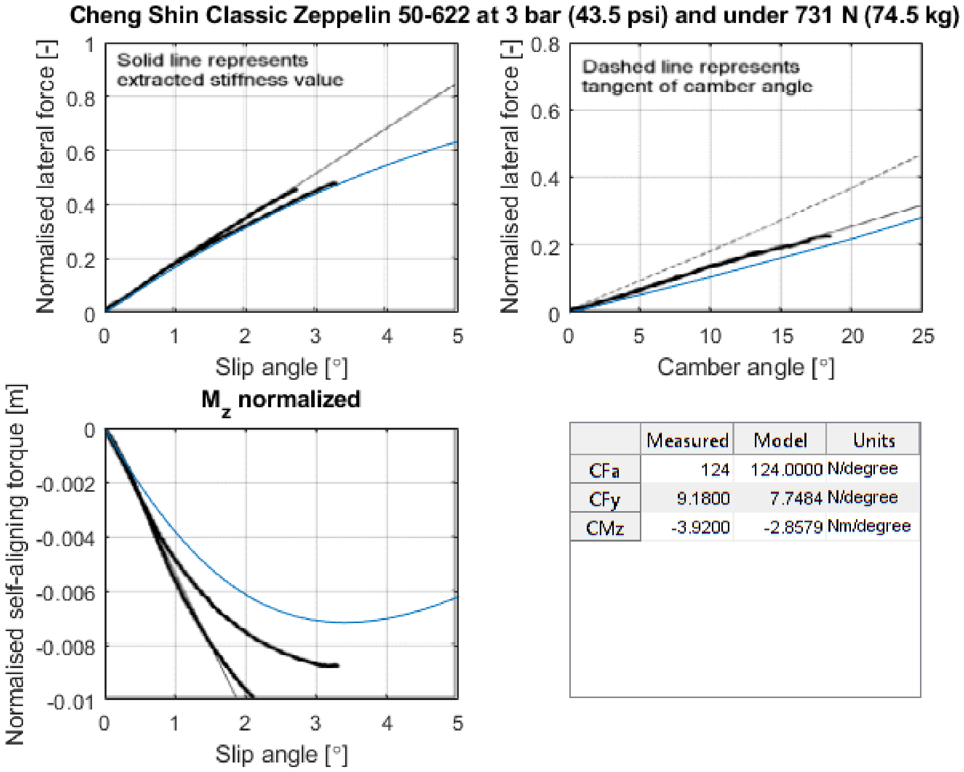

Cheng Shin Classic Zeppelin 50-622 at 3 bar (43.5 psi) and under 731 N (74.5 kg)

	Measured	Model	Units
CFa	124	124.0000	N/degree
CFy	9.1800	7.7484	N/degree
CMz	-3.9200	-2.8579	Nm/degree

Figure B.29

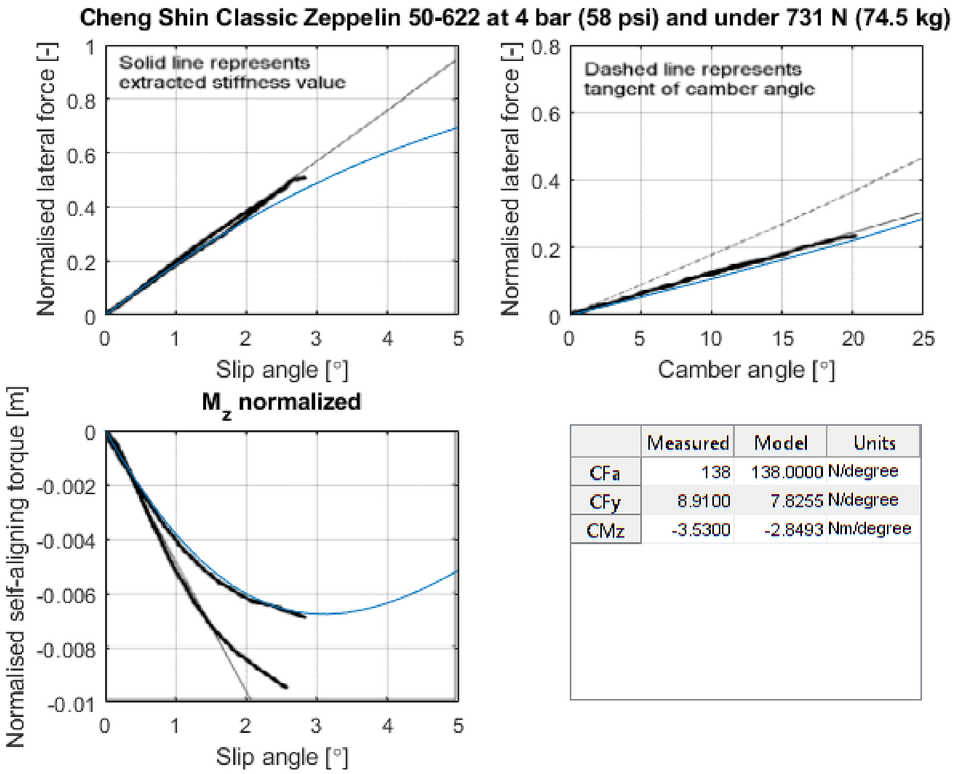

Cheng Shin Classic Zeppelin 50-622 at 4 bar (58 psi) and under 731 N (74.5 kg)

	Measured	Model	Units
CFa	138	138.0000	N/degree
CFy	8.9100	7.8255	N/degree
CMz	-3.5300	-2.8493	Nm/degree

Figure B.30

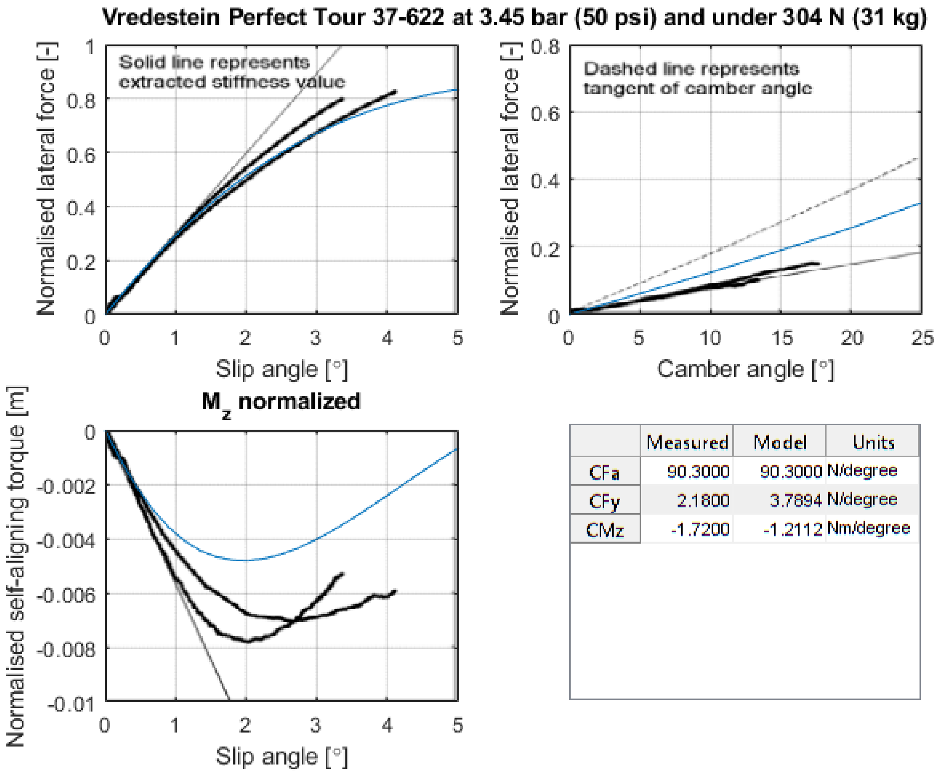

Vredestein Perfect Tour 37-622 at 3.45 bar (50 psi) and under 304 N (31 kg)

	Measured	Model	Units
CFa	90.3000	90.3000	N/degree
CFy	2.1800	3.7894	N/degree
CMz	-1.7200	-1.2112	Nm/degree

Figure B.31

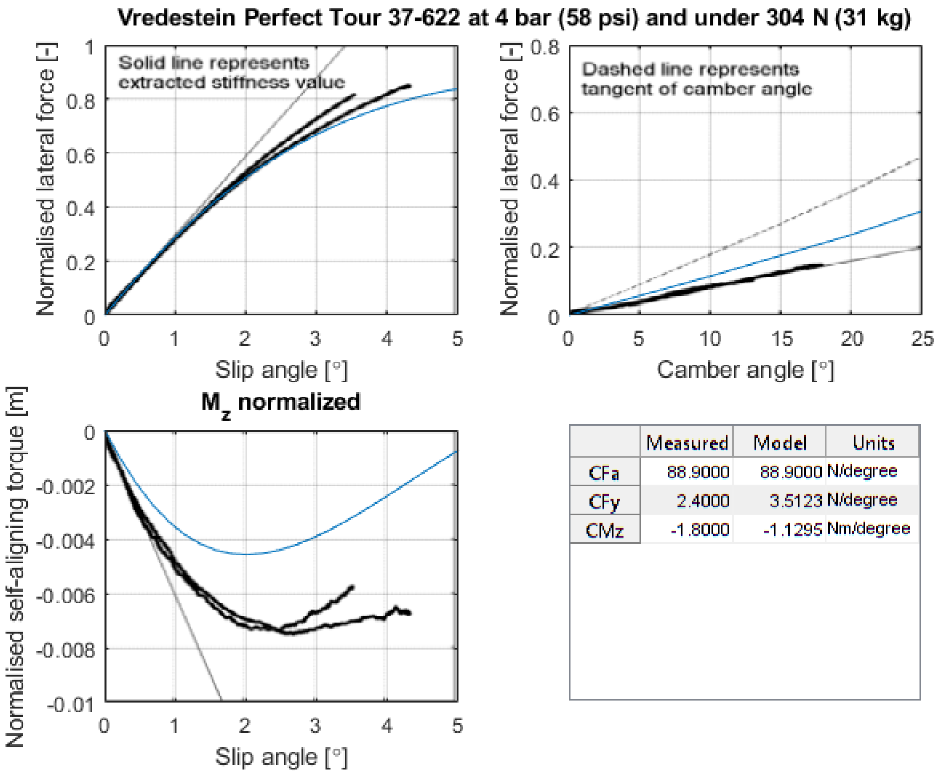

	Measured	Model	Units
CFa	88.9000	88.9000	N/degree
CFy	2.4000	3.5123	N/degree
CMz	-1.8000	-1.1295	Nm/degree

Figure B.32

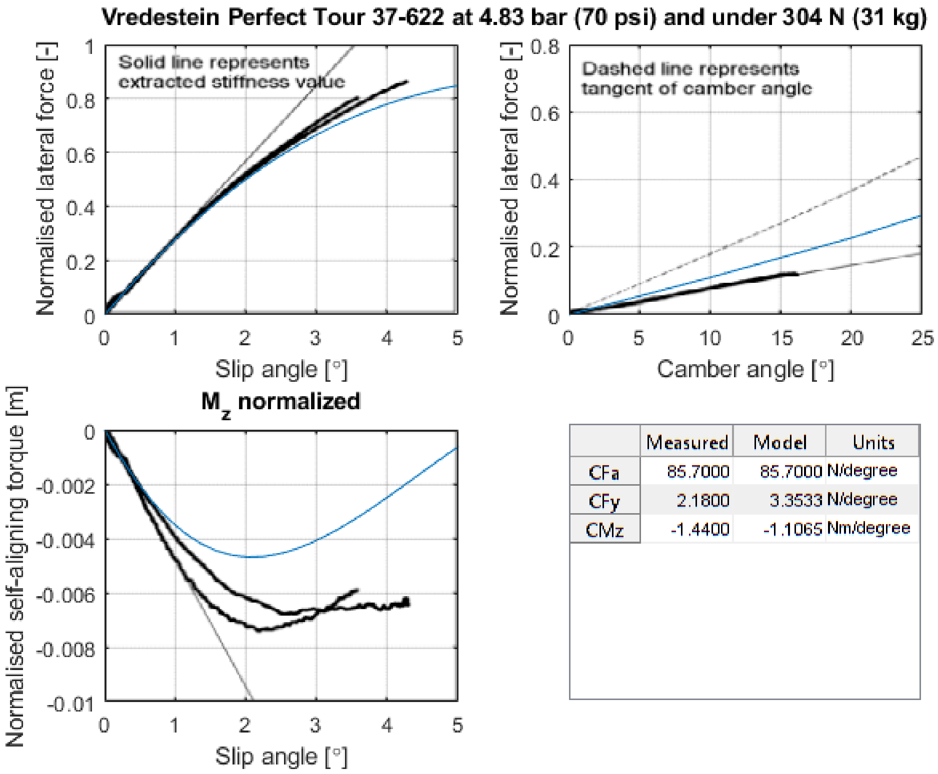

	Measured	Model	Units
CFa	85.7000	85.7000	N/degree
CFy	2.1800	3.3533	N/degree
CMz	-1.4400	-1.1065	Nm/degree

Figure B.33

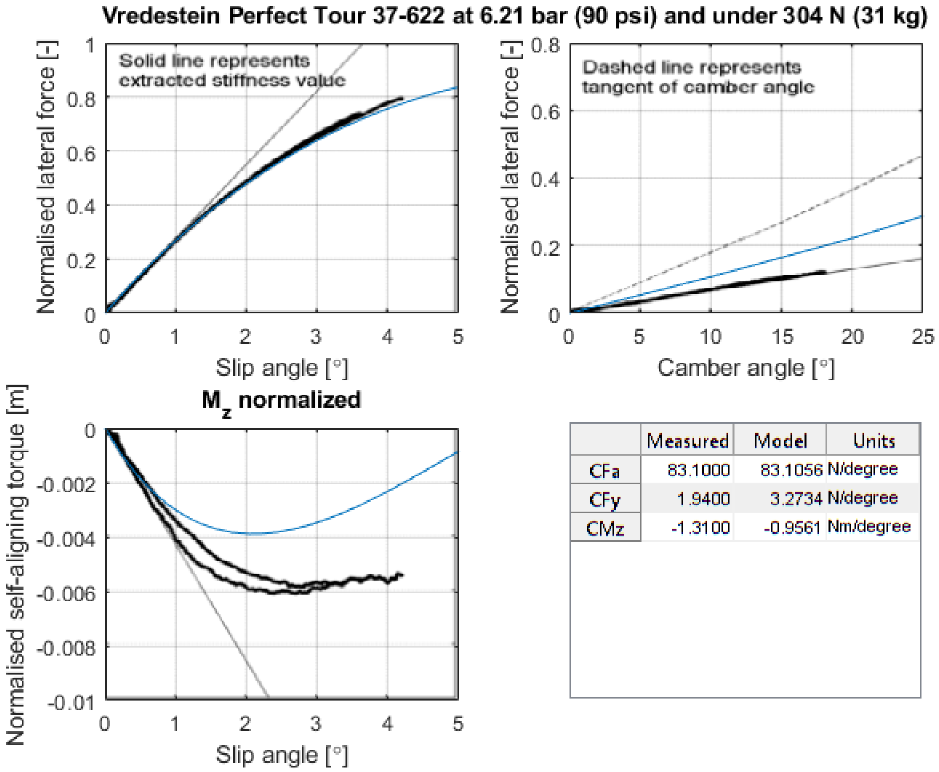

	Measured	Model	Units
CFa	83.1000	83.1056	N/degree
CFy	1.9400	3.2734	N/degree
CMz	-1.3100	-0.9561	Nm/degree

Figure B.34

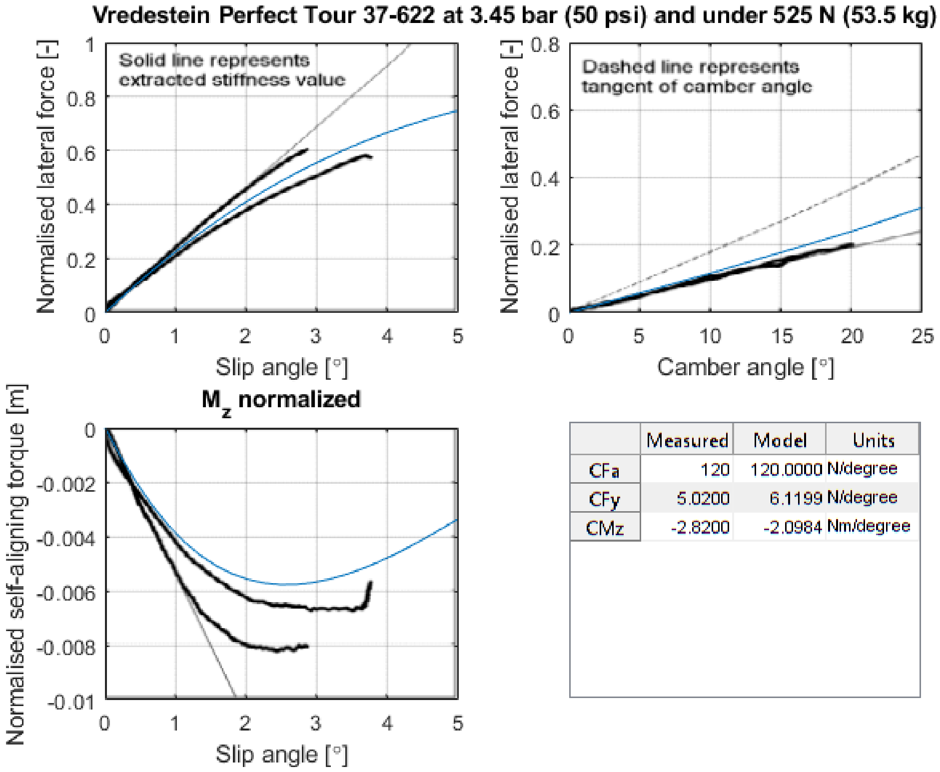

	Measured	Model	Units
CFa	120	120.0000	N/degree
CFy	5.0200	6.1199	N/degree
CMz	-2.8200	-2.0984	Nm/degree

Figure B.35

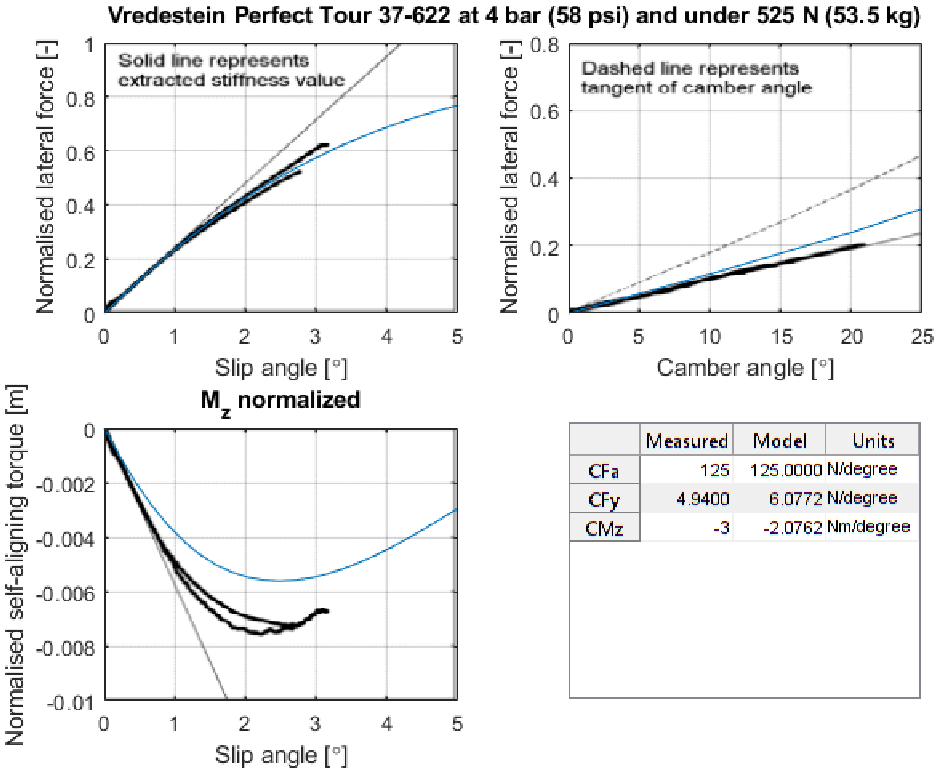

	Measured	Model	Units
CFa	125	125.0000	N/degree
CFy	4.9400	6.0772	N/degree
CMz	-3	-2.0762	Nm/degree

Figure B.36

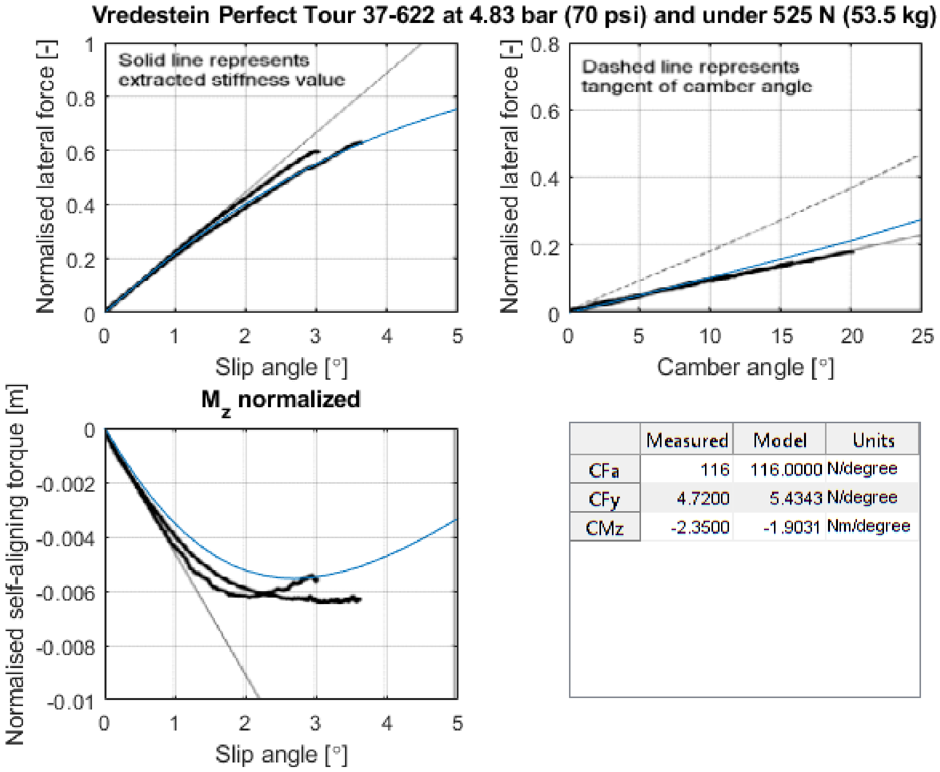

	Measured	Model	Units
CFa	116	116.0000	N/degree
CFy	4.7200	5.4343	N/degree
CMz	-2.3500	-1.9031	Nm/degree

Figure B.37

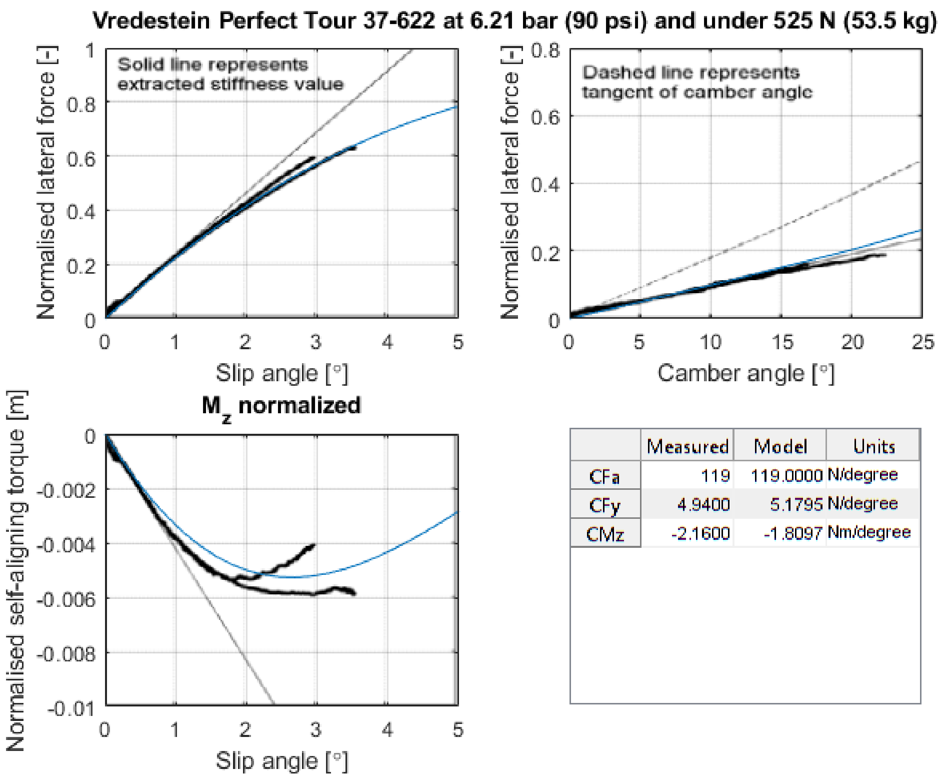
Vredestein Perfect Tour 37-622 at 6.21 bar (90 psi) and under 525 N (53.5 kg)

	Measured	Model	Units
CFa	119	119.0000	N/degree
CFy	4.9400	5.1795	N/degree
CMz	-2.1600	-1.8097	Nm/degree

Figure B.38

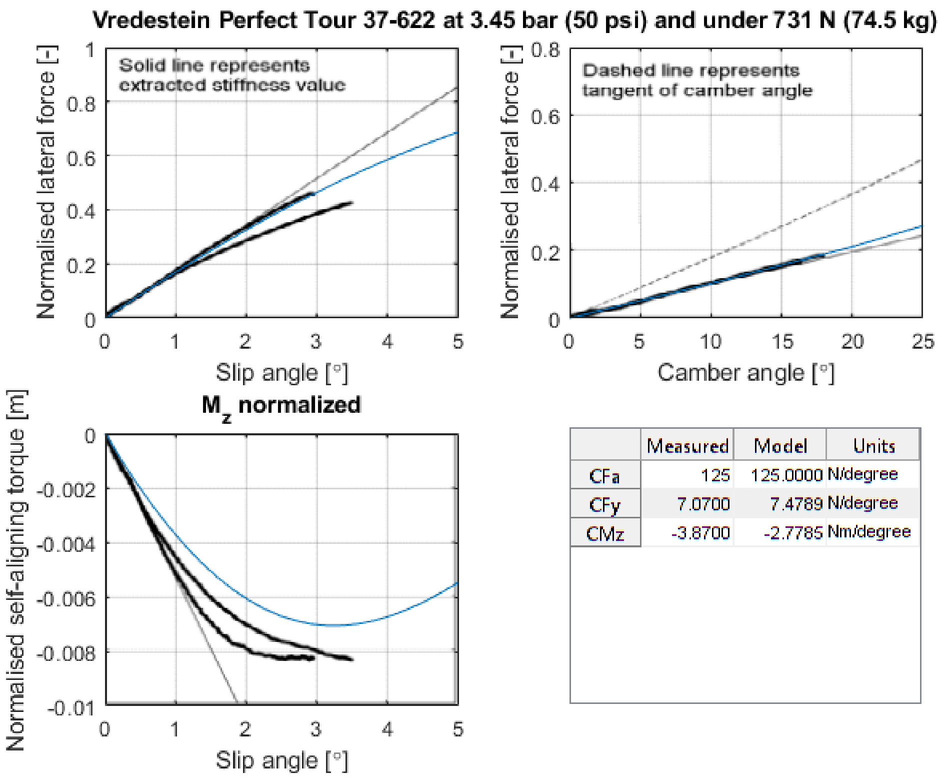
Vredestein Perfect Tour 37-622 at 3.45 bar (50 psi) and under 731 N (74.5 kg)

	Measured	Model	Units
CFa	125	125.0000	N/degree
CFy	7.0700	7.4789	N/degree
CMz	-3.8700	-2.7785	Nm/degree

Figure B.39

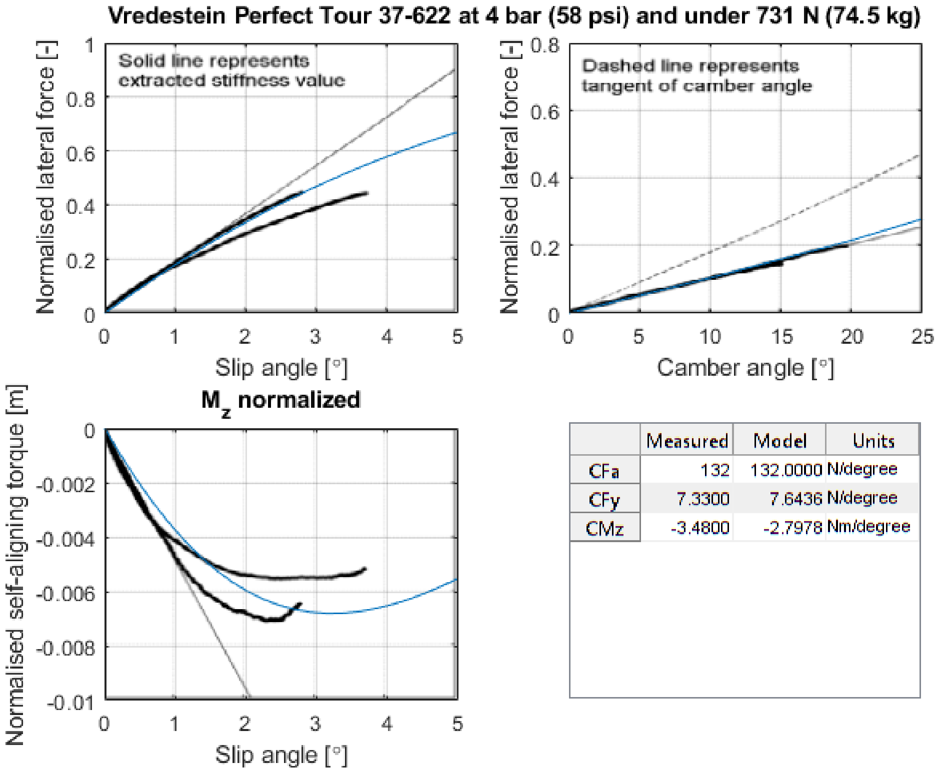

	Measured	Model	Units
CFa	132	132.0000	N/degree
CFy	7.3300	7.6436	N/degree
CMz	-3.4800	-2.7978	Nm/degree

Figure B.40

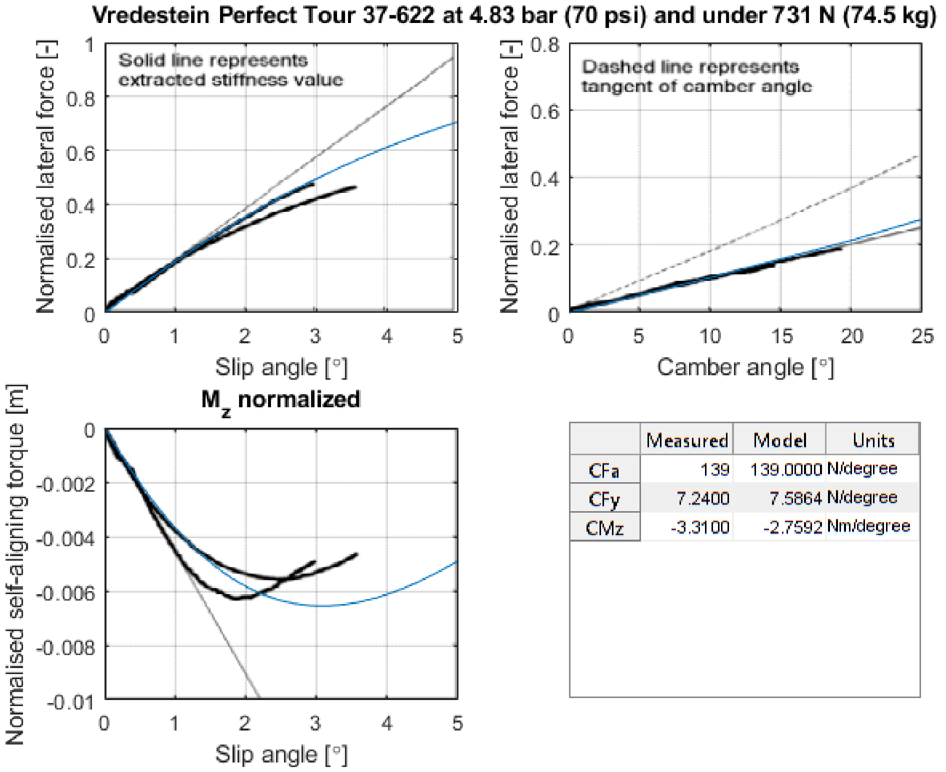

	Measured	Model	Units
CFa	139	139.0000	N/degree
CFy	7.2400	7.5864	N/degree
CMz	-3.3100	-2.7592	Nm/degree

Figure B.41

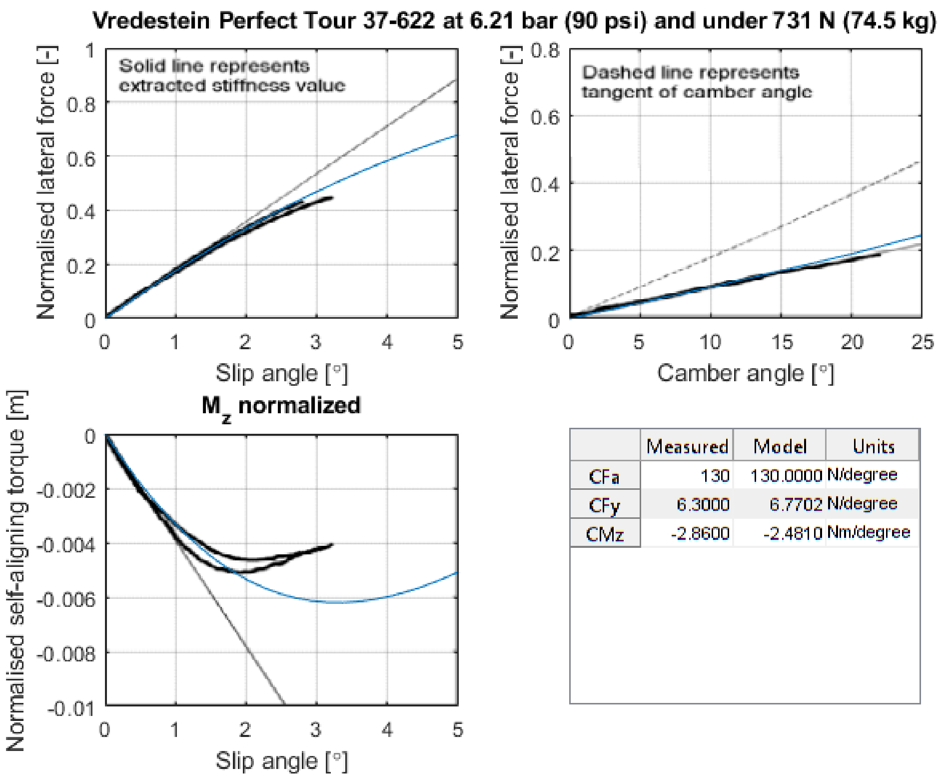

	Measured	Model	Units
CFa	130	130.0000	N/degree
CFy	6.3000	6.7702	N/degree
CMz	-2.8600	-2.4810	Nm/degree

Figure B.42

Bibliography

[1] H. B. Pacejka, *Tire and Vehicle Dynamics* (Elsevier Ltd., Oxford, United Kingdom, 2012).

[2] *Ftire,* (2018), https://www.cosin.eu/.

[3] J. Papadopoulos and A. E. Dressel, *Nonlinear brush formulation for a bicycle tire based on rotta model,* in *Bicycle and Motorcycle Dynamics* (2016).

[4] A. E. Dressel, *Measuring and modeling the mechanical properties of bicycle tires*, Ph.D. thesis, The University of Wisconsin-Milwaukee (2013).

[5] J. Knuit, F. de Kok, P. Raaphorst, and A. van der Spek, *Bicycle tire stiffness and damping,* (2014), bachelor Thesis.

[6] H. B. Pacejka, *Spin: camber and turning,* Vehicle System Dynamics **vol. 43**, pp. 3/17 (2005).

[7] J. Rotta, *Zur statik des luftreifens,* Ingenieur-Archiv **17**, pp. 129 (1949).

[8] J. Rotta, *On the statics of the pneumatic tire,* (1952), (Zur Statik des Luftreifens). Translated by R.E. Frank, Cornell Aeronautical Laboratory, Inc., February 1952.

[9] J. P. Meijaard and A. A. Popov, *Tyre modelling for motorcycle dynamics,* Vehicle System Dynamics **vol. 43**, pp. 187 (2005).

[10] S. Beregi and D. Takács, *Analysis of the tyre-road interaction with a non-smooth delayed contact model,* in *Rolling Contact Mechanics for Multibody System Dynamics* (2017).

[11] G. Rill, *Tmeasy - the handling tire model for all driving situations,* in *Proceeding of the XV International Symposium on Dynamic Problems of Mechanics* (2013).

[12] D. Takács, G. Orosz, and G. Stépán, *Delay effect in shimmy dynamics of wheels with streched string-like tyres,* European Journal of Mechanics A/Solids **28**, pp. 516 (2009).

[13] D. Takács and G. Stépán, *Contact patch memory of tyres leading to lateral vibrations of four-wheeled vehicles,* Philosophical Transactions of the Royal Society A: Mathematical Physical and Engineering Sciences **vol 371** (2013), https://doi.org/10.1098/rsta.2012.0427.

[14] P. Lugner, H. B. Pacejka, and M. Plöchl, *Recent advances in tyre models and testing procedures,* Vehicle System Dynamics **vol. 43**, pp. 413 (2005).

[15] D. Takács and G. Stépán, *Micro-shimmy of towed structures in experimentally uncharted unstable parameter domain,* Vehicle System Dynamics **vol. 50**, pp. 1613 (2012).

[16] A. Thaitirarot, R. Flicek, D. A. Hills, and J. R. Barber, *The use of static reduction in the solution of two-dimensional frictional contact problems,* Journal of Mechanical Engineering Science **vol. 228**, pp. 1474 (2014).

[17] P. W. A. Zegelaar, *The dynamic response of tyres to brake torque variations and road unevenesses*, Ph.D. thesis, Delft University of Technology (1998).

[18] V. Cossalter, *Motorcycle Dynamics* (Lulu.com, Morrisville, North Carolina, USA, 2006).

[19] R. T. Uil, *Non-lagging effect of motorcycle tyres: An experimental study with the Flat Plank Tyre Tester*, Tech. Rep. (Eindhoven University of Technology, 2006).

[20] G. A.N. and W. J.D., *The Pneumatic Tire* (NHTSA, Washington D.C., United States of America, 2006).

[21] J. C. Lagarias, J. A. Reeds, M. H. Wright, and P. E. Wright, *Convergence properties of the nelder-mead simplex method in low dimensions,* Society for Industrial and Applied Mathematics **vol. 9**, pp. 112 (1998).

[22] J. A. Nelder and R. Mead, *A simplex method for function minimization,* The Computer Journal **vol. 7**, pp. 308 (1965).

[23] C. G. Broyden, *The convergence of a class of double-rank minimization algorithms,* IMA Journal of Applied Mathematics **vol. 6**, pp. 76 (1970).

[24] R. H. Byrd, J. C. Gilbert, and J. Nocedal, *A trust region method based on interior point techniques for nonlinear programming,* Mathematical Programming **vol. 89**, pp. 149 (2000).